SPACE-BORNE RETRIEVAL OF SOLAR-INDUCED PLANT FLUORESCENCE AND ITS RELATIONSHIP TO PHOTOSYNTHETIC PARAMETERS

Narges Khosravi

Dissertation zur Erlangung des Grades *Doktor der Naturwissenschaften*

Institut für Umweltphysik
Fachbreich 1
Universität Bremen

May 2017

Contents

Abstract

Studies have shown that chlorophyll fluorescence is directly linked to the photosynthetic efficiency of plants. The excess absorbed energy by leaves which has not been used in photosynthesis is re-emitted to the environment, either as heat or fluorescence. Therefore, any potential stress in plants is technically visible through monitoring fluorescence and the Solar-Induced plant Fluorescence (SIF) can thus be monitored as an indicator for vegetation growth and health status. SIF is a broad band spectral feature exhibiting two maxima at about 680 and 740 nm respectively, also known as red and far-red SIF. In the recent decades, there have been several studies addressing SIF, its importance and approaches to measure its value over vegetated regions.

Among several measurement approaches, satellite-based *remote sensing* of SIF is particularly valuable, since the covered (spatial) area can be explicitly larger than is the case with in-situ measurements. With current space-borne instruments, even a full global coverage is attainable within a few days. In the framework of this thesis, two novel methods have been developed, tested and utilized to retrieve SIF from hyper-spectral satellite measurements.

In particular, the first developed method, makes use of the Fraunhofer absorption lines in the far-red spectral region (748.5 - 753 nm), to retrieve SIF via its in-filling effect on these absorption lines. However, the satellite-based remote sensing spectrometers, used in this work, typically exhibit an additive spectral feature, which is not fluorescence. This is often accompanying the actual SIF retrieval and can significantly deteriorate the results. To account for this effect, a correction method has been developed and is combined with the retrieval algorithm. The model-based sensitivity

studies confirmed the feasibility of the method to disentangle SIF from this additive feature. Additionally, the potential influences of the atmospheric and measurement conditions on the retrieval results have been assessed. Finally, the method has been applied to ten years of SCIAMACHY data and the retrieved results have been mapped on seasonal base. On a global scale, the obtained values are between 0 to 4 mW m^{-2} sr^{-1} nm^{-1}.

In absence of large area ground based validation data, final judgment of the results obtained in the framework of this study, is not possible. Alternatively, comparison of the achieved results with those published by the US National Aeronautics and Space Administration (NASA) Goddard Space Flight Center (GSFC) has been performed. Despite some differences, the comparison also exhibited close results, both qualitatively and quantitatively. It should be noted that comparisons among the retrievals provided by other research groups (not only GSFC) over the same spatial region is also variable depending on the instruments and methods utilized (ranging on average from a few tenths to more than 4 mW m^{-2} sr^{-1} nm^{-1}).

To further assess the reliability of retrieved SIF, monthly average values have been compared to ground-based flux-tower measurements of Absorbed Photosynthetically Active Radiation by plants (APAR) and Gross Primary Production (GPP), for a time span of several years. The agreement between the seasonal trends of SIF and these parameters was significant.

Although the main focus of this PhD work was on retrieving SIF in the far-red wavelength region using a spectral micro-window, there are clear scientific benefits in having an estimation over the full spectral emission range of SIF. Therefore, the second retrieval method, developed in the framework of this work, was to obtain the full spectrum of the emitted SIF by retrieving the leaf and canopy parameters, utilizing a combination of two radiative transfer models. The model-based studies showed the feasibility of the method to retrieve SIF with high accuracy. Moreover, the first results of applying this approach on GOME-2 measurements demonstrated promising outcomes. Examples of the fit quality and retrieved SIF over two different vegetation coverage types have been presented in this thesis, showing clear applicablity of the method to retrieve SIF over its full spectral emission range and the potential to derive other vegetation parameters (e.g. Chlorophyll content of the leaves and the so-called leaf area index).

The method and results presented in this thesis are partially already published as Khosravi et al. [2015].

The content of this thesis has also been presented in the following conferences:

- Poster presentation at Global Vegetation Monitoring and Modeling (GV2M). conference, Avignon, France, February 2014.
- Poster presentation at Nationales Forum für Fernerkundung und Copernicus, April 2014.
- Oral presentation at “Earth Observation for Ocean-Atmosphere Interaction” conference, ESA Earth observation center, Frascati, Italy, October 2014.
- Poster presentation at American Geophysical Union (AGU) fall meeting, San Francisco, US, December 2014.
- Oral presentation at Workshop "Nutzung der Sentinels und nationalen Erdbeobachtungs-Missionen" in DLR meeting, Bonn, Germany, January 2015.
- Poster presentation at European Geophysical Union (EGU), Vienna, Austria, April 2015.
- Poster presentation at the International Union of Geodesy and Geophysics (IUGG), Prague, Czech republic, June 2015.
- Poster presentation at American Geophysical Union (AGU), San Francisco, USA, December, 2015.

Acknowledgement

My highest gratitude goes to my supervisor and advisor, *Dr. Marco Vountas*, whose trust, encouragement, exemplary patience and good-natured disposition kept me going whenever I got stuck. His enthusiasm, friendship and heuristic advices throughout my master's and doctoral programmes have made me a better student, researcher, programmer and a better person. It has been a great privilege to work alongside him and other members of the "Aerosol, Cloud and Surface Parameterization" research group (CASPAR). Mere thanks do not suffice.

I would like to thank *Prof. John P. Burrows*, who generously shared with me his illuminative comments at key moments in my work while also allowing me to work independently the majority of time. Being able to attend his lectures and seminars has been one of the highlights of my studies in Bremen. I could always count on him for inspiration and guidance and I was never disappointed.

I very much owe this thesis to *Dr. Vladimir Rozanov*, who painstakingly developed the comprehensive radiative transfer model SCIATRAN, vital to this project. I am very thankful for his unrestricted support in developing methods and for sharing his exceptional expertise with me.

I wish to thank all the professors, fellow doctoral students, Postdoctoral researchers, members of staff and friends at the Institute of Environmental Physics and the University of Bremen in general, who supported me throughout these years and went out of their way to ensure that both my academic experience and my life in Germany would be as productive and enjoyable as it could be. Particular mention, in random order, should be given to *Prof. Dr. Reiner Schlitzer* and *Prof. Dr. Emily King* for everything they have taught me; *P.D. Dr. Annette Ladstätter-Weißenmayer* for her never-ending encouragement, wise counsel and empowering support; *Dr. Andreas Hilboll* for his friendship, practical suggestions and helping me through the darkest of days; *Dr. Luca Lelli* for helping me when I most needed and for tolerating me in the same

office room. I have enjoyed his light-hearted jokes and my heated and wide ranging arguments with him. I should also thank *Conor Gouch Murray* who proofread my thesis, computer experts *Heiko Schellhorn* and *Heiko Schröter* who never hesitated to share their knowledge with me; friends in administration, *Stephanie Drath, Geraldine Schmiechen, Anke Werner, Lars Jeschke* and *Anja Gatzka* who helped me in every way they possibly could; *Günther Lehnert* and other members of our coffee-break circle who patiently explained the subtleties of the German language and culture and made me feel more at home in Bremen.

I am forever indebted to my parents, *Shayesteh Sepehr* and *Mohammad Khosravi* for their unlimited and unconditional support, love and encouragement. They were my aspiring role models and they prioritized my education above all. I am also beholden to the heart-warming presence of my dear sister *Sara Khosravi*, here at the University of Bremen for two of my years here.

Because this may be my only opportunity to thank these individuals in writing, I must thank my late uncle *Mohammad Sepehr* for instating in me a fascination with natural sciences; *Achmed Suhrke* for his altruistic and boundless support from my first day in Germany and for always being there for me in the past six years, *Prof. Dr. Morteza Shahbazi* who kept me interested in Physics and saw the potential that I could not see in myself; *Saeid Bagheri* for supplying me with the world's best fettuccine alfredo and *Hanna Rademaker* for remaining my best friend and my loyal partner in crime. Special thanks to *Dr. Sharareh Tavaddod* for her wise tips and her warm hospitality when I was attending a course in the town she then resided; *Maryam Sharifi*, *Samar Hosseini* and *Omid Kia* for their genuine friendship.

Part I

Introduction and Theory

Chapter 1

Introduction

1.1 Motivation

Terrestrial life-forms can be affected by variations in temperature, humidity, precipitation, wind and other meteorological patterns and atmospheric conditions. Since most species favor specific settings, relatively rapid changes in the climate may alter their population dynamics and surpass their ability to adapt. In fact, climate change is contributing to the loss of biodiversity on a global scale and life on Earth is extremely vulnerable today [Midgley et al., 2002]. As far as our knowledge extends, the current rate of climate change is unparalleled in the history of the planet and there is a clear scientific consensus on the role of human activities in climate modification [Oreskes, 2004].

The Earth's climate is regulated in part by the composition of the atmosphere and the warming effect of the so-called greenhouse gases. Although water vapor and clouds play a significant role in Earth's greenhouse effect, the atmospheric concentrations of carbon dioxide (CO_2) is the most important modifier of the planet's temperature variation [Lacis et al., 2010] implying that abnormally high levels of this gas may contribute to higher temperatures. The CO_2 levels before the industrial age have varied between an estimated low of approximately 180 parts per million (ppm) during the ice ages, to a high of approx. 280 ppm during warmer periods. Accordingly, it has been suggested that the global mean temperature difference between the interglacial periods and ice ages has only been about 5 degrees Celsius [Lacis et al., 2010]. However, on May 2013 the US National Aeronautics and Space Administration (NASA) announced the average global CO_2 concentration had reached 400 ppm for the first time in recorded

history[1]. Yet again, September 2016 was declared the warmest September globally over 136 years of modern record-keeping, according to NASA's Goddard Institute for Space Studies (GISS). The Arctic ice cap has also reached its lowest extent on record at the same time[2].

The fifth report of the Intergovernmental Panel on Climate Change (IPCC) states unequivocally that Earth's climate is being affected by human activities: "Human activities ... are modifying the concentration of atmospheric constituents... that absorb or scatter radiant energy. ... most of the observed warming over the last 50 years is likely to have been due to the increase in greenhouse gas concentrations" [Bernstein et al., 2008]. According to the IPCC reports, land use and land-use change have a direct influence on the exchange of greenhouse gases between terrestrial ecosystems and the atmosphere. Deforestation is associated with land-cover change and reduction in the global carbon uptake. According to the United Nations Food and Agricultural Organization (FAO), $\sim$ 129 million hectares of forest have been cleared since 1990 and converted into industrial, agricultural and residential areas [Singh, 2013], suggesting land-use management has a significant effect on sources and sinks of CO_2, CH_4, and N_2O[3].

On the other hand, the growth of the human population necessitates a proportional growth in food resources and according to the World Bank, 50-100% more food than is being produced today will be required to support the human population of 2050 [Godfray et al., 2010]. Therefore, preserving the remaining forests has become ever more challenging and fastidious land-use management should be concerned.

It is well-known that there is a delicate balance between carbon emission and uptake between the Earth's atmosphere and biosphere with photosynthesis being the first key process eliminating CO_2 from the atmosphere. Approximately 120 [Gt] of carbon is absorbed annually by terrestrial vegetation which is significantly higher than the amount of carbon released through human activity, e.g. fossil-fuel combustion (Fig. 1.1).

The regulatory effect of vegetation goes beyond carbon absorption. In general, Forests affect surface reflectance patterns, humidity, aerosols and cloud-forming processes which in turn influence from regional-to-continental to global scales. Accordingly, the photosynthetic behavior of plants not only affects the climatological characteristics of their immediate surroundings but it also exerts significant influence on the Earth's interrelated cycles and spheres. As demonstrated by Fig. 1.2, , terrestrial plants are a major factor affecting the global energy cycle and temperature balance. All

[1] https://climate.nasa.gov/news/2503/september-was-warmest-on-record-by-narrow-margin/

[2] http://climate.nasa.gov/news/2496/arctic-sea-ice-annual-minimum-ties-second-lowest-on-record/

[3] major greenhouse gases, which impact the global temperatures

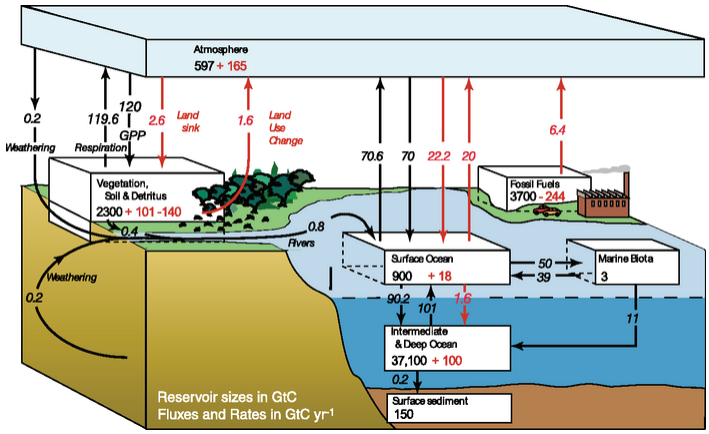

Figure 1.1: The global carbon cycle for 1990s according to the report of the Intergovernmental Panel on Climate Change (IPCC) [Bernstein et al., 2008] [GtC yr^{-1}]. Natural carbon fluxes are illustrated in black and anthropogenic fluxes in red.

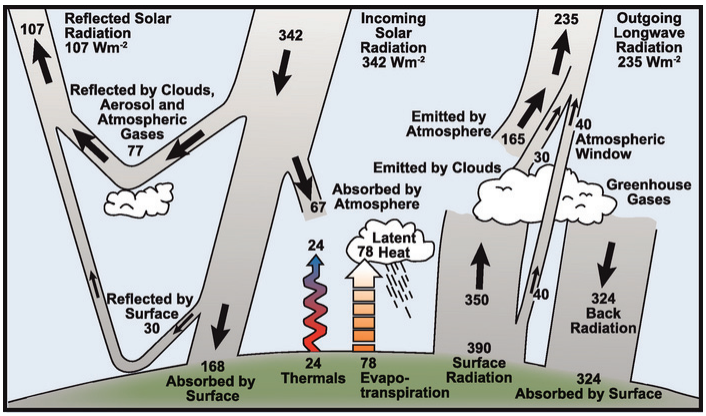

Figure 1.2: Estimate of the Earth's annual and global mean energy balance [Kiehl and Trenberth, 1997].

together, any effort towards sustainable development has to address global vegetation.

Certainly, none of the challenges involved can be addressed as stand-alone issues and holistic approaches must be sought. In order to devise effective strategies, it is imperative that we have access to wide-ranging monitoring systems and reliable data collection techniques. One of the relatively recent developments in the field of terrestrial vegetation monitoring is the innovative use of Sun-Induced plant Fluorescence (SIF).

Introduced less than twenty years ago, measuring SIF has been put forward as a promising method to not only detect a vegetated area, but also monitor the health and stress status of the plants and examine the extent of their contribution to the global

carbon uptake. Since fluorescence as a by-product of photosynthesis is a fraction of surplus absorbed energy which is re-emitted to the environment, SIF is an indicator of the overall photosynthetic efficiency and may be of interest to various research purposes and environmental applications. Lately, SIF is finding its place in the space-borne land and vegetation monitoring technology and SIF measurements are being incorporated into Earth observation missions which provide insights into the relationship between climate studies and environmental, agricultural, silvicultural and land-use planning. However, measuring SIF is challenging and requires rather complex retrieval methods particularly in large spatial scales.

1.2 Outline

This dissertation summarizes a (more than) three year process of method development as well as the assessment of the potentials and limitations of the methods. It is structured into three main parts focusing on (I) "introduction and theory" providing introductory information on the topic, (II) "Model and data" that focuses on the method development, models and instruments used, leading to (III) the results of the work.

Chapter 1 is divided into two parts, the general motivation and the outline of the study. Chapter 2 provides necessary scientific information on fluorescence and how it is related to photosynthesis. The fluorescence yield and its relationship with CO_2 absorption is answering the question why retrieving fluorescence from the atmosphere is instructive. Understanding radiative transfer through the atmosphere is essential to remote sensing of any signal from a space-borne instrument. Building on that, a brief summary of radiative transfer through the atmosphere is given in section 2.2. This is followed by discussing different approaches to measure fluorescence and the reasons based on which, the first approach has been selected. Before discussing this developed retrieval method, the most important published research papers on solar-induced vegetation fluorescence are summarized at the end of this chapter. These studies have been either conducted before the starting point of this study or during the progress of this work. Chapter 2 ends with section 2.5, pointing out the objectives of this study in detail.

Building on the introductory part, the first developed retrieval method is discussed in chapter 3. The radiative transfer model which is used in the development as well as the retrieval processes is also introduced in this chapter followed by an introduction on the space-borne instruments chosen for the retrieval.

Prior to the global retrieval of SIF, a thorough analysis on the feasibility and limitations of the developed approach is required. Therefore, a detailed sensitivity

analysis of the retrieval method is provided in chapter 4. The possible sources of systematic and random errors are assessed and possible ways to reduce their effects have been discussed. Additionally, the effects of several measurement characteristics on the retrieved quantity are modeled and the sensitivity of the SIF signal on the spectral wavelength window is tested.

Based on the outcome from chapters 3 and 4, fluorescence has been successfully retrieved from satellite-based measurements which are presented in chapter 5. The obtained values are compared to the findings of other research groups. After gaining confidence of the retrieval quality looking at ten years of data, the relationship between vegetation fluorescence and photo-biochemistry of vegetation is discussed on different scales in the next sections of this chapter. Firstly, the relationship between the retrieved SIF and the seasonal variation of the vegetation coverage on global scale is investigated. Secondly, the photobiochemical behavior (e.g. light absorption) of the canopy is compared to the retrieved SIF on local scale in order to assess correlations between these quantities. These photobiochemical variables are connected to some specific characteristics of the canopy and leaves in plants. Such canopy/leaf properties define photosynthetic efficiency, the optical characteristics of the canopy and fluorescence emission.

Accordingly, chapter 6 is dedicated to a relatively independent study of the relationship between the most important canopy/leaf parameters and canopy reflectance. This model-based study has aimed to retrieve and characterize SIF from its full emission spectrum. The sophisticated approach taken for this is unique, using a combined radiative transfer and leaf/canopy model.

The final chapter of this dissertation (chapter 7) discusses the obtained results as well as suggestions for further investigations.

Chapter 2

Scientific Background

In the present chapter photosynthesis will be discussed as the process in which fluorescence is generated. In the following, the main techniques established to measure the emitted fluorescence will be discussed focusing on the space-borne spectral retrieval used in this study. Consequently, the radiative transfer equation solved in the retrieval process will be introduced.

2.1 Plant photosynthesis and its relation to fluorescence

Photosynthesis has a rather complex relationship with fluorescence emission and can be discussed from different points of view. From the ecosystem perspective, photosynthesis is responsible for terrestrial carbon uptake from the environment and the subsequent release of oxygen back into the environment. However, the biophysics and chemistry of photosynthesis have to be understood in order to investigate the microscopic process in which fluorescence is emitted from plant cells.

2.1.1 Photosynthesis as a mechanism of energy transformation

Originating from Greek language, *photosynthesis* can be translated as *construction with light*. Photosynthesis in many photosynthetic organisms[1], including plants, can be defined as the process of making use of light (as an energy source), water and CO_2 to produce high energy organic molecules known as sugars. Such an organism is called an *autotroph*. Autotrophs are defined as organisms which are able to form organic substances from inorganic substances such as carbon dioxide. Autotrophs are also referred to as primary producers of the ecosystem, capable of storing solar

[1] an individual form of life which is able to function independently

energy by building organic matter. The produced organic matter is converted to energy again by the primary producer itself (also known as autotrophic respiration[2]; R_a) or by the primary consumers e.g. animals (heterotrophic respiration[3]; R_h). Unlike photosynthesis, respiration is not light dependent and remains relatively constant during the time [Chapin III et al., 2011].

Photosynthesis in plants occurs sequentially from utilizing light to produce energy molecules known as ATP[4] and NADPH[5] (in a process known as the *light reactions*) followed by making use of the energy molecules for carbon fixation which do not directly require light (also known as *dark reactions*).

Based on their environmental conditions, plants have developed three photosynthetic pathways, known as C3, C4 and CAM[6] which determine their growth and distribution patterns. The C4 and CAM photosynthetic pathways, are observed in plants mainly found in the sub-tropics and arid regions. These photosynthetic pathways are more water efficient than C3, the photosynthetic pathway by which the majority of plants reduce CO_2 to sugar. The main difference between photosynthetic pathways is the ability of plants to extract carbon dioxide more efficiently for photosynthesis, while preventing water evaporation from the surface in warm environments. C4 and CAM photosynthesis have been observed in less than 10% of land vegetation [Sage, 2004, Keeley and Rundel, 2003]. For the sake of simplicity only C3 photosynthesis is explained here (further information on photosynthetic pathways is available in e.g. Chapin III et al. [2011] p.98-105).

A scheme of simple C3 photosynthetic process is shown in Fig. 2.1. The leaf cells responsible for photosynthesis in C3 (and CAM) plants are mesophyll cells, literally translated as the *central leaf*, referring to the position of the mesophyll cells in plant leaves. Mesophyll cells are the sites of light reactions for plants with all photosynthetic pathways. Mesophyll cells are located below the upper leaf epidermis[7] and contain the chloroplast organelles[8] in which photosynthesis occurs. Each chloroplast contains a fluid called stroma, which surrounds sacks of thylakoids. Thylakoid sub-organelles are membrane-bound compartments carrying the photosynthetic pigments such as chlorophyll molecules. The latter is the most important molecule absorbing light energy

[2] the metabolism of organic matter by plants

[3] the metabolism of organic matter by the non-primary producers e.g. bacteria, fungi, and animals

[4] Adenosine TriPhosphate

[5] Nicotinamide Adenine Di-nucleotide PHosphate

[6] Crassulacean Acid Metabolism

[7] In botany, the outermost layer of cells covering the stem, root, leaf, flower, fruit, and seed parts of a plant

[8] any of the in-cell structures, which is specialized to perform a specific function

during the light reactions.

The light reactions are the processes by which the absorbed light energy is converted into chemical energy, utilizable for chemical work in autotrophs. In plants, a complex of photosynthetic pigments bound by proteins form a *reaction center*, where the absorbed light energy is converted to chemical energy in the forms of ATP and NADPH molecules. To maximize the light absorption, plants have evolved to develop light-harvesting complexes (*antennae*) to capture the light energy and transfer it to the reaction centers (see 2.1.3).
A combination of both antenna and reaction center in the thylakoid's membrane is defined as a PhotoSystem (PS). Some plants have developed two types of PSs known as Photosystem I (PSI) and Photosystem II (PSII) having spectral absorption peaks at 700 and 680 nm respectively. The generated ATP and NADPH molecules by PSs are transported from the thylakoid's membrane to the stroma in which they are utilized for the dark reactions to fix CO_2 and produce sugar.
The main focus of this work is on light reactions in which fluorescence is a byproduct. However, a brief description of the dark reactions is given in the following paragraphs. For further details on dark reactions refer to Chapin III et al. [2011].

The dark reactions (also known as carbon fixation or the Calvin cycle) occurs in the stroma and converts CO_2 to the final product of photosynthesis; $C_6H_{12}O_6$ (glucose) as shown in equation 2.2. Although, details of this process are not used in the framework of this thesis, it is mentioned here briefly for the sake of comprehensiveness. In C3 plants, the Calvin cycle starts with a CO_2 molecule being incorporated into a 5-carbon compound (RuBP)[9] and forming two 3-carbon compounds (3-PGA)[10]. This process is known as carboxylation [11] and is catalyzed by a RuBisCO[12] enzyme. An ATP molecule produced in light reactions is used for converting a 3-PGA into an intermediate product (1,3BPGA)[13] and finally, the 1,3BPGA is reduced to a molecule known as G3P[14] by NADPH. Two G3Ps can form a sugar molecule.

The Calvin cycle has slight variations among different photosynthetic paths but detailed chemistry is not the subject of this work. However, the Calvin cycle's contribution to the CO_2 uptake by terrestrial photosynthesis is relevant to the objectives of this

[9] Ribulose-1,5-bisphosphate
[10] 3-Phosphoglyceric acid
[11] introducing a carboxyl acid (COOH) group to a substrate
[12] Ribulose-1,5-bisphosphate carboxylase/oxygenase
[13] 1,3-Bisphosphoglyceric acid
[14] Glyceraldehyde 3-phosphate

thesis and is discussed in the following.

2.1.2 Photosynthesis and the global carbon cycle

Photosynthetic organisms (e.g. plants) use CO_2 as a source of carbon for their food synthesis, which gives them a key role in the global carbon cycle. On an ecosystem scale, photosynthesis is described by the Gross Primary Productivity (GPP). This is the rate at which vegetation removes carbon from the environment (e.g. Gitelson et al. [2012]) or the total amount of carbon ($gCm^{-2}yr^{-1}$) absorbed in the process of photosynthesis by photosynthesizing organisms. However, some of the absorbed CO_2 is released to the atmosphere during the respiration process. Respiration is not part of photosynthesis but is part of the process through which the CO_2 accumulation and dissipation forms the global carbon cycle. While investigating the contribution of land vegetation in the global carbon cycle, the role of respiration has to be taken into account. The Net Primary Production (NPP) is accordingly the net production of organic matter in excess of autotrophic respiration (R_a):

$$\text{NPP} = \text{GPP} - R_a.$$

Likewise, the Net Ecosystem Production (NEP) is defined as the net accumulation of carbon by an ecosystem, which is the difference between the net production rate of the organic matter (NPP) and the heterotrophic respiration (R_h):

$$\text{NEP} = \text{NPP} - R_h.$$

The net carbon flux between land surface and the atmosphere, known as Net Ecosystem Exchange (NEE) is the same quantity as NEP (with negative sign), which is the CO_2 flux exchange between the canopy[15] and the atmosphere due to photosynthesis/respiration processes and is measured in-situ, based on tower-based eddy-covariance methods [Jung et al., 2011]. The Eddy covariance technique is a non-invasive way to measure the flow of carbon, water and energy to and from an ecosystem. At regional scales, the eddy covariance technique provides a direct measurement of these fluxes between the canopy and the atmosphere [Baldocchi et al., 2001]. These fluxes are seen as indicators for photosynthetic efficiency and therefore, are closely connected to chlorophyll fluorescence (as will be explained in section 2.1.4).

Only a specific range of the the solar spectrum can be utilized for photosynthesis (see section 2.1.3) which is known as the Photosynthetically Active Radiation (PAR).

[15] uppermost layer of foliage (banches of the trees, crops, etc.)

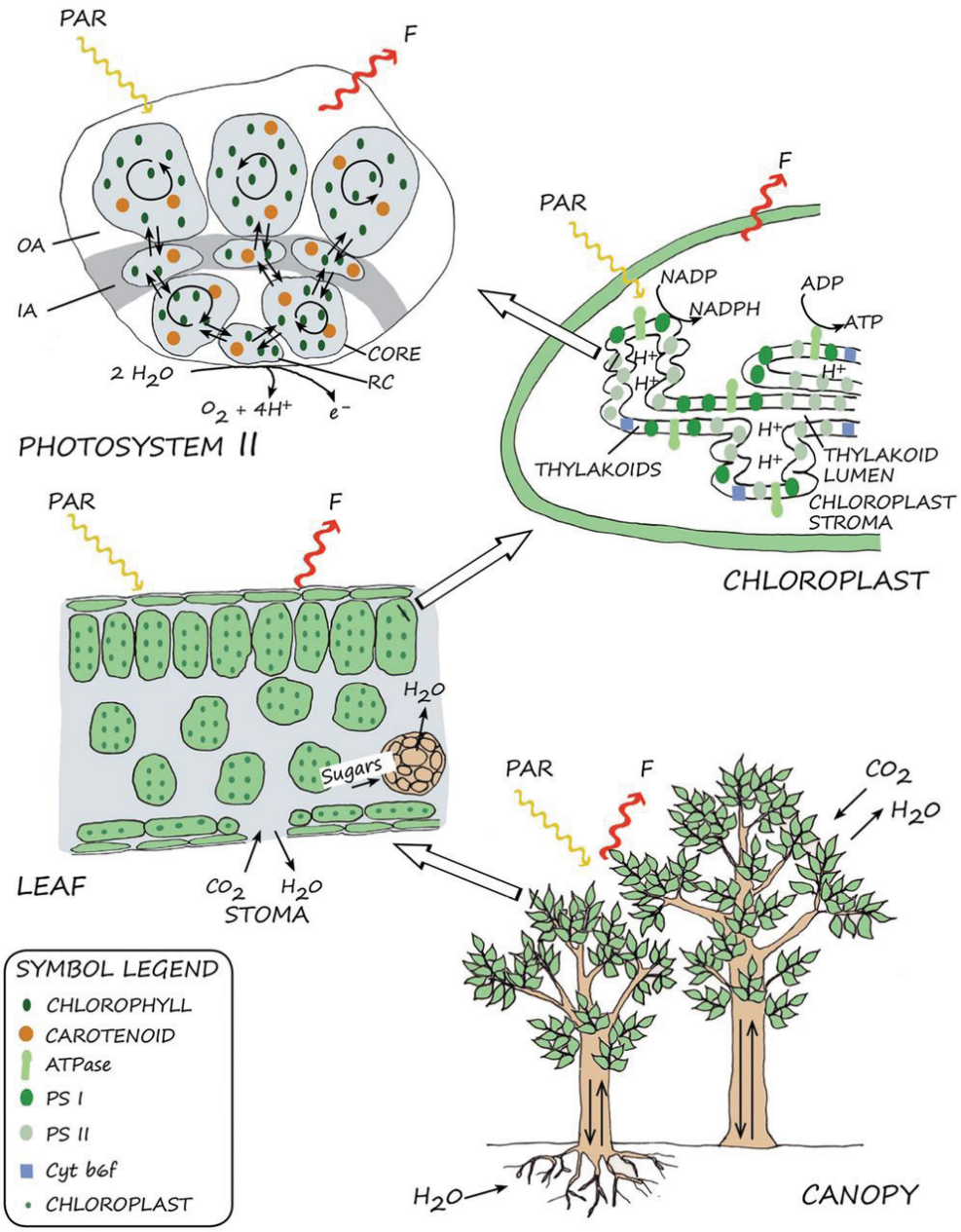

Figure 2.1: A sketch of photosynthesis on different levels: On the ***bottom-right****, the plants can be seen absorbing CO_2 and H_2O as well as light (PAR) necessary for photosynthesis from their environment and emitting O_2 (not shown) and fluorescence back to the environment. A closer look to the leaf (****bottom-left****) shows the sacks of chloroplast containing chlorophyll pigments. A sketch of a chloroplast can be seen on the* ***top-right*** *containing thylakoids floating in the chloroplast stroma. Inside the internal membrane of a chloroplast is filled with so-called stroma fluid. The thylakoids are organized into stacks, known as grana (single: granum) surrounded by stroma. All the chlorophyll in the chloroplast is located in the membranes of the thylakoid vesicles. The PhotoSystems (PSs) within the thylakoid membranes shown in different colors, are responsible for creating NADPH from NADP and ATP from ADP as energy "currencies" [Porcar-Castell et al., 2014] for carbon-fixation. Details on the light reactions can be followed on the* ***top-left****, presenting inside of the thylakoid membrane. [Porcar-Castell et al., 2014]*

The fraction of the Absorbed PAR (APAR) by the canopy in order to be utilized for photosynthesis is abbreviated as fAPAR.

In essence, GPP can be described as:

$$\text{GPP} = \text{PAR} \times f\text{APAR} \times \text{LUE}_p = \text{APAR} \times \text{LUE}_p \,, \tag{2.1}$$

in which LUE_p is the Light Use Efficiency by which PAR is consumed for photosynthesis. As shown in equation 2.1, GPP is directly dependent on the light absorption. The relationship between light absorption and fluorescence emission by plants is the key point connecting GPP to fluorescence emission. Therefore, the physico-chemical aspect of photosynthesis leading to fluorescence emission has to be discussed as a prerequisite.

2.1.3 The physics and chemistry behind photosynthesis

Despite its complexity, photosynthesis can be described as a straightforward non-spontaneous chemical reaction. The overall photosynthetic reaction of the green plants can be written as:

$$6\text{CO}_2 + 6\text{H}_2\text{O} \xrightarrow[Chlorophyll]{light} \text{C}_6\text{H}_{12}\text{O}_6 + 6\text{O}_2 \,, \tag{2.2}$$

in which $\text{C}_6\text{H}_{12}\text{O}_6$ is a carbohydrate molecule (simple sugar).

Photosynthetic activity is not limited to plants. Some bacterial species e.g. Cyanobacteria are also capable of photosynthesis although no oxygen is produced in these sorts of photosynthesis. A general reaction describing different forms of photosynthesis is:

$$\text{CO}_2 + 2\text{H}_2\text{A} \xrightarrow[bacteriochlorophyll]{light} (\text{CH}_2\text{O}) + \text{H}_2\text{O} + 2\text{A} \,, \tag{2.3}$$

in which H_2A is a reducing component, being oxidized to A (a reducing component). Consequently, CO_2 is the oxidizing substance, being reduced to (CH_2O) as one-sixth of a sugar molecule. In bacterial photosynthesis, H_2A can be a variety of molecules [Clayton, 1980]. C. B. van Niel was studying bacterial photosynthesis in the 1920s when he noticed that many bacterial photosynthetic paths share some similarities with the plant photosynthesis. Rewriting the reaction 2.2 as

$$\text{CO}_2 + 2\text{H}_2\text{O} \xrightarrow[Chlorophyll]{light} (\text{CH}_2\text{O}) + \text{H}_2\text{O} + \text{O}_2 \,,$$

he realized that plant photosynthesis can be considered to follow a specific form of reaction 2.3 having water as the reducing component and producing O_2 as the oxidized substance. Consequently, van Niel described plant photosynthesis to be a pair of redox

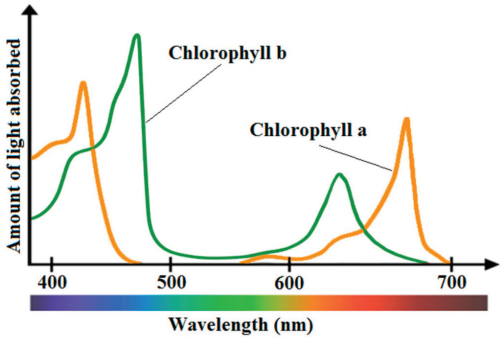

Figure 2.2: Absorption spectral features of chlorophyll-a and chlorophyll-b [Gholizadeh et al., 2016]

[16] reactions, benefiting from having water as the reducing compound which is abundant on Earth.

Light and its key role in photosynthesis

The Sun is the energy source required for plant photosynthesis as can be seen from reaction 2.2 and Eq. 2.1. The spectral range of PAR is $\sim$ 400 to 700 nm. However, as illustrated in Fig. 2.2 most of the photons that have a spectral wavelength between 480 nm and 550 nm are not being absorbed by the photon-collector pigments of the plant cells known as Chlorophyll molecules (Chl) within PSI and PSII [Taiz and Zeiger, 1998]. Outside of the PAR spectral region, plants have a sharp increase in their reflectance between $\sim$ 700 and 750 nm wavelengths. This rapid change in the absorption signature of plants in the far-red Near InfraRed (NIR) spectral region is referred to as the *red-edge*. As a result, plants have a relatively large reflectance in the far-red and NIR spectral range. Fig. 2.4a illustrates the dependence of the red-edge steepness simulated (using PROSAIL leaf-canopy model [Jacquemoud et al., 2009]) with respect to different vegetation concentrations defined by the total area of vegetation leaf per area; the so-called Leaf Area Index (LAI) [m^2/m^2].
There are two types of Chl molecules (**-a** and **-b**), each playing slightly different roles in photosynthesis. Chl-a is the primary and Chl-b is the accessory photosynthetic pigment. PSI usually consists mainly of Chl-a and is able to function independently of PSII. However, PSII is dependent on PSI and can contain Chl-b in its antenna [Heldt, 2005].

Describing light absorption by Chl molecules requires an introduction on photon

[16] an oxidation-reduction reaction which requires electron transfer between the species

absorption from the quantum mechanics perspective. An electromagnetic wave would only exchange energy with matter in integer number of energy quanta. It is also well-known that an atom could only exist in a distinctive set of energy states by gaining or loosing quantized energy equal to the difference between any pair of its energy states. Chl pigments are complex sets of molecules which provide a variety of energy transition possibilities. Therefore, the frequency of the absorbed light is not limited to a single value but covers a range of possible frequencies, forming broadband absorption signatures (referred to as *absorption bands*) for photosynthetic pigments (Fig. 2.2).

Singlet and triplet excited states for a photosynthetic pigment absorbing photons within the PAR spectral range (e.g. Chl molecule) are reached by an increase in the intrinsic angular momentum (spin) of the electrons shared between the atoms within the molecule. Absorption of an energy quantum by a Chl molecule can be translated to a transition of its electrons to higher energy levels. This transition can be caused by the excited electron having a spin in either the same or opposite orientation as it was in its ground state. These are known as the triplet and singlet states respectively.

The energy levels of a Chl molecule are shown schematically in Fig. 2.3. Assuming the molecule is in its ground state, its energy level increases to an excited state depending on the absorbed photon's energy. Red and blue light lead to a rise into the first singlet and higher energy states (e.g. second singlet) respectively. The energy level of an electron in second and higher energy states is too unstable and will immediately dissipate converting to internal (thermal) energy. The first singlet state is ~ 200 times more stable [Clayton, 1980] and an electron being in this energy level can reach the ground state via several pathways (as shown in Fig. 2.3). Each are defined by their first order rate constants expressed in physical units [s^{-1}] [Porcar-Castell et al., 2014]. These pathways include the following:

1. Transferring the energy to another molecule or to the reaction center, using it to drive photochemistry is represented by the rate constant of k_T.

2. Radiating a photon back to the environment is referred to as chlorophyll fluorescence (k_F).

3. Non-radiative dissipation mechanisms, which is either through thermal conversion or an internal mechanism known as the Non-Photochemical Quenching (NPQ). They are represented by the rate constants of k_D and k_{NPQ} respectively.

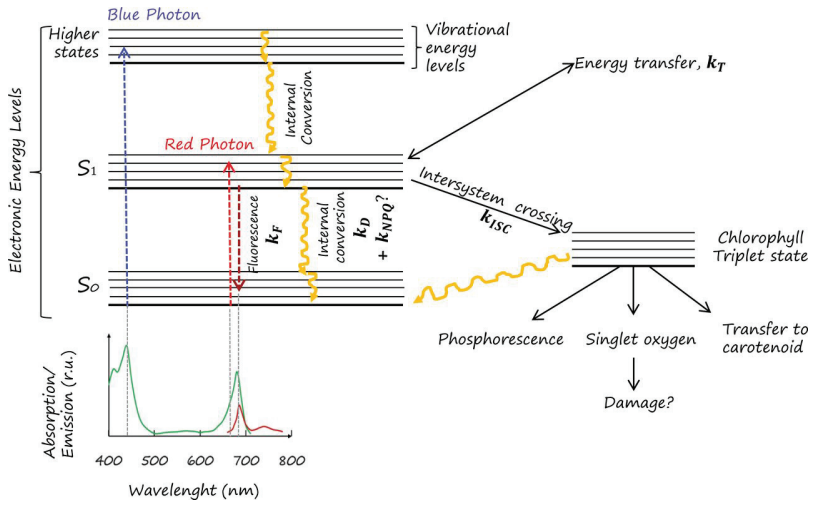

Figure 2.3: The energy states of a chlorophyll molecule.[Porcar-Castell et al., 2014]

4. Inter-system crossing[17] leads to formation of a triplet state (k_{ISC}). The transition from the triplet state to the ground state can occur by formation of reactive oxygen radicals, which can damage the Chl molecule. The triplet state energy can also be dissipated via phosphorescence.

The Chl-a pigment in the PSII reaction center has an absorption maximum at 680 nm. Likewise, the absorption peak of PSI has a maximum at longer wavelength of 700 nm. Therefore, PSI is able to accept energy in the form of electrons from PSII as well as to absorb light independently.

In a PSII within a plant cell, Chl molecules can release their excitation energy by transferring it to the reaction center leading to an unstable excited energy state. The conversion of the absorbed electromagnetic energy to a chemical energy form starts with the release of an electron from the excited reaction center. The electron can be transfered within several electron acceptor molecules, through a chain of redox reactions to PSI to reach the final electron acceptor $NADP^+$, forming NADPH.

The release of an electron from the PSII reaction center leaves a positive charge which breaks the water molecules in the thylakoid's lumen[18] (Fig. 2.1) into H^+ ions and oxygen atoms to recoup the lost electron of the reaction center. The resulting oxygen molecules are released by the leaves as a byproduct of splitting H_2O by PSII. Consequently, the proton (H^+) concentration gradient between thylakoid lumen and stroma causes a proton flow which provides the required energy for ATP synthesis.

[17] A non-radiative transition between two energy states with different spin multiplicity such as a singlet to a triplet state transition or vice versa [Marian, 2012].

[18] the inner membrane space of a cellular component or structure including a thylakoid

The produced ATP and NADPH molecules are finally utilized as energy sources in the dark reactions (explained in 2.1.1).

In absence of drastic light variation or stress, most of the absorbed radiation is (as intended) used for chemical work known as Photochemical Quenching (PQ). However, as it has been mentioned before, other than transferring the excitation energy to the reaction center, there are several ways for releasing the excitation energy and descending back to the ground state for a Chl molecule. Among these, formation of a triplet excited state is a possibility plants avoid through NPQ and heat dissipation mechanisms.

Non-Photochemical Quenching (NPQ)

Light absorption by plants plays a key role in photosynthesis. PAR can vary drastically from day to day as well as seasonally. In order to compensate for the excessive absorbed energy, plants have developed some mechanisms to protect themselves from possible damages and to optimize photosynthetic Light Use Efficiency LUE_p. To avoid exposure to extreme radiation, plants adjust their light harvesting through movements of the leaves as well as changing the length of their antennae by varying the number of pigments. Therefore, long-term stress can change the spectral shape of the canopy reflectance by modifying the amount of absorbing pigments (e.g. bleaching). Such effects can be persistent from days to months (Fig. 2.4b).

Besides modifying the absorption process, to cope with short-term stress (e.g. excessive illumination) some non-photochemical mechanisms have been developed to quench the excess light energy which is already absorbed. Although the probability of a transition between the first singlet state and the first triplet state through inter-system crossing is low, highly reactive oxygen free radicals can still form, damaging the plant cells. Thus, when the absorbed energy is not directly utilizable for chemical work, it has to be quenched via a thermal dissipation processes known as NPQ. Many plants release the excess energy non-photochemically, by changing the light harvesting pigments within the antennae to control their interactions in order to form energy traps [Müller et al., 2001]. For instance, the so-called Xanthophyll cycle as a NPQ process, refers to the conversion of some pigments within the antenna to those with a different absorption peak, being able to block the energy transfer chain by absorbing and releasing the excess energy as heat. In a PS exposed to extreme radiation, some of the so-called violaxanthin molecules within the antenna are converted into other forms known as zeaxanthin pigments which are unable to transfer the excess energy to the reaction center and dissipate it as heat. This process is reversible when illumination is inadequate.

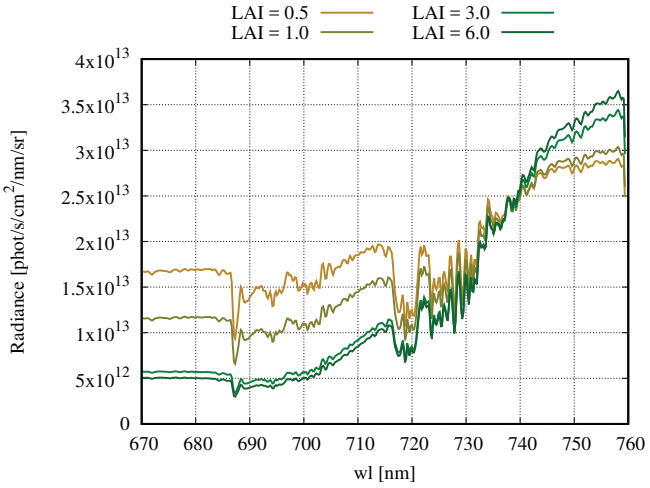

(a)

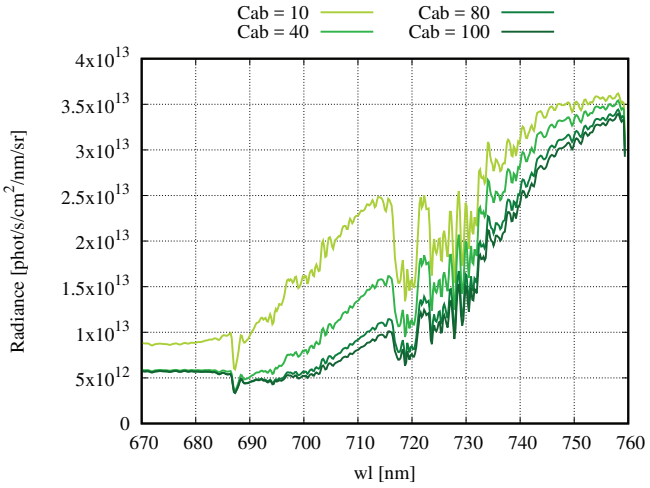

(b)

Figure 2.4: (a): The TOA radiance simulated based on the variation of LAI from 0.5 to 6 m^2/m^2 for a canopy assuming the Chl concentration to be 80 $\mu g/cm^2$. Increasing the vegetation concentration represented by LAI shows higher steepness in the red-edge. (b): The TOA radiance simulated based on the variation of Chl concentration from 10 to 100 $\mu g/cm^2$ for a canopy assuming the LAI to be 3 m^2/m^2. Increasing the Chl concentration within the canopy (larger number of photo-absorbers) shows higher steepness in certain regions of the red-edge.

NPQ does not refer to a process in which no photo-chemical reaction is involved, but suggests that the "quenching" of energy is not due to chemical work or photo emission. Thinking of NPQ as the major way to dissipate the excess energy suggests a positive correlation between NPQ and fluorescence emission. On the other hand, the energy which is not being quenched photochemically or non-photochemically is

emitted to the environment as fluorescence. Therefore, Chl fluorescence is a radiative form of energy loss for an excited Chl* and an important indicator of the photosynthetic efficiency of plants. This implies that NPQ can also have a negative correlation to the Chl fluorescence emission. Thus, additional measurements of thermal dissipation are necessary to translate Chl fluorescence to photosynthetic activity [Van der Tol et al., 2009a].

2.1.4 Terrestrial Chlorophyll fluorescence

Tol et al. [2014] showed that NPQ is the main way of quenching the excess energy and therefore k_{NPQ} varies mostly due to over-excitation while k_F remains almost unchanged or shows a slight decline due to an increase in the NPQ. A photochemical or photo-physical process such as fluorescence emission or oxidation of Chl molecules in a PS, is defined through a quantum efficiency or yield (Φ), showing the probability of the excited state taking a certain pathway to the ground state.

Plants, being exposed to sun radiation emit Sun-Induced plant Fluorescence (SIF) consisting out of two broad-band spectral peaks in the spectral wavelength range of red and far-red ($\sim$ 650-800 nm). The magnitude of SIF ranges from a few to several tenths mW/m^{-2}sr^{-1}nm^{-1}, suggesting it is a weak signal ($\sim$ 2%) compared to the reflected radiance from the canopy (Fig. 2.5). SIF has two maxima at $\sim$ 680 and 750 nm accumulated from the fluorescence emitted by both photosystems. PSII, has a larger contribution to the red-SIF peak emission while PSI is the main reason for SIF in far-red spectral range. This could be understood based on their spectral absorption peaks.

For chlorophyll fluorescence, the quantum yield (Φ_F) is defined as the ratio of emitted fluorescence photons per absorbed photon by the pigments. Therefore, for an absorbed quantum of energy, the quantum yield (efficiency) of each possible process is defined with respect to all the processes in which the energy can be released. The quantum efficiency of SIF can be seen in Eq. 2.4.

$$\Phi_F = \frac{k_F}{k_T + k_F + k_D + k_{NPQ} + k_{ISC}} \tag{2.4}$$

Despite showing a relatively high quantum yield of 15- 30% in vitro, Chl fluorescence has a lower quantum yield ($\sim 0.5 - 5\%$) in vivo [Latimer et al., 1956]. This difference can be explained by energy dissipation through PQ and NPQ in vivo. The spectral shape of SIF at the canopy level is highly affected by the vegetation structure and physiological properties. Light penetration in the canopy depends on the PS composition of the individual leaves, the overlap of the red-SIF and the Chl absorption spectra, as well as the re-absorption of red-SIF (mainly by PSI). All together, these properties

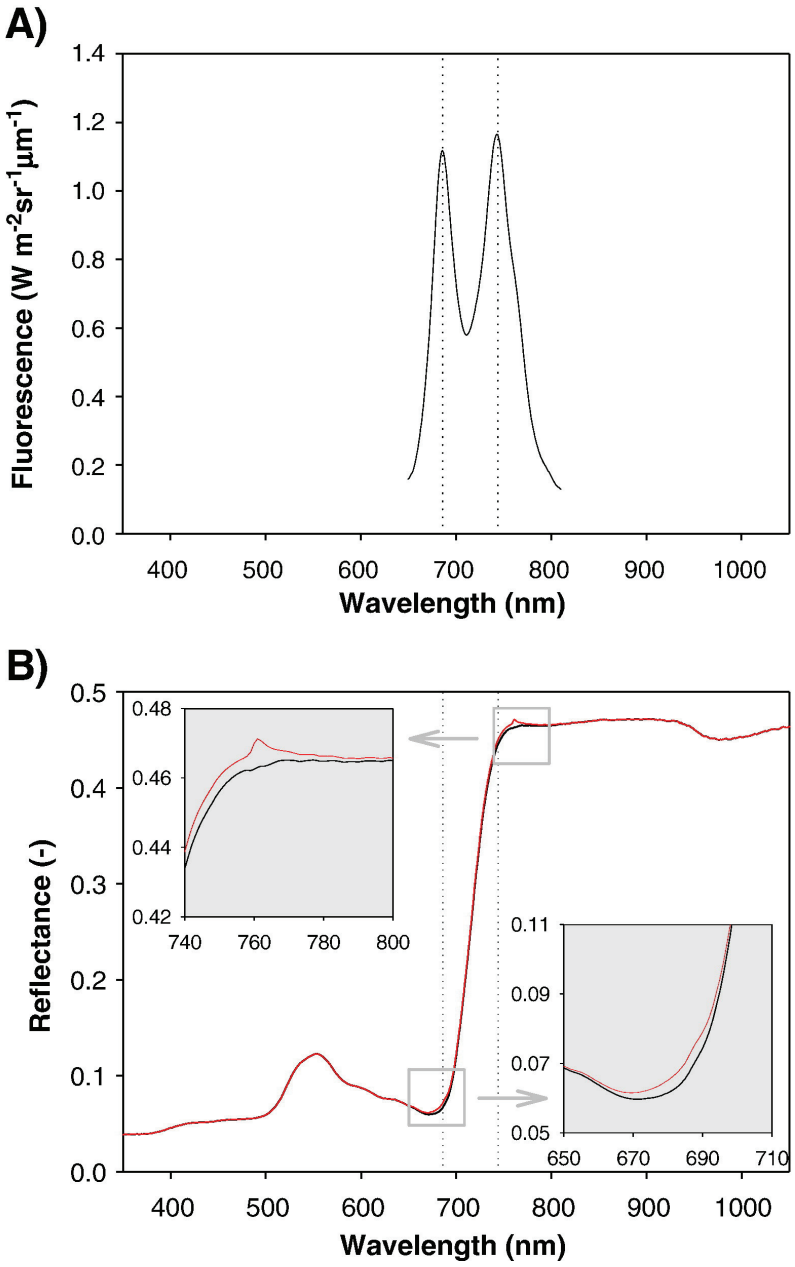

Figure 2.5: (A) The typical spectral shape and magnitude of SIF (B) The relative magnitude of the SIF emission on the reflectance from canopy. As shown, the reflectance at TOA is not significantly affected by SIF and it is challenging to decompose its effect from the reflectance[Meroni et al., 2009]

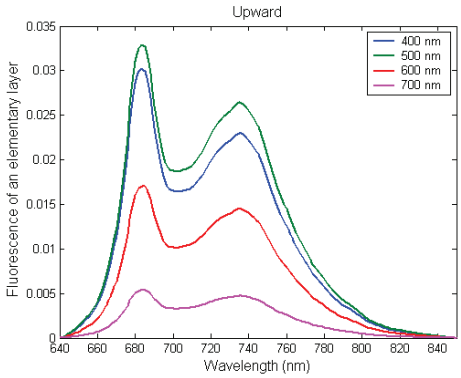

Figure 2.6: Modeled upward induced chlorophyll fluorescence of an elementary layer calculated at four wavelengths of excitation [Miller et al., 2005].

cause a significant difference between the overall spectral shape of SIF at the canopy level and leaf level [Porcar-Castell et al., 2014, and references therein].

Sharing one energy source, any change in the yield of SIF emission is followed by a change in the photosynthetic yield. Thus, SIF is an important indicator of photosynthetic efficiency of plants, showing a stress-related disturbance in the photosynthesis even before a visible change occurs in the canopy [Joiner et al., 2011]. It has been shown by Daumard et al. [2010] that measured SIF over a canopy is closely related to the stress (e.g. drought) the plants are exposed to, even though chlorophyll concentration or the *greenness* of the canopy remains unchanged.

Fluorescence emission from a chlorophyll molecule exposed to light, can be seen as the accumulation of several fluorescence signals generated from absorption of monochromatic radiation by the molecule. Fig. 2.6 illustrates modeled fluorescence from a layer of Chl molecules based on different excitation wavelengths. Accordingly, SIF at the canopy level (for each spectral wavelength point, λ_{em}) can also be written as the sum of the fluorescence signals generated from all excitation wavelengths (λ_{ex}) within the PAR spectral region:

$$\mathcal{F}_b(\lambda_{em},t) = e(\lambda_{em},t)\int_{\lambda_{ex}} \Phi_F(\lambda_{ex},\lambda_{em},t)\, f\text{APAR}(\lambda_{ex},t)\, I(\lambda_{ex},t)\, d\lambda_{ex}\,. \quad (2.5)$$

$\mathcal{F}_b(\lambda_{em},t)$ is the fluorescence emission spectrum at each moment and e represents the fraction of SIF leaving the canopy [Joiner, 2014]. Since the excitation spectrum for fluorescence may contain somewhat more from ultraviolet wavelengths than the excitation spectrum for photosynthesis, their corresponding PAR spectra are not exactly the same [Chappelle and Williams, 1987, Rosema et al., 1991, Middleton et al., 2008]. However, the difference is negligible and APAR for fluorescence can be safely

approximated by APAR for photosynthesis. A simplified version of the Eq. 2.5 has been utilized by Louis et al. [2005], Berry et al. [2012], Joiner et al. [2014]:

$$\mathcal{F}_b(t) = e(t)\Phi_F(t)\,\mathrm{APAR}(t)\,, \tag{2.6}$$

Therefore, comparing Eq. 2.1 and 2.6 one can see that GPP is related to SIF emission [Joiner, 2014] and the relationship between them can be written as:

$$\frac{GPP(t)}{\mathcal{F}_b(t)} \propto \frac{\mathrm{LUE}_p}{e(t)\,\Phi_F(t)}\,. \tag{2.7}$$

Bearing in mind that the LUE_p is directly related to the quantum yield of photosynthesis ($\Phi_P = k_T\,(k_T + k_F + k_D + k_{NPQ} + k_{ISC})^{-1}$), Eq. 2.7 can also be written as

$$\frac{GPP(t)}{\mathcal{F}_b(t)} \propto \frac{\Phi_P(t)}{\Phi_F(t)}\,. \tag{2.8}$$

Tol et al. [2014] stated that Φ_F has a linear relationship with Φ_P depending on the species and illumination conditions. As stated by Berry et al. [2012], under extreme radiation, the ratio between Φ_P and Φ_F tend to remain constant which implies that *there is a linear relationship between GPP and SIF emission.*

Chlorophyll fluorescence has been studied in laboratories and fields using active and passive measurement methods. Active measurement techniques utilize artificial light sources (e.g. laser) to excite Chl molecules and have been helpful to the understanding the photosynthetic responses of plant cells to different stress conditions (e.g. Kolber et al. [2005]). In vitro measurements of Chl fluorescence have been mainly based on active measurements using Pulse Amplitude Modulated fluorometry (PAM) in which a pulse of light excites the Chl molecules and the emitted fluorescence is observed accordingly [Porcar-Castell et al., 2014, and the references therein]. However, to track vegetation photosynthetic activity in vivo, passive techniques are beneficial as the Sun is the excitation energy supply. Moreover, for passive remote-sensing approaches larger spatial coverage is achieved.

2.2 Radiative transfer through the atmosphere

As the canopy is *remote* from the energy source (Sun) and the detector (instrument), the signal received by a space-borne instrument at TOA, does not only contain information about the Earth's surface, but is influenced by the atmosphere as well. Therefore to remotely sense the surface, the interaction of light with the atmosphere and the surface has to be understood.

In spite of absorption and scattering by the terrestrial atmosphere, light reaching the canopy is a fraction of the incident radiation transmitted through the atmosphere. The rate of energy transfer is the radiant *flux*. Solar irradiance (I_0) for any spectral wavelength range of [λ, $\lambda + d\lambda$] and any differential surface area, dA, is defined as the sun's radiant flux intercepted by dA per any time interval of dt. The unit of irradiance (in remote sensing) is usually $W\,m^{-2}\,nm^{-1}$.

Radiance however, can be defined as the irradiance per solid angle $d\Omega$. The monochromatic radiance is defined as the energy that is propagated through the surface dS generated by dA in a direction perpendicular to the incident direction ($dS = cos\theta \times dA$);

$$dI(\lambda) = \frac{dE(\lambda)}{dS\,d\lambda\,dt\,d\Omega}. \tag{2.9}$$

The radiance is a directional quantity in $Wm^{-2}nm^{-1}sr^{-1}$. What a space-borne instrument measures at TOA is radiance which can be computed through radiative transfer modeling. The interaction between radiance and the atmosphere/surface is modeled by solving the radiative transfer equation. The parameters playing the main role in the radiative transfer equation are absorption, scattering and emission by the atmosphere and the Earth's surface.

When an electromagnetic wave passes through the atmosphere, the incident photons may collide with the atoms, molecules, particulate matter and ions. Having the right energy quanta, these photons are either absorbed by the objects or are scattered into a direction other than the incident direction. The sum of scattered and absorbed photons is also called extincted photons. Assuming the atmosphere to be a homogeneous medium, the atmospheric transmittance is defined as the fraction of the incident radiance passing through the atmosphere in its incident direction and is described by the **Beer-Lambert's law**:

$$\begin{aligned} \frac{dI(\lambda)}{dS} &= -\sigma(\lambda)\,\rho\,I(\lambda), \\ \Rightarrow I(\lambda) &= I_{inc}\,exp(-\sigma(\lambda)\,\rho\,S)\,. \end{aligned} \tag{2.10}$$

I_{inc} is the unattenuated and $I(\lambda)$ the transmitted (reduced) spectral intensity. $\sigma(\lambda)$ is the extinction cross-section, ρ the density of the medium interacting with the photons and S, the path length of the spectral beam (medium geometrical thickness).

In the following the individual contributions to the radiative transfer equation (i.e. absorption, emission and scattering) are briefly discussed in order to formulate an

underlying framework, i.e. the radiative transfer equation which describes all governing processes.

2.2.1 Absorption

As explained in section 2.1.3, a photon with a specific wavelength is absorbed by an atom/molecule if its energy equals the energy difference between two energy states of the atom/molecule. Accordingly, each molecule is only capable of absorbing radiation of specific wavelengths.
Absorption in the atmosphere follows Beer-Lambert's law, explained by the absorption cross-section $\sigma_a(\lambda)$ which shows the probability of incident radiation to be absorbed by a *particle*[19].
The term $\rho\sigma_a(\lambda)S$ is often called the absorption Optical Depth ($\tau_a(\lambda)$) and it depends on the concentration of the absorbing particles in the medium: $d\tau_a(\lambda) = \rho\,\sigma_a(\lambda)\,dS$.
Accordingly, Beer-Lambert's law can be rewritten for case of absorption as:

$$\frac{dI(\lambda)}{d\tau_a(\lambda)} = -I(\lambda). \tag{2.11}$$

Fraunhofer absorption lines (discussed in section 2.3) result from the absorption within specific wavelength bands in the Sun's photosphere. In terrestrial atmosphere, light is absorbed by gas molecules and particulate matter resulting in terrestrial absorption lines in the radiance spectrum.

2.2.2 Emission

Although emission in the atmosphere is not significant within the spectral range of SIF emission, the reader should note that (as a general rule) the molecules along the light path also emit radiative energy depending on their temperature according to the *Stefan-Boltzmann*'s law. The emitted radiance can be formulated as follows:

$$E_\lambda(T) = \epsilon_\lambda(T)B_\lambda(T). \tag{2.12}$$

Since the atmosphere does not have black body characteristics within the spectral region of interest for this work, $\epsilon_\lambda(T)$, the emissivity of a molecule at wavelength λ and temperature T, is smaller than one ($\epsilon_\lambda < 1$).

Absorption and emission of radiative energy by atmospheric particles are connected by the Kirchhoff's law which states that for any medium in thermodynamic equilibrium

[19] using the word *particles* does not refer to particulate matter and aerosols here and is a physical concept.

emissivity is directly related to the ability of the medium to absorb radiation. Therefore Beer-Lambert's law (Eq. 2.11) including absorption and emission by a medium can be modified as:

$$\frac{dI(\lambda)}{d\tau_a(\lambda)} = B_\lambda(T) - I(\lambda). \tag{2.13}$$

2.2.3 Scattering

Scattering is the redirection of electromagnetic radiation from a straight trajectory, which occurs when an incident light ray encounters an obstacle or inhomogeneity. Gaseous molecules and particulate matter scatter electromagnetic radiation in the atmosphere through different scattering regimes depending on the so-called size parameter; $\alpha = \frac{\pi.D_p}{\lambda}$. D_p is the diameter of the molecule/particle (assumed to be spherical for simplicity) and λ is the scattering wavelength.

From the classical electrodynamical point of view, when an incident photon interacts with a particle, the electric field of the incident ray is the primary source of perturbation of the particle's electron distribution i.e. polarizability. This induces a dipole moment which is itself a source of electromagnetic radiation, thereby resulting in scattered light. The scattering process in which the scattered photon shares the same wavelength (energy) as the incident photon is known as elastic scattering.

Elastic Scattering

Elastic scattering occurs when energy exchange is negligible. Depending on the size parameter, the main elastic scattering regimes are Rayleigh ($\alpha \ll 1$) and Mie ($\alpha \approx 1$) scattering. Particles larger than the incident wavelength ($\alpha \gg 1$) scatter the light geometrically.

Mie scattering occurs for particles with $\alpha \approx 1$ such as dust, pollen or smoke as well as water droplets within the clouds. The dependence of Mie scattering on the incident wavelength is rather weak. Therefore, within the spectral wavelength range in which $\alpha \approx 1$, the scattering efficiency is not strongly bound to the energy of the scattering photons.

It is worth mentioning that the Mie theory provides a general scattering solution that holds for several sizes and wavelengths. Electromagnetic radiation scattered from any small, non-absorbing, spherical and dielectric particle can be described by Mie theory. For the particular case of Mie scattering, the intensity of the scattered light has

a wavelength dependence of λ^{-a}, in which $0 \leq a < 4$. Rayleigh scattering regime is a special case of Mie theory.

Rayleigh scattering is based on the assumption that an incident photon is interacting with a small, non-absorbing, spherical and dielectric particle.

The dipole moment (p), induced by the electromagnetic wave to the particle is defined as $\vec{p} = \alpha_p \vec{E_0}$, in which α_p is the polarizability of the particle. Accordingly, the scattered electric field at the distance r from the particle is defined as

$$\vec{E} = \frac{1}{c^2}\frac{1}{r}\frac{\partial \vec{p}}{\partial t} sin(\gamma), \tag{2.14}$$

where γ is the angle between $\vec{p}$ and the scattering direction. Applying equation 2.14 to the induced dipole moment $\vec{p} = \vec{p_0} exp(-ik(r - ct))$ the induced electric field is:

$$\vec{E} = -\vec{E_0} k^2 \alpha_p \frac{exp(-ik(r - ct))}{r} sin(\gamma), \tag{2.15}$$

in which $k = \frac{2\pi}{\lambda}$ is the wave number. Knowing that the light intensity is defined as the squared amplitude of the electric field, the intensity of the scattered ray depends on the wavelength as follows:

$$I \propto \frac{\alpha_p^2}{r^2}\left(\frac{2\pi}{\lambda}\right)^4, \tag{2.16}$$

implying that the scattered intensity is inversely proportional to the wavelength to the fourth power; $I \propto \lambda^{-4}$. Therefore, the scattering efficiency is significantly higher for photons of higher energy (shorter wavelength) than lower energy (longer wavelength).

Inelastic Scattering

The incident photon can also interact with the molecules leading to a gain or loss in its energy, so that the scattered photon has a different wavelength than the incident one. The most widely known type of inelastic scattering is known as Raman scattering (RS) [Timofeyev and Vasil'ev, 2008].

Inelastic scattering cannot be fully described by classical electrodynamics and has to be seen from quantum mechanics perspective. From this point of view, scattering is defined as the excitation of a molecule to a virtual energy state by absorbing a photon and an almost coincident de-excitation to a lower energy state by emitting a photon which can have higher (Stokes scattering), lower (Anti-Stokes scattering) or the same energy as the incident photon (Rayleigh scattering). The latter is also known as elastic

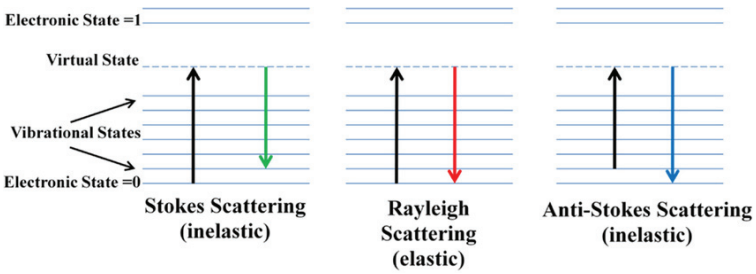

Figure 2.7: Elastic vs. inelastic scattering described by the virtual energy levels of the scattering particle [Lupoi, 2012]

scattering (Fig. 2.7). In other words, due to quantized energy transmission, the molecule can lose some energy to the scattered photon or gain energy from it.

As it has been mentioned before, most of light scattering in the atmosphere is elastic, however, a small portion of the photons is scattered at different wavelengths than the incident. Vibrational Raman Scattering (VRS) and Rotational Raman Scattering (RRS) are two forms of RS. The internal energy of a molecule E_{int} consists out of the electronic (E_{el}), vibrational (E_{vib}) and rotational (E_{rot}) components:

$$E_{int} = E_{el} + E_{vib} + E_{rot} \tag{2.17}$$

The effect of RRS in the atmosphere is also referred to as the Ring effect [Grainger and Ring, 1962] and has an in-filling effect on Fraunhofer and telluric absorption lines (for further reading see e.g. Kattawar et al. [1981], Vountas et al. [1998]). In essence, the in-filling effect due to RS can be explained by the spectral redistribution of the scattered photons which (comparable to an additive signal such as fluorescence) can change the relative depth of an absorption line. Thus, the importance of RS in SIF retrieval is due to the fact that both SIF and RS cause comparable variations in the solar Fraunhofer lines. The impacts of both are referred to as in-filling, despite having fundamentally different mechanisms.

As it is shown in Fig. 2.8, the energy difference between electronic energy states is larger than of vibrational states and both of them are larger than rotational states. Considering the width of Fraunhofer lines within the visible and far-red spectral region and the typical atmospheric temperature ranges, rotational transitions are more likely to fill-in the Fraunhofer lines in this spectral region. Therefore, one can conclude that the contribution of VRS is comparatively small and RRS is more relevant to the scope of this study and must be taken into account (see for instance Sioris et al. [2003] and Lampel et al. [2015]).

To summarize, the scattering process can be formulated in the radiative transfer

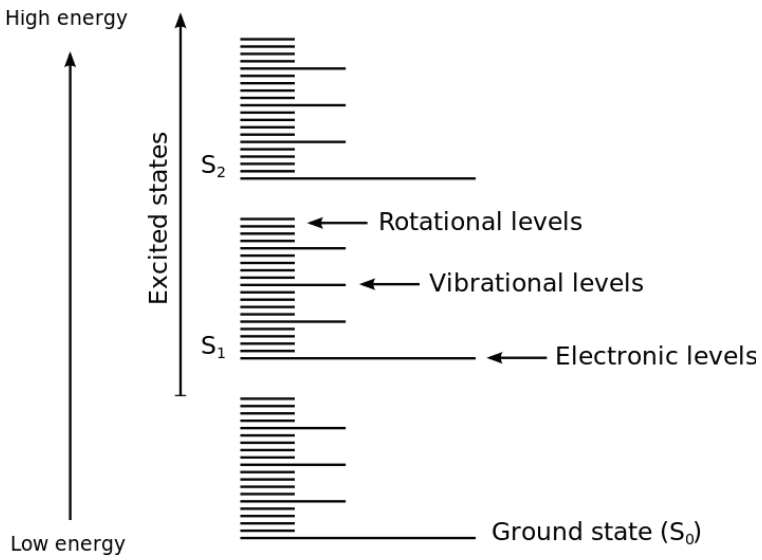

Figure 2.8: Electronic, vibrational and rotational energy levels of a molecule [Lichtman and Conchello, 2005]

equation (as in Eq. 2.13):

$$\frac{dI(\lambda)}{dS} = -\sigma_s(\lambda)\rho I(\lambda) + \frac{\sigma_s(\lambda)\rho}{4\pi}\int_{4\pi} P(\Omega,\Omega')I(\lambda,\Omega')d\Omega', \tag{2.18}$$

in which $-\sigma_s(\lambda)$ represents the scattering cross section and $-\sigma_s(\lambda)\,\rho$ is the extinction of the incident radiance due to scattering. The first term is similar to Beer Lambert's law (single scattering), while the second term expresses the directional dependence of scattering (multiple scattering). $P(\Omega,\Omega')$, also known as the phase function. This is the probability density function by which photons are being scattered from the solid angle Ω' to the solid angle Ω. Therefore, due to the conservation of energy, the following equation holds:

$$\frac{1}{4\pi}\int_{4\pi} P(\Omega,\Omega')I(\lambda,\Omega')d\Omega' = 1. \tag{2.19}$$

2.2.4 Radiative transfer equation

The atmospheric radiative transfer equation can be derived from combining absorption, emission and scattering effects from Eq. 2.13 and 2.18:

$$\frac{1}{\rho}\frac{dI(\lambda,\Omega)}{dS} = -(\sigma_a(\lambda)+\sigma_s(\lambda))\,I(\lambda) + \sigma_a\,B_\lambda(T) + \frac{\sigma_s(\lambda)}{4\pi}\int_{4\pi} P(\Omega,\Omega')I(\lambda,\Omega')d\Omega'. \tag{2.20}$$

Accordingly, the extinction optical depth can be defined as $d\tau(\lambda) = (\sigma_a(\lambda) + \sigma_s(\lambda))\,\rho\,dS$. Therefore, the RTE can be rewritten as:

$$\frac{\partial}{\partial\tau}I(\lambda,\tau,\Omega) \;=\; -I(\lambda,\tau,\Omega) \;+\; \omega_a(\tau)\,B_\lambda(T) \;+\; \frac{\omega_s(\tau)}{4\pi}\int_{4\pi} P(\tau,\Omega,\Omega')\,I(\tau,\Omega')\,d\Omega'\;, \tag{2.21}$$

in which the $\omega_s(\tau) = \sigma_s/(\sigma_a+\sigma_s)$ and $\omega_a(\tau) = \sigma_a/(\sigma_a+\sigma_s)$ are known as the absorption and single scattering *albedo*s, respectively. In the framework of this dissertation, Eq. 2.21 is solved to describe the propagation of SIF emission through the terrestrial atmosphere.

The boundary conditions to solve Eq. 2.21 are set based on the following:

- Monochromatic unpolarized incident solar irradiation at the TOA (I_0) provided by Chance and Kurucz [2010].
- The solar zenith angle ϑ_0 is defined as the angle between the positive direction of the z-axis (from the center of the Earth) and the direction towards the sun (Fig. 2.9).
- The x-axis of the basic coordinate system points away from the Sun. This means that the azimuthal angle of the solar beam is assumed to be zero ($\varphi_0 = 0$) and the relative azimuth angle is the only azimuthal angle taken into account.
- The intensity of the direct solar irradiance is $I_0\,\delta(cos\vartheta - cos\vartheta_0)\delta(cos\varphi - cos\varphi_0)$, in which $\delta(cos\vartheta - cos\vartheta_0)$ and $\delta(cos\varphi - cos\varphi_0)$ are the Dirac functions [Korn and Korn, 1968].
- The direct radiation is modeled in a spherical atmosphere, while the diffused radiation is calculated in pseudo spherical geometry.

Consequently, the upper boundary condition set for solving the Eq. 2.21 is:

$$I(0,\vartheta,\varphi) = I_0\,\delta(cos\vartheta - cos\vartheta_0)\delta(cos\varphi - cos\varphi_0) \tag{2.22}$$

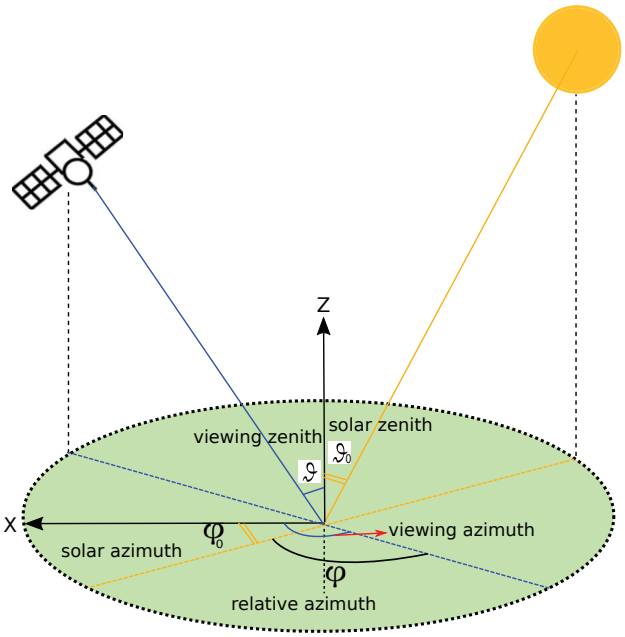

Figure 2.9: The measurement geometry of satellite observations in nadir mode as assumed within this study. The Z axis is the normal vector of the surface originating from the center of the globe. The solar zenith and viewing zenith angles are defined as the angle between the Z axis and the direction from the measurement target (on the Earth's surface) towards the sun and satellite respectively. The solar azimuth angle (φ_0) is defined as the angle between the positive X axis and the direction pointing away from the sun. The viewing azimuth angle is also defined as the angle between a hypothetical line pointing away from the satellite and positive X axis. However, assuming the X direction to be the horizontal line pointing away from the sun, $\varphi_0 = 0$ and the φ can be defined as the relative azimuth angle.

in which ϑ and φ represent any zenith and azimuth angle respectively. To define the lower boundary condition, a brief description of the assumptions on the Earth's surface reflectance is needed. The Earth's surface reflectance depends on both viewing and illumination directions. The term Bidirectional Reflectance Distribution Function (BRDF) represents the surface reflectance, which is defined as the ratio between the reflected radiance from the surface ($I_b(\vartheta_r, \varphi_r)$) and the incident irradiance at the surface ($I_{0b}(\vartheta_i, \varphi_i)$):

$$\rho_s(\vartheta_i, \varphi_i, \vartheta_r, \varphi_r) = \frac{I_b(\vartheta_r, \varphi_r)}{I_{0b}(\vartheta_i, \varphi_i)}, \tag{2.23}$$

with ϑ_i and ϑ_r being incident and reflected zenith angles in the same way as the φ_i and φ_r are the incident and reflected azimuth angles.

The Lambertian reflectance is a special type of BRDF reflectance and is defined as the reflection from a surface which reflects light uniformly into all directions (isotropic). In fact, the intensity of the reflected light is proportional to $cos\vartheta_r$. However, at each viewing zenith angle the received light intensity by a detector is proportional to $cos^{-1}\vartheta_r$. Therefore, the measured light intensity is not angular dependent. Considering the typical spatial resolutions and characteristics of the instruments in the framework of this dissertation, the Earth's surface can safely be considered to be Lambertian due to its diffusive characteristic. Therefore, at each spectral wavelength the surface reflectivity can be considered constant (A).

Hence, the lower boundary condition is defined as follows:

$$I(\tau_0, \Omega) = \frac{A}{\pi} \int_0^{2\pi} \int_0^1 I(\tau_0, \Omega') cos\vartheta' \, d\cos\vartheta' \, d\varphi' + \mathcal{F}_b \, , \; cos\vartheta < 0 \tag{2.24}$$

in which $\mathcal{F}_b$ is the fluorescence emission at the top of canopy (see section 3.1.1) and A is the Lambertian surface reflectance.

2.3 Measuring terrestrial Chlorophyll fluorescence

The current approaches of SIF measurements can be categorized based on their spatial coverage (e.g. field, airborne and satellite-based measurements) or the utilized techniques (e.g. *radiance-based* and *reflectance-based* methods) [Meroni et al., 2009].

Vegetation spectral indices (VI) are dimensionless quantities aiming to show the green vegetation coverage. VI mainly takes advantage of the variation in reflectance at

two different wavelength intervals.
The Difference Vegetation Index as the simplest VI relies on the drastic increase in reflectance of vegetation over the red-edge:

$$\text{DVI} = \rho_{NIR} - \rho_{Red}$$

in which ρ_{NIR} and ρ_{Red} are the reflectance in the NIR and red respectively. Likewise, the Normalized Difference Vegetation Index (NDVI) is:

$$\text{NDVI} = (\rho_{NIR} - \rho_{Red})/(\rho_{NIR} + \rho_{Red})$$

in which $(\rho_{NIR} + \rho_{Red})$ represents the average reflectance within the red-edge. The advantage of vegetation indices such as NDVI is that they show a positive correlation with important vegetation properties such as LAI, leaf chlorophyll content and fAPAR. Daumard et al. [2010] pointed out that although NDVI is an indicator of the vegetation greenness, unlike SIF, it is not representative for vegetation stress.

The relationship between SIF and photosynthetic efficiency can be studied by exploiting vegetation indices as additional information as well as comparison references for the retrieved results [Walther et al., 2015, and references therein]. The so-called *radiance-based* measurement techniques of the SIF are being widely used. A well-known measurement method for SIF is the **Fraunhofer Line Depth (FLD)**. FLD takes advantage of the so-called infilling of Fraunhofer lines [20] by SIF. As it is shown in Fig. 2.10, the solar spectrum has a spectral structure due to absorption in the solar photosphere (see 2.2.1). SIF, as an additive signal, varies the fractional depth of the solar Fraunhofer lines as well as the telluric absorption features (caused by gaseous absorption in Earth's atmosphere). Fig. 2.10 shows the resultant in-filling effect of SIF on a Fraunhofer line. The net infilling of SIF photons can be seen as a relative amplification of the signal in the Fraunhofer line depth.

Assuming $I(\lambda_{in})$ and $I(\lambda_{out})$ to be the measured radiances in the spectral points inside and outside of a Fraunhofer line respectively, one can formulate them as follows:

$$\begin{cases} I(\lambda_{in}) = \frac{1}{\pi} \cdot a(\lambda_{in}).I_0(\lambda_{in}) + SIF(\lambda_{in}) \\ I(\lambda_{out}) = \frac{1}{\pi} \cdot a(\lambda_{out}).I_0(\lambda_{out}) + SIF(\lambda_{out}) \end{cases} \tag{2.25}$$

in which λ_{in} and λ_{out} represent the spectral points inside and outside of the Fraunhofer line and a is the fraction of the radiance reflected from the target for each wavelength. Correspondingly, *SIF* at each wavelength (λ) point represents the additive radiance due

[20] named after Joseph Fraunhofer, 1817.

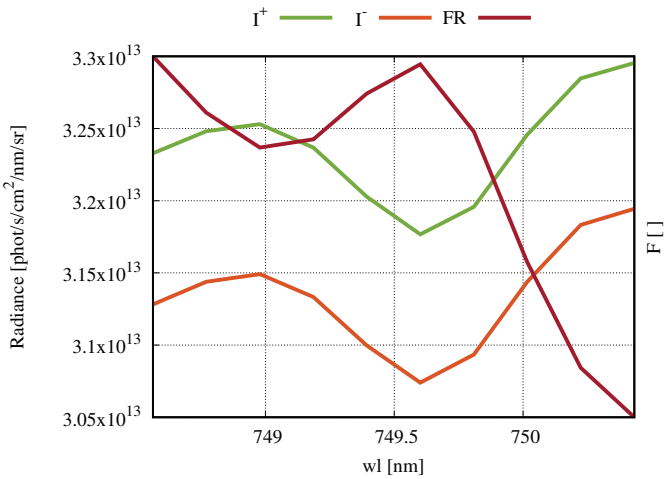

Figure 2.10: The infilling effect of fluorescence, simulated on a Fraunhofer line. The radiance in presence (I^+) and absence (I^-) of fluorescence is shown in orange and green respectively. The fractional depth of the Fraunhofer line (dark-red) is changed due to the additive signal.

to SIF emission. If a and *SIF* remain unchanged at λ_{in} and λ_{out}, solving the equation set 2.25 provides *SIF* in radiance units [Meroni et al., 2009]:

$$\begin{cases} SIF = \frac{I_0(\lambda_{out})I(\lambda_{in}) - I_0(\lambda_{in})I(\lambda_{out})}{I_0(\lambda_{out}) - I_0(\lambda_{in})} \\ a = \pi . \frac{I(\lambda_{out}) - I(\lambda_{in})}{I_0(\lambda_{out}) - I_0(\lambda_{in})} \end{cases} \tag{2.26}$$

Hence, fluorescence detection using FLD is generally possible using at least two spectral measurements inside and outside of a Fraunhofer line [Meroni et al., 2009]. Some FLD-based methods rely on a few spectral measurement points (i.e. multi-spectral) yet there are some FLD-based approaches which need contiguous measurements covering a continuous spectral window (i.e. hyper-spectral). The advantage of multi- and hyper-spectral approaches is that a and *SIF* (Eq. 2.26) do not remain unchanged at any selection of λ_{in} and λ_{out} [Alonso et al., 2008, Meroni and Colombo, 2006, and references therein]. Therefore, multi-spectral approaches rely on more than two spectral measurement points. By this means, the possibility of using multi-spectral imaging spectrometers such as MERIS [Guanter et al., 2007] and OLCI [Sabater et al., 2015] as well as exploiting hyper-spectral satellite measurements to retrieve SIF [Joiner et al., 2012, 2013a, Köhler et al., 2015b, Wolanin et al., 2015, etc.] are ensured. In the framework of this study, a retrieval method has been developed based on hyper-spectral satellite measurements involving the essential principles of FLD. Parts of the current work have been published in Khosravi et al. [2015].

Depending on the spatial measurement scale, the passive SIF-measurement methods

can be categorized as in-situ and remote sensing. The remote sensing methods could be from a relatively shorter distances (i.e. airborne) or long distance (i.e. spaceborne).

In-situ and airborne measurements

Passive in-situ measurement of vegetation fluorescence goes back to the 1970s and provides the opportunity to monitor vegetation fluorescence emission in vivo at leaf level and ecosystem scale [Meroni et al., 2009]. Measurements at different levels of detail are required to link leaf and canopy photosynthetic activity. Airborne detection of SIF bridges the in-situ field measurements to the spaceborne observations and can provide validation sources for global SIF measurements [Damm et al., 2014], although at the current level, it is still not practical due to the significant gap between spatial resolutions of local SIF measurements and the global retrievals. Nevertheless, in the past decade satellite-based passive measurements of SIF have been considered to be the best way of obtaining the spatial coverage needed for the estimation of photosynthetic activity at regional and global scales [Papageorgiou and Govindjee, 2004].

Space-borne measurements

As stated before, the main advantage of satellite-based remote sensing measurements of SIF is the possibility of having large spatial coverage which allows the mapping of fluorescence variations on a global scale.
It is worth mentioning that photosynthetic properties of the canopy are not the only factors affecting remotely sensed SIF, since measured SIF is highly dependent on atmospheric and measurement characteristics [Damm et al., 2014, Frankenberg et al., 2012, etc.], as well as instrumental effects [Frankenberg et al., 2011b, Damm et al., 2011, Guanter et al., 2010, Meroni et al., 2010].
Space-borne measurement of SIF, at its current level, is suitable for large (mainly) homogeneous vegetated regions (e.g. croplands and forests). Not to forget the importance of in-situ and airborne measurements of SIF and/or biological properties (e.g GPP) to complement the satellite based SIF retrievals [Papageorgiou and Govindjee, 2004].
So far, both hyper- and multi-spectral instruments have been used for SIF retrieval. The MEdium Resolution Imaging Spectrometer (MERIS) was the first multi-spectral instrument utilized by Guanter et al. [2007]. The Japanese Greenhouse gases Observing SATellite (GOSAT)[Hamazaki et al., 2005] has been used to retrieve SIF most frequently by Joiner et al. [2011, 2012], Frankenberg et al. [2011b] and Guanter et al. [2012]. Another spaceborne instrument utilized for SIF retrieval is the Orbiting Carbon Observatory 2 (OCO-2) [Frankenberg et al., 2014].

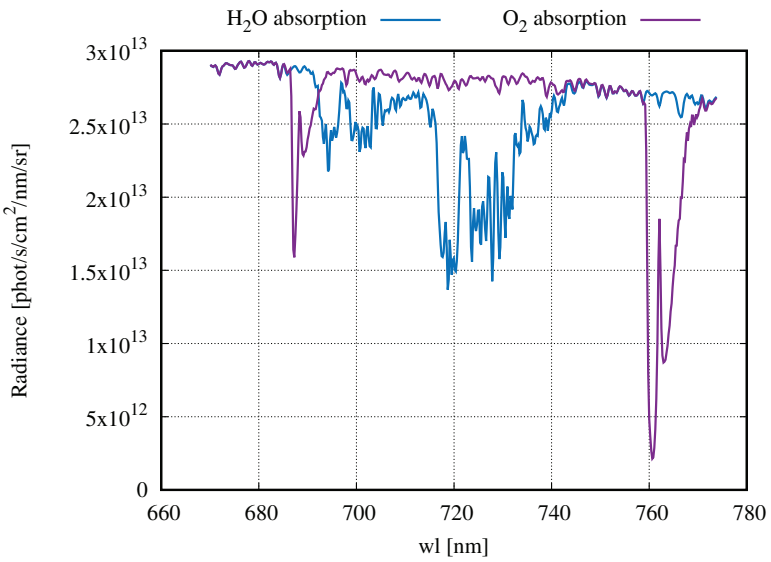

Figure 2.11: Examples of modeled radiances at TOA featuring the absorption signature of water vapor (blue) and oxygen (purple). The overlaps are where neither H_2O nor O_2 show significant absorption. The ground reflectance is considered to be Lambertian and wavelength independent.

The hyper-spectral spectrometers chosen for this study are the SCanning Imaging Absorption spectroMeter for Atmospheric CHartographY (SCIAMACHY), which has been used by Joiner et al. [2012], Wolanin et al. [2015], Köhler et al. [2015b] and Khosravi et al. [2015], as well as the Global Ozone Monitoring Experiment-2 (GOME-2) by Joiner et al. [2013a] and Joiner et al. [2016].

Fraunhofer and telluric absorption lines can be utilized while using hyper-spectral FLD-based approaches. Since SIF has a broad-band spectral signature coverage $\sim 600 - 800$ nm (Fig. 2.5), the main telluric absorbers within this wavelength range are O_2 and H_2O (see Fig. 2.11). Therefore, there have been several attempts to retrieve SIF using FLD-based methods from telluric absorption bands.

Particularly, two Oxygen absorption bands (O_2-B located around 687 nm and O_2-A around 760.4 nm) are often chosen, due to the spectral co-location of these bands with the peaks of the SIF emission spectrum (Fig. 2.12) [Moya et al., 2004, Guanter et al., 2007, Alonso et al., 2008, Daumard et al., 2010, etc.].

However, unlike solar Fraunhofer lines, the depths of O_2 absorption bands change with the measurement geometry and surface pressure [Guanter et al., 2010, Joiner et al., 2011]. Additionally, Frankenberg et al. [2012] showed that satellite-based measurements of SIF in the O_2-A band are error-prone. The impact of atmospheric and measurement properties (e.g. the aerosol optical depth, ground reflectance and surface

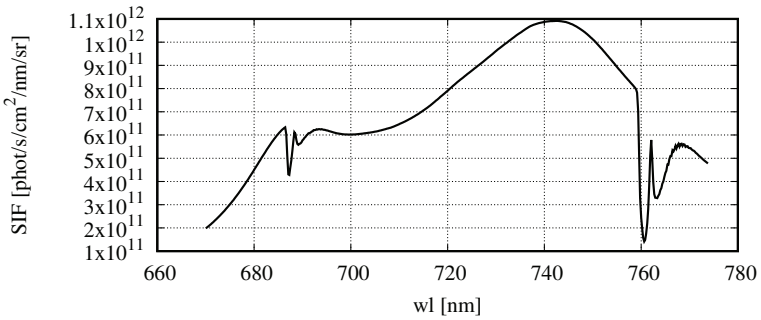

Figure 2.12: The double-peak of a sample SIF emission spectrum at TOA in presence of O_2 absorption (only). The Oxygen absorption of the upwelling SIF can be clearly seen in the O_2-A and -B absorption bands which are located near the second and first SIF maxima respectively.

pressure) can affect the spectral shape of the O_2 absorption bands and consequently the retrieved SIF values. Moya et al. have already stated in 2004 that since the upwelling radiance containing SIF is affected by absorption within the O_2-A spectral band, the SIF retrieval from this absorption line is disturbed. Meroni et al. [2009] have confirmed this outcome based on a thorough analysis of different FLD-based methods. They also mentioned a positive bias in the SIF retrieval from the spectral regions affected by O_2 bands due to BRDF effects. Recently, Ni et al. [2016] conducted a model-based study on the sensitivity of O_2-A and -B bands to the SIF retrieval utilizing different methods and concluded that for fitting methods such as the one used in this work, retrieving SIF from oxygen absorption bands is highly sensitive to the elevation and visibility (related to the aerosol optical depth [Sanders and de Haan, 2013]) of the measurement target.

The method proposed in this thesis is designed excluding the significant telluric absorption bands and is based only on the hyper-spectral measurements of solar Fraunhofer lines. There have been several studies aiming to retrieve plant fluorescence, analyzing its nature and characteristics, assessing its relationship to photosynthetic efficiency and canopy properties. Many of these studies have been conducted and published during the time period of the current work and were helpful to develop the retrieval method as well as interpreting the results. The next section is dedicated to a chronological summary of these relevant studies.

2.4 Studies performed so far

Aiming to study the possibility of decomposing SIF effects from those of RRS, Sioris et al. [2003] performed a model-study in order to investigate the relative fraction of Chl

fluorescence infilling of Fraunhofer lines in comparison with the relative fraction of the RRS, based on simulated data from nadir-viewing satellite geometry. In order to simulate Chl fluorescence and RRS effects for a number of cases, a radiative transfer model (MODTRAN [Berk et al., 2014]) was implemented. They concluded that RRS is not the dominant factor of the Fraunhofer lines filling-in and also its magnitude is smaller than fluorescence and is not comparable to fluorescence infilling in red and Near InfraRed (NIR) regions of the spectrum. Additionally, they have shown that errors due to Chl fluorescence uncertainties are larger than the errors introduced by RRS uncertainties. However, it has been stated that models should include both RRS and Chl fluorescence in order to simulate Fraunhofer lines filling-in realistically.

Focusing on regional applications and agricultural purposes, Baker and Rosenqvist [2004], reviewed the relationship between Chl fluorescence and the leaf photosynthetic performance using in-situ fluorescence imaging. They assessed the sensitivity of fluorescence to different plant statuses such as drought, freezing, salinity variation, etc. and concluded that having the right calibration and data selection, Chl fluorescence can be an informative tool to show the crop performance.

Based on the idea of measuring SIF from a telluric absorption band, Moya et al. [2004], introduced an instrument to measure SIF at the atmospheric O_2-A band ($\sim$ 760 nm). The instrument is designed based on FLD principle and could successfully show the feasibility of SIF remote sensing (for both air- and space-borne instruments). The authors mentioned that the upwelling radiance is partially absorbed by oxygen in the atmosphere which disturbs the signal. However, they suggested the Chl fluorescence to be a better indicator of absorbed PAR by the canopy than reflectance. It has been also pointed out that an additional vegetation reflectance index measurement would provide a complete signature of the vegetation.

Guanter et al. [2007], have attempted to develop a remote sensing technique of Chlorophyll Fluorescence, based on satellite instrumentation (MERIS)[21]. They have utilized a radiative transfer model, by which atmospheric parameters such as the atmospheric path radiances, the direct and diffused fluxes, the viewing zenith angle, the total atmospheric transmittance and the atmospheric spherical albedo are known and the unknowns are the surface reflectance and the fluorescence steady state. The use of Digital Elevation Model (DEM), MODTRAN-4 look-up tables (LUT) and the Fraunhofer Line Discriminator (FLD) principle used within O_2-A absorption band, allowed them to separate reflected and emitted radiances. They have proved a correlation between fluorescence signal and NDVI. It has also been shown that there is a clear agreement between the

[21] MEdium Resolution Imaging Spectrometer is an multi-spectral instrument which was on board EnviSat launched by ESA in 2002.

MERIS remote sensing retrieved ChF values and the reported values from NDVI.
Defining the vegetation apparent reflectance as the sum of vegetation reflectance and SIF, Campbell et al. [2007], have investigated the relative fractions of vegetation reflectance and fluorescence with vegetation apparent reflectance. They have studied the contribution of fluorescence and reflectance to the solar spectrum within 650-800 nm spectral range, at the foliate level and showed that the absolute contribution of fluorescence and maximum fluorescence at the apparent reflectance ranges between 4% and 15% in the region 670-690 nm. They have also shown that the contribution of fluorescence in different wavelengths consistently allows the classification of different vegetation species. It is stated that the maximum value of SIF is observed for 740 nm and is 4-6% of the incoming solar radiation. Their finding implies that the emitted fluorescence from different species can vary based on their physiological characteristics.
Amorós-López et al. [2008], assessed the best conditions to monitor SIF from a satellite-based instruments by analyzing the diurnal evolution of the vegetation fluorescence emission spectrum and its yield. The study was held on the leaf level, simulating two different species experiencing different stress conditions during summer and winter. Fluorescence yield showed a significant sensitivity to stress induced by both water and light and is highly affected by the measurement conditions. As water and light stress have their influential peak on fluorescence in different times of day, recommending the best time to measure SIF is reported to be difficult. However, the authors recommended mid-morning hours as the best measurement time based on their leaf-level measurements.
Alonso et al. [2008], proposed an improved FLD approach for decoupling Chl fluorescence from the measured radiance. Their method was applied on the O_2-A band (754-761 nm), where they argued that the magnitude of Chl fluorescence is comparable to the incoming radiation. The improved approach was to consider not only two wavelengths, inside the O_2-A band and on the edge for FLD implementation, but a continuous spectral region and retrieve fluorescence by adding correction coefficients to the basic Fraunhofer Line Discriminator (FLD) technique. They stated that the standard FLD method introduces a large overestimation of SIF, in magnitude and the diurnal cycle trend.
Shortly after, the outcomes of the CEFLES2 campaign (which took place on April to September 2007 in Southern France) were published by Rascher et al. [2009]. The CEFLES2 campaign was part of the Carbon Europe Regional Experiment Strategy, as a preparation project of the FLuorescence EXplorer (FLEX) satellite mission funded by European Space Agency (ESA). This work as a preliminary step for FLEX mission (which is formally approved by ESA in November 2015) had focused on providing

large scale and ground based measurements of SIF emissions and CO_2 fluxes based on passive remote sensing instrumentations. Furthermore, SIF estimations were spatially studied and validated, based on field laser induced fluorescence and the results were compared for different vegetation types. The campaign was designed to investigate if mesoscale SIF can be used to quantify carbon exchange processes at the same scale level and reduce modeling uncertainties when SIF is used as an input parameter.

As it started to gain attention by the scientific communities, SIF remote sensing through passive methods was assessed by Meroni et al. [2009]. A thorough analysis of radiance and reflectance-based methods as well as in-situ and remote sensing based approaches has been provided in their study. The authors reviewed several approaches from simple multi-spectral FLD methods to hyper-spectral fitting methods, which are shown to be more accurate even considering different levels of noise. They finally showed that the FLD technique in both oxygen absorption bands, leads to a positive bias in fluorescence estimation which cannot be easily avoided even implementing high spectral resolution data.

Moving from multi-spectral to hyper-spectral retrieval methods, Guanter et al. [2010], used O_2-A and O_2-B atmospheric absorption features to retrieve fluorescence signal. The obtained result was used in preparation of the FLEX concept as well. They used a data set of "FLEX-like measurements" to simulate the real condition and fitted the spectral features to decouple SIF and ground reflectance, with realistic assumptions of other atmospheric and environmental conditions. At this step the solar Fraunhofer lines were discarded from the retrieval algorithms because the authors argued that the Fraunhofer lines have low spectral overlap with the most intense emission in the Chl-a fluorescence spectrum. At the end it has been stated that the root-mean-square deviation (RMSD) of the retrieved SIF is 0.5 $mWm^{-2}sr^{-1}nm^{-1}$ within O_2-B band, although the oxygen line depth varies with viewing geometry and surface pressure. According to their paper, an explanation for better retrieval in O_2-B absorption band can be that it is in the red spectral region in which vegetation has a very small reflection.

In the mean time, Daumard et al. [2010] investigated passive retrieval of SIF from O_2-A and -B bands in-situ. The measurements have been held in a 38 day campaign and made use of the entire SIF spectral window ($\sim$ 687 - 760 nm). The reflectance spectrum in the 400 - 900 nm wavelength region has also been measured aiming to provide a continuous spectral signature at canopy level. Assessing the retrieved signals and comparing them with PRI values (measured simultaneously), the effect of drought could be detected for the target fields.

Joiner et al. [2011], made use of the high spectral resolution data from GOSAT to retrieve SIF from direct radiance measurements. They have used the Potassium Fraun-

hofer line near 770 nm, and stated that SIF fills a Fraunhofer line more efficiently than the O_2-A spectral band based on the findings from [Guanter et al., 2010] which stated that the O_2 bands are influenced by measurement conditions. The retrieval generally followed the expected monthly mean variation of SIF. However, comparing the retrieved values and the corresponding EVI some similarities and correlation as well as some differences were shown.

Such studies were preliminary steps to assess the relationship between the space-borne retrieved SIF and photosynthesis. Frankenberg et al. [2011b], worked on understanding the present and future carbon cycle by using solar induced chlorophyll fluorescence in order to assess its correlation to GPP. In order to investigate SIF, they collected measured radiances from the GOSAT in the 756-759 nm spectral region. They retrieved SIF by applying an iterative least-square fitting method. The so-called "zero-offset effect" (see section 3.1.1 for details) has been introduced in satellite-based SIF retrieval for the first time and an offset correction factor for it has been provided. Furthermore, they compared the results with the Max Planck Institute of Bio-geochemistry (MPI-BGC) model product, the derived GPP from Moderate Resolution Imaging Spectroradiometer (MODIS) and the NDVI, EVI and LAI indices. The SIF derived from GOSAT has been shown to correlate strongly with GPP. The derived correlation coefficient in some cases is higher than the correlation between GPP and VIs e.g. NDVI, EVI and LAI. They have finally shown that their retrieval exhibits a pronounced seasonal cycle and latitudinal dependency with GPP. In essence, this work can be considered to have a key role in SIF studies within the last years.

Soon after, Frankenberg et al. [2012] investigated the impact of atmospheric scattering effects and Chl fluorescence on satellite-based nadir viewing high resolution spectra, obtained from GOSAT and Orbiting Carbon Observatory -2 (OCO-2). They have argued that SIF cannot be retrieved exclusively from spaceborne measurements inside the O_2-A band due to the fact that the spectral signature of SIF cannot be distinguished from the impact of aerosols, ground reflection, and variations of surface pressure. More importantly, elastic scattering due to aerosols and clouds alter the shape of O_2 absorption lines. They have evaluated those assumptions by applying an empirical model for the Fraunhofer lines and a radiative transfer model (in which RRS was not included). Finally it has been shown that in the case of GOSAT and OCO-2, if the investigation is focused not on the retrieval within the O_2-A band but on the strong Fraunhofer lines around 757.5 nm and 769.5-775 nm, SIF can be retrieved with a precision of about 0.2-1% of the radiance at TOA.

Looking at the relative significance of SIF in atmospheric remote sensing, Frankenberg et al. [2012] also showed that if SIF is neglected in the retrieval algorithm of CO_2 as

a greenhouse gas, atmospheric CO_2 measurement fluxes in the O_2-A region, are systematically perturbed up to 1 ppm if SIF is assumed to consist only 1% of the retrieved radiance at TOA. Accordingly, they have proposed and shown that this bias can be eliminated if SIF is introduced as a state vector in the retrieval algorithm. Regarding fluorescence retrieval, they stated that implementing the retrieval algorithm only to the Fraunhofer lines can offer accurate and robust quantification measurements of vegetation fluorescence. It is finally suggested by the authors that measurement noise can be reduced if an extension to shorter wavelengths is applied in future instruments. Using SCIAMACHY measurements in NIR spectal region, the aim of the study done by Joiner et al. [2012] was to obtain the Chl fluorescence retrieved from lower spectral resolution. They developed an algorithm in order to simulate Vibrational Raman Scattering (VRS) and RRS as well as high temperature effects in the region of Ca II Fraunhofer line at 866 nm. Their approach was applied to SCIAMACHY data, in order to retrieve the SIF infilling on the Fraunhofer line. They have additionally compared their retrieval with retrieved SIF from GOSAT and EVI product from MODIS. Being spectrally far from both SIF emission maxima, the infilling effect of fluorescence in the CaII Fraunhofer line is found to be $\sim$ 0.1-0.2 $\mathrm{mWm^{-2}nm^{-1}sr^{-1}}$ which is reported to show similarities with the retrievals reported from laboratories. To conclude they stated that the SIF results have not only shown consistency between SCIAMACHY and GOSAT scaled fluorescence, but with the EVI temporal and spatial patterns provided by MODIS.

Fournier et al. [2012] have investigated the impact of canopy structure on Chl fluorescence properties, comparing canopy and leaf level SIF. The instrument utilized by them is SpectroFLEX, which measures fluorescence in O_2-A and O_2-B atmospheric absorption bands at canopy level. Therefore, a radiative transfer model to correct atmospheric features affecting the light was not necessary. Then, they compared the measured canopy level fluorescence with the leaf level fluorescence spectrum which was obtained simultaneously and showed that the ratio of retrieved fluorescence measured at canopy level is smaller than the fluorescence measured at leaf level by a factor of two and they could show under high light conditions, this ratio is even smaller. To understand possible sources of this change, they used FluoSAIL [Verhoef, 1984] for canopy and leaf level simulations to get a better view on the impact of canopy density and geometry on SIF. Their results confirmed that this decrease is due to the re-absorption of red fluorescence emission by Chl pigments second absorption band while the emitted far-red SIF can pass through the canopy.

On the influence of the atmospheric aerosols on fluorescence retrievals, Sanders and de Haan [2013] have investigated a simultaneous retrieval of SIF and a set of atmo-

spheric aerosol parameters, over vegetated land surfaces in the O_2-A absorption band. They have studied the precision dependence of their retrieval on the aerosol optical thickness, fluorescence emissions, surface pressure and solar and viewing zenith angles. Moreover, they have tested the dependence of the retrieval precision on the Signal to Noise Ratio (SNR) of the instrument and spectral resolution. They concluded that it is feasible to retrieve SIF simultaneously with aerosol properties.

Two satellite-based instruments SCIAMACHY and GOME-2 have been used in the study conducted by Joiner et al. [2013a] to retrieve SIF in-filling effect on the Fraunhofer lines before O_2-A absorption band. However, they expanded the application of their approach to the inside of O_2-A and water vapor absorption bands as well as the target solar Fraunhofer lines. The retrieval method applied in their study was based on Principal Component Analysis (PCA) aiming to exclude the features due to atmospheric absorption using Principal Components (PC). The model study showed that fluorescence retrieval can be obtained if the SNR is large enough for both GOME-2 and SCIAMACHY instruments. The authors also mentioned that the extra absorption bands are not necessarily providing vital information on SIF which cannot be obtained from Fraunhofer lines alone.

In order to achieve better spatial sampling, Frankenberg et al. [2014], used OCO-2 thermal vacuum test data and simulations to evaluate the potential of OCO-2 to retrieve SIF. As mentioned in the publication, the advantage of this instrument is its high spatial resolution that is 8 times better than GOME-2 (used in most studies so far).

Investigating the relationship between GPP and SIF, Guanter et al. [2014] showed that space-borne measurements of SIF provide a direct measurement of GPP of grasslands and croplands. Their results indicate that fluorescence retrieval can help to improve global models of the climate impact on the vegetation GPP.

Improving the SIF results from Joiner et al. [2013a], Joiner et al. [2013b] assessed the relationship between SIF and the length of the annual carbon uptake period. They obtained the satellite fluorescence retrievals, from GOME-2 instrument and compared them with seasonal cycles of GPP from regional flux towers. The seasonality of APAR from satellite measurements has been tested with respect to SIF variation as well. They concluded that satellite-based SIF measurements can help improving the seasonal dependence of global models of photosynthesis.

Assessing the relationship between SIF and canopy properties, the relation between Vcmax (maximum rate of carboxylation in the Calvin cycle of C3 plants) and space-borne SIF measurements of Top Of Canopy (TOC) at the ecosystem level was analyzed by Zhang et al. [2014]. They used the Soil-Canopy Observation of Photosynthesis and Energy (SCOPE) [Van der Tol et al., 2009b] balance model to derive empirical

relationships between seasonal Vcmax and SIF to be able to estimate Vcmax from space-borne retrieved SIF data. Their results were evaluated using six agricultural flux tower sites in the US. Their Vcmax values were in agreement with expectations and showed reasonable seasonal patterns. Validation of the obtained Vcmax parameterization is done by comparing the simulated GPP and LUE using their results with GPP from fixed Vcmax. GPP showed a significant improvement when they used their time-resolved Vcmax estimated from SIF retrieval.

Taking advantage of the high spectral resolution of the Fourier Transform Spectrometer (FTS[22]) on GOSAT, Köhler et al. [2015a] presented an algorithm to retrieve far-red SIF using Fraunhofer lines around 755 nm. They aimed to simplify the existing retrieval algorithms without reducing the accuracy of the retrieved SIF. Testing the sensitivity of the proposed method with different cloud thresholds, the authors concluded that their approach does not show a significant dependence on cloudiness of the scene.

Additionally, aiming to solve the remaining problems from Joiner et al. [2013a] work such as the non-linearity of the forward model, Köhler et al. [2015b] also tried to retrieve SIF from the GOME-2 and SCIAMACHY instruments. Their solution to the latter was to use a so-called backward elimination algorithm to reduce the noise effect and modify the number of fitting parameters of the retrieving method. The performance of their retrieval method has been tested on simulated data. Real data from GOME-2 and SCIAMACHY have been used in the next step to retrieve SIF based on the new retrieval method. Surprisingly, the retrieved SIF values were significantly larger than the results from Joiner et al. [2013a] and Joiner et al. [2013b]. It has been also mentioned that it is not possible to judge the quality of the retrievals in absence of a ground truth or validation source. It has been also been claimed that SIF retrievals from GOME-2 are not significantly sensitive to presence of clouds.

Verrelst et al. [2015], investigated the SIF and the key variables deriving it using the Soil-Canopy Observation of Photosynthesis and Energy balance (SCOPE) model. The SCOPE model contains leaf physiological modules to determine the fluorescence yield. They applied two model-based experiments for the different leaf physiology modules in SCOPE. For the first experiment only vegetation variables were considered and for the second one, all SCOPE variables, including micro-meteorological, aerodynamic and geometry variables were taken into account. According to them, the most important variables to determine SIF variability were leaf chlorophyll content (Cab), leaf inclination (LIDFa) and leaf area index (LAI) found to be responsible for 77.9% of

[22] A spectrometer which creates an optical path difference between the two light beams originated from the splitting the captured beam. FTS measurement uses the Fourier transform on that measured light path differences.

the SIF variability. Photosynthetic capacity, is claimed to be the source of 11.4% of overall SIF variability. However, it is more important in the first emission peak (red) that its maximal relevance is 17.9% at 676 nm, than for the second peak (NIR) where the maximum relevance is 9.6% at 740 nm. For the total SIF yield determination (the integral of the hemispherical broadband SIF flux divided by the total absorbed PAR), photosynthetic capacity plays a more important role, as they showed 35% of the variability was influenced by it. By analyzing the relative importance of all SCOPE variables, they found that micro-meteorological variables are important in driving SIF variability as well as key vegetation factors. For instance, incoming radiation (mainly in the visible range), air temperature, atmospheric vapor pressure and CO_2 concentration in the atmosphere are the most important micro-meteorological variables. Moreover, as expected and shown before, photosynthetic activity is found to be more relevant for the first SIF emission peak than for the second peak but the full broadband SIF has the most relevance to the photosynthetic activity which allows calculation of fluorescence yield in the full range.

Damm et al. [2015], assessed the relationship between the second peak of SIF (at 760 nm) and GPP, and whether it is transferable across across three different ecosystems, perennial grassland, cropland and mixed temperate forest The employed method was a multi-temporal imaging spectroscopy of the data obtained by the Airborne Prism EXperiment (APEX) and the data from eddy Covariance flux towers. The SCOPE model has been used for simulations to confirm their results from observations. Moreover, they used SCOPE to analyze factors such as physiological and structural interferences as confounding factors. They found that the relationships between SIF and GPP are dependent on the ecosystem; the correlation coefficient between GPP and the cropland ecosystem is the strongest, grasslands slightly weaker and mixed temperate forests the weakest. They also could show that asymptotic leaf level relationships between SIF and GPP are more linear at canopy level. As they mentioned, although remote sensing of SIF can be seen as a new observational approach to reduce uncertainties in estimating GPP across ecosystems, it requires compensation for factors which influence the relationship between SIF and GPP. Rossini et al. also published a study in 2015 on the relationship between red and far-red SIF with photosynthesis efficiency. Air-borne measurements have been conducted over two grass fields to retrieve SIF in both red and far-red spectral regions using O_2-B and -A absorption bands. The grass in one field was treated by a herbicide to inhibit photosynthesis. A significant increase of SIF emission in both red and far-red SIF has been detected over the treated grass with respect to the untreated field. They concluded that SIF in its both peaks is responsive to photosynthetic efficiency and is worth measuring. Daumard et al. [2015],

measured the O_2-A and -B absorption bands depth at different altitudes, from 324 to 3123 m, for different vegetation density such as bare soil and wheat fields. Their results imply that in O_2-B band, the depth variation has the same order of magnitude as the expected SIF impact. However, within this wavelength region, the variation in the O_2-A absorption band is much stronger than the variation of SIF. They used the MODTRAN 4 to assess the sensitivity of the absorption band depth to several atmospheric parameters. Among them, temperature, air pressure, and aerosols were found to be the most critical parameters in their study. Correcting the measurements for atmospheric effects, a significant reduction of band depth variation with altitude had been observed. The MODTRAN feasibility to simulate oxygen band depth variations at spectral resolution of around 0.5-1 nm was shown. The retrieval of solar-induced plant fluorescence within the red spectral region (known as red SIF) has been demonstrated for the first time from land and ocean by Wolanin et al. [2015] who presented a SIF retrieval approach which shares some similarities with this work. The instruments utilized in this study were SCIAMACHY and GOME-2 and the retrieved values have been compared to MODIS EVI with good agreement. Joiner et al. [2016], extended the implementation of their PCA based from far-red SIF retrievals to red spectral region utilizing GOME-2 and SCIAMACHY measurements to retrieve fluorescence from O_2-B spectral region. To compensate for the O_2 absorption effect, the O_2-γ absorption band, which is not affected by SIF was also taken into account. The retrieved SIF values within the red spectral range have been compared to simulated data and showed good agreement. The results were corrected with respect to the so-called zero-offset effect. Additionally, according to their study, the sensitivity of red SIF to water stress is higher than far-red SIF. Rossini et al. [2016] conducted several field measurements of red and far-red SIF signals for different canopy compositions. Generally speaking, the far-red SIF shows higher values than red SIF due to re-absorption discussed before. Moreover, crops performed higher SIF emission than broad leaf trees and the lowest measurements were over needle leaf species. Although the SIF emission depends on the photosynthetic capacity , the authors stated that leaf and canopy characteristics such as LAI and chlorophyll content of the leaves have a significant influence on the SIF emission. van der Tol et al. [2016] confirmed that the emitted fluorescence (at 760 nm) is strongly dependent on biochemical and structural canopy variables. Therefore, measuring fluorescence could make it feasible to predict physiological variations of the plants without having a direct measure of the leaf inclination or Chl concentration of the leaves. A study by Zhang et al. [2016a] confirmed the previous findings on the linear relationship between GPP and SIF utilizing SIF measurements and simulated GPP values. However, not all modeled GPP results follow the spatial pattern of satellite

based SIF values (from GOME-2). Later, a model study conducted by Zhang et al. [2016b] focused on the relationship between SIF and GPP. The SCOPE model has been utilized to simulate both factors at leaf and canopy levels considering the temporal variations of the canopy as well as the measurement conditions. Interestingly, the relationship between leaf-level GPP and SIF is reported to be highly non-linear, but more linear at the canopy level. The relationship between SIF and GPP is reported to be driven by APAR, especially at the seasonal scale depending on the photosynthetic efficiency. The authors confirmed these results based on in-situ measurements. On the linear relationship between SIF and GPP, Goulas et al. [2017] conducted a study on wheat canopy. The in-situ measurement of SIF in both O_2-A and -B absorption bands were taken from wheat plants and normalized with respect to PAR in order to obtain fluorescence yields for both red and far-red spectral regions. The fluorescence yields were compared with GPP measured by eddy covarience techniques. It has been found that far-red SIF has stronger correlation to GPP than the far-red SIF. This correlation is strongest during growth periods and highly variable. For steady state canopy, SIF was not significantly more informative than PAR. Therefore, far-red SIF is found to be more helpful to predict GPP for growing canopy.

2.5 Goals of this work

The aim of this thesis is to retrieve solar-induced terrestrial plant fluorescence based on radiance measurements at TOA, provided by the hyper-spectral satellite-based instrument SCIAMACHY. In 2013, at the beginning of this study, there was a clear need for an independent straightforward SIF retrieval method specifically for instruments with moderate spectral resolution (e.g. SCIAMACHY) and within the wavelength region of strong fluorescence emission. The results obtained by Joiner et al. [2012] were the only SCIAMACHY-based study although due to the spectral location of the chosen Fraunhofer line for the retrieval (Ca II) were not extrapolated to spectral intervals closer to the emission maxima. The results from Guanter et al. [2007, 2010], Joiner et al. [2011], Frankenberg et al. [2011b, 2012] helped developing a generic retrieval method by demonstrating potential possibilities and obstacles.

In general, the objectives of this work are:

- To develop a new, independent and generic approach, applicable to all spectrometers measuring in the fluorescence emission wavelength range.
- To conduct a thorough model-based sensitivity analysis on the proposed method to assess the potential sources of error as well as modify the proposed method

with respect to the environmental and measurement characteristics.

- To compensate for a ”zero-offset” signal (see section 3.1.1) applicable for data from all modern spectrometers fulfilling a specific measurement accuracy and resolution.
- To analyze the seasonal trends of SIF and compare the retrieval to already existing retrievals in absence of a suitable validation source.
- To assess the relationship between the measured SIF and bio-geochemical properties of the canopy e.g. GPP, APAR and LAI as a vegetation index representing the vegetation density.
- To characterize SIF over its both spectral peaks, preferably achieving a full spectrum SIF retrieval

Part II

Model, Data &, Sensitivity

Chapter 3

Retrieval approach and instruments

Sun-induced plant fluorescence is about two orders of magnitude smaller than the solar radiance, reflected from the plants (section 2.1.4). At TOA, the upwelling radiance has been already modified by (i) absorption by gases, the Earth's surface, aerosols and clouds, (ii) scattering by gas molecules and particles (i.e Rayleigh, Mie and Raman scattering). By these means, radiance at TOA carries the spectral imprint of these various features. In comparison to these processes, fluorescence plays a rather small role, requiring high accuracy of the utilized retrieval approach. Additionally, instrumental artifacts and signal non-linearity in space-borne detectors cause spectral distortion of the measurement. This necessitates a retrieval algorithm, based on accurate modeling of the radiative transfer, considering the measurement limitations.

3.1 Methodology

As explained in chapter 2, SIF is superimposed on top of the diffused radiation at the canopy layer, causing a relative change in the upwelling radiation at TOA.

Based on the evident advantage of hyperspectral FLD-based methods over multi-spectral approaches, especially for satellite-based measurements (see section 2.3), the retrieval algorithm proposed in this thesis aims to detect the fluorescence signal based on hyper-spectral space-borne measurements of the backscattered solar radiation. The proposed method is also capable of providing estimations of SIF at the top of canopy (TOC) layer.

According to the Beer Lambert's law (see section 2.2) the Logarithm of Sun-normalized Radiance (LSR) governs the relative variation of radiance with respect to the incident radiance which was also regarded to as the Optical Depth (OD), $\tau(\lambda)$, before. Therefore, for a measured radiance at TOA at the wavelength λ, one can write:

$$S^m(\lambda) = \ln \frac{I_m(\lambda)}{I_0^m(\lambda)}\,, \tag{3.1}$$

in which $I_m(\lambda)$ and $I_0^m(\lambda)$ are the measured radiance [photons s^{-1} cm^{-2} nm^{-1} sr^{-1}] at TOA and extra-terrestrial solar irradiance [photons s^{-1} cm^{-2} nm^{-1}], respectively. I_0^m and I_m are dependent on the observation and illumination geometry, geographical coordinates of an instrument footprint and measurement time. However, these dependencies are not noted here for the sake of clarity.

As mentioned before, the problem being addressed here is to retrieve SIF as a relatively small additive signal of the upwelling radiance at TOA, while it is influenced by the atmospheric and measurement conditions and disentangle it from the comparable spectral features not caused by SIF [Frankenberg et al., 2011b].

The main idea is that the spectral signature of SIF can be obtained solving an inverse problem using $S^m(\lambda)$, assuming that it alters the spectral shape of I_m by filling in the absorption bands (see section 2.3 for details). The sun-normalized radiance is typically used for the solution of numerous inverse problems based on satellite-borne data because ratioing the measured radiance by the solar irradiance leads to significant decrease of the Fraunhofer line amplitude and shows the relative fraction of the I_m and I_0^m. Additionally, using the natural logarithm simplifies the forward model to a linear relationship between optical depths. This would allow the separation of the broadband spectral structures (caused by the surface reflection and scattering processes in the atmosphere) from high-oscillating remaining Fraunhofer structures (caused by trans-spectral processes or instrumental effects). Using natural logarithm also helps reducing potential calibration errors.

3.1.1 Forward model

To solve an inverse problem, the forward model of the measured quantities has to be developed. In this study, a comprehensive radiative transfer model; SCIATRAN (see section 3.1.4) has been used to simulate the TOA radiances which are necessary to formulate the forward problem. The corresponding LSR to an upwelling radiance at TOA can be written as follows:

$$S(\lambda) = \ln \frac{I^+(\lambda) + \varepsilon_a(\lambda)}{I_0(\lambda)}\,, \tag{3.2}$$

where $I^+(\lambda)$ is the modeled upwelling radiance at TOA influenced by SIF and $I_0(\lambda)$ is the extra-terrestrial solar irradiance. The term ε_a is an additive signal not

induced by SIF, but having a magnitude comparable to SIF which can be detected by SIF retrieval algorithms over regions where no SIF is expected (e.g. barren lands and snow).

The only known possible sources which can cause an infilling effect on the solar Fraunhofer lines other than vegetation fluorescence is Raman scattering (section 2.2.3) [Joiner et al., 2012, Vasilkov et al., 2013, Wolanin et al., 2015], thermal emission from high temperature emitters such as forest fires and volcanic eruptions ($> 650K$) [Joiner et al., 2012, and confirmed by numerical simulations in this study] and fluorescence emission from other sources than vegetation e.g. minerals in soil and rocks. According to Abrams et al. [1994], detector signal non-linearity causes systematic errors in the measurement, referred to as zero-level offset. As Frankenberg et al. stated in 2011a, the so-called zero-level offset effect and stray-light are instrumental artifacts which are also potential sources of in-filling of the Fraunhofer lines. For the sake of simplicity, in the framework of this study, the term **zero-offset effect** is chosen to refer to the in-filling impact of the ε_a signal, independent on its source as long as it is not SIF. The so-called zero-offset effect intervenes with any method directly retrieving the infilling of the absorption lines and distorts the outcome if not being taken into account (see section 3.1.2). It should be noted that since only emissions from extremely high temperature sources such as forest fires can contribute to the infilling effect within the spectral window of SIF emission. However, the spatial size of such heat sources is not large enough (and accordingly) not likely to cover the large footprints of instruments utilized in this work (see section 3.1.4).

The TOA radiance influenced by SIF can be represented by:

$$I^{+}(\lambda) = I^{-}(\lambda) + \mathcal{F}_t(\lambda)\,, \tag{3.3}$$

assuming the upwelling radiance at TOA from a region free of vegetation (and therefore free of SIF) to be $I^{-}(\lambda)$ and $\mathcal{F}_t(\lambda)$ to be the SIF spectrum at TOA.

The challenge of retrieving SIF at TOA is its small magnitude compared to the radiance. Therefore, the FLD-based methods discussed in section 2.3 are designed in order to retrieve SIF signal from its infilling effect. Accordingly, one can define the spectral influence of SIF on the radiance at TOA as the Fluorescence Reference (FR) spectrum, F, being the natural logarithm of the ratio between radiances in presence and absence of SIF (also referred to as the fluorescence OD in this work):

$$F(\lambda) = \ln \frac{I^{+}(\lambda)}{I^{-}(\lambda)}\,. \tag{3.4}$$

Substituting Eq. (3.3) into Eq. (3.4) and accounting for that $\mathcal{F}_t$ is much smaller than I^- and that the Taylor expansion of the natural logarithm can be restricted to linear term (with respect to $\mathcal{F}_t$), one can rewrite the Eq. 3.4 as:

$$F(\lambda) = \ln\left[1 + \frac{\mathcal{F}_t(\lambda)}{I^-(\lambda)}\right] \approx \frac{\mathcal{F}_t(\lambda)}{I^-(\lambda)} \,. \tag{3.5}$$

To model the radiance at the TOA, SCIATRAN has been used to solve the RTE (Eq. 2.21). The outcome of the model are $I^+(\tau, \Omega, \lambda)$ and $I^-(\tau, \Omega, \lambda)$, being the radiances at TOA in presence and absence[1] of SIF emission respectively. They are regarded to as $I^+(\lambda)$ and $I^-(\lambda)$ hereafter for the sake of simplicity.

From Eq. 3.5 it can be seen that the FR spectrum, F, is directly proportional to the fluorescence spectrum at TOA and therefore, is a measure of SIF magnitude. Thus, the following assumptions are the basis of the inverse problem:

- The variation of the fluorescence spectrum at TOA, $\mathcal{F}_t(\lambda)$, can be quantified by scaling the FR spectrum.

- The spectral shape of unknown fluorescence spectrum at TOA, $\mathcal{F}'_t(\lambda)$, resembles the shape of an *a priori* one. Therefore, it can be estimated scaling the *a priori* spectrum, i.e.,

$$\mathcal{F}'_t(\lambda) = f\,\mathcal{F}_t(\lambda) \,, \tag{3.6}$$

  where $\mathcal{F}_t(\lambda)$ is a priori fluorescence spectrum, f is the scaling factor;

- The same scaling factor f is used to estimate an unknown fluorescence spectrum at top of canopy layer scaling the *a priori* one, i.e.,

$$\mathcal{F}'_b(\lambda) = f\,\mathcal{F}_b(\lambda) \,, \tag{3.7}$$

  where $\mathcal{F}_b(\lambda)$ is the *a priori* fluorescence spectrum at top of canopy layer (see section 2.2.4).

- The additive component $\varepsilon_a(\lambda)$ will be approximated as spectrally constant (in the considered wavelength window). The error introduced to the retrieval method due to this assumption is discussed in the section 4.3.1 and is not significant within such narrow spectral range.

[1] To obtain the radiance at the TOA in absence of SIF emission $\mathcal{F}_b$ is set to zero in Eq. 2.24.

Multiplying the nominator and denominator in Eq. 3.2 by $I^-(\lambda)$ leads to:

$$S(\lambda) = \ln \frac{I^-(\lambda)}{I_0(\lambda)} + \ln \frac{I^+(\lambda) + \varepsilon_a(\lambda)}{I^-(\lambda)} \ . \tag{3.8}$$

Considering the additive component ε_a to be significantly smaller than $I^+(\lambda)$, a linear approximation of the forward model would be:

$$S(\lambda) = \ln \frac{I^-(\lambda)}{I_0(\lambda)} + \ln \frac{I^+(\lambda)}{I^-(\lambda)} + \frac{\varepsilon_a(\lambda)}{I^+(\lambda)} \ . \tag{3.9}$$

The second term in this expression can be replaced by F.

Summing up the forward model based on Eq. 3.9 and the above mentioned assumptions, for a simulated radiance at TOA which is influenced by **unknown** fluorescence emission can be adapted and formulated as follows:

$$S(\lambda) = \ln \frac{I^-(\lambda)}{I_0(\lambda)} + f\,F(\lambda) + \frac{\varepsilon_a}{I^+(\lambda)} \ . \tag{3.10}$$

The first term on the right hand side of Eq. 3.10 does not contain any information on SIF emission but represents the effect of atmosphere and surface e.g. atmospheric gaseous absorption, aerosol scattering and absorption, as well as surface reflection.

As explained in section 2.2.3, atmospheric scattering has a broadband spectral shape inversely proportional to several exponents of wavelength (λ). However, gaseous absorption does not exhibit the same behavior and creates fluctuating spectral signatures based on the probabilities of rotational, vibrational and electronic transitions of the gas molecules. More importantly, it highly depends on the concentration of the absorber in the light path (see section 2.2.1) causing variation in the depth of the absorption bands.

Therefore, by choosing a rather narrow wavelength range where practically no gaseous absorption can be observed, the effect of gaseous absorption of unknown strength can be mitigated. Moreover, the spectral broadband effects of aerosols, molecular scattering and surface reflectance do not have drastic variations over narrow spectral intervals. Under this assumption the first term in Eq. (3.10), owing to its spectral smoothness, can be approximated by a low order polynomial. Coefficients of the polynomial are fit parameters in the same manner as e.g., for ε_a. Therefore, for different absorption and scattering by aerosols, different polynomial coefficients will be obtained in the fitting process:

$$\ln \frac{I^-(\lambda)}{I_0(\lambda)} = \sum_{i=1}^{N} a_i \lambda^i = P(\lambda) \ , \tag{3.11}$$

where a_i are polynomial coefficients and N is the degree of polynomial. Using systematic computations running SCIATRAN, the degree of the polynomials has been chosen to be three ($N = 3$) to approximate all broadband features in the selected spectral window with sufficient accuracy. Please note that, although $N = 3$ is used for all polynomials, coefficients a_i vary in different minimization problems. Therefore, the polynomials being introduced hereafter are distinguished by their subscripts, namely m, c, s, a and ε. In particular, the suggested fluorescence retrieval algorithm utilizes measurements in the spectral window 748.5 - 753.0 nm (see section 4.2 for details on selecting the retrieval spectral window). Simulated ODs for $I^-\left(:\ln\frac{I^-(\lambda)}{I_0(\lambda)}\right)$ and $I^+\left(:\ln\frac{I^+(\lambda)}{I_0(\lambda)}\right)$ are shown in Fig. 3.2 in which the spectral shape of the LSR in absence (LSR$^-$) and presence (LSR$^+$) of the SIF emission can be compared. Moreover, the analysis of residuals after fitting of measured LSR does not demonstrate any remaining broadband spectral components. Thus, the forward model (Eq. 3.10) can be reformulated as following:

$$S(\lambda) = f\,F(\lambda) + \frac{\varepsilon_a}{I^+(\lambda)} + P_m(\lambda)\ , \tag{3.12}$$

in which $P_m(\lambda)$ represents the third order polynomial replacing the term $\ln\frac{I^-(\lambda)}{I_0(\lambda)}$. Figure 3.1 demonstrates the difference between modeled $I^+(\lambda)$ and $I^-(\lambda)$ within the selected wavelength window as well as F from Eq. 3.4. The relative ratio of the radiances in presence and absence of SIF shows the spectral structure due to the in-filling effect. As it can be seen from the Fig. 3.2 the LSR$^+$ has the same spectral structure. Simulations showed that, for simulated data when ε_a does not play a role, LSR$^+$ can be reconstructed summing FR and LSR$^-$. This confirms the expression of the forward model from Eq. 3.12.

3.1.2 Inverse problem

The target parameters of the forward model given by Eq. 3.12, i.e., f and ε_a can be obtained solving the following minimization problem:

$$\| S^m(\lambda) - S(\lambda) \|^2 = \left\| S^m(\lambda) - \frac{\varepsilon_a}{I^+(\lambda)} - f\,F(\lambda) - P_m(\lambda) \right\|^2 \rightarrow min\ , \tag{3.13}$$

where $S'(\lambda)$ is substituted according to Eq. 3.12 and $S^m(\lambda)$ has been defined in Eq. 3.1. Assuming the term $S^m(\lambda)$ to be the measured OD of the atmosphere for this spectral range, $S^m(\lambda) - P_m(\lambda)$ is known as the Differential Optical Depth (DOD) which represents the spectral shape of the measured LSR after removal of the broadband features and contains the net infilling structure. For the sake of clarity, the fit results

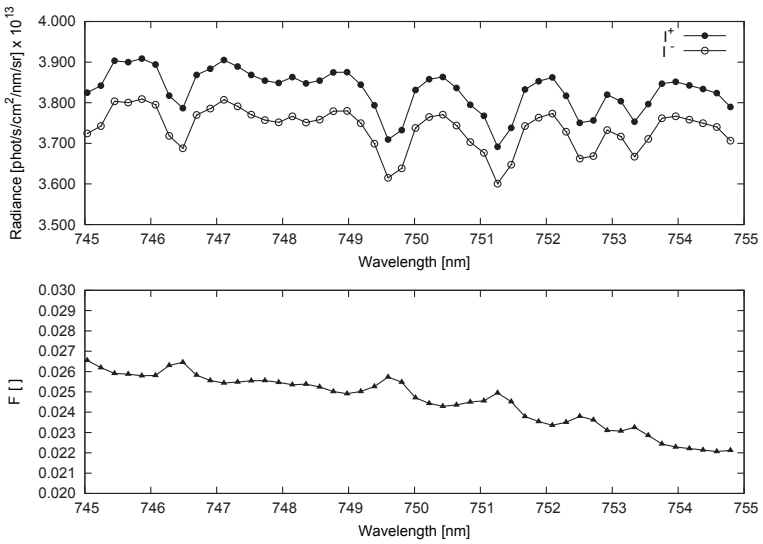

Figure 3.1: Top: The simulated radiances at the TOA for the chosen wavelength range in presence and absence of the SIF signal, causing a vertical shift in I^+ with respect to the I^-. Bottom: The FR spectrum, obtained from the radiances shown above.

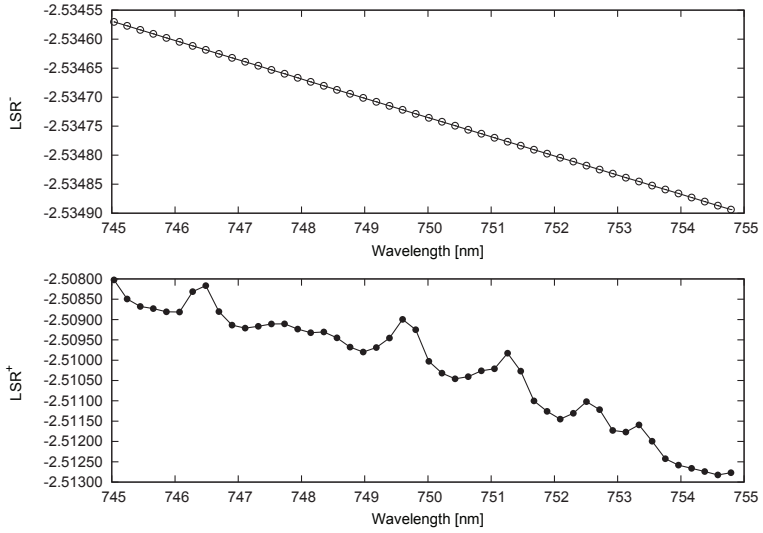

Figure 3.2: The modeled optical depths (LSRs) at the TOA in absence (top) and presence (bottom) of the SIF emission. In absence of the SIF emission and within a wavelength window in which no absorption occurs, a polynomial can represent the LSR^-. However, adding fluorescence emission to the spectrum causes fluctuations in h LSR^+.

within the framework of this thesis are shown after removing the polynomial as DOD. Unfortunately, the minimization of the quadratic form given by Eq. 3.13 does not allow the estimation of parameters f and ε_a simultaneously. Another equation is necessary to estimate both of these unknowns independently. Considering Eq. 3.5, it can be seen that $F(\lambda) \sim 1/I^-(\lambda) \sim 1/I^+(\lambda) \sim 1/I_m(\lambda)$. Therefore, one can safely assume that $F(\lambda)$ and $1/I_m(\lambda)$ are strongly correlated. To address this, a linear relationship between $F(\lambda)$ and $1/I_m(\lambda)$ is defined introducing C_a as a fit parameter:

$$\left\| \frac{1}{I_m(\lambda)} - C_a F(\lambda) - P_c(\lambda) \right\|^2 \rightarrow min \; . \tag{3.14}$$

Detailed discussion on the necessity of introducing C_a can be found in section 3.1.3. It has been confirmed from numerical simulations (see section 5.1) that $1/I_m(\lambda) \approx C_a\, F(\lambda) + P_c(\lambda)$, which leads to the following relationship:

$$F(\lambda) \approx \frac{1}{I_m(\lambda)\, C_a} - \frac{1}{C_a} P_c(\lambda) \, . \tag{3.15}$$

The term $1/C_a\, P_c(\lambda)$ is clearly a polynomial and the quadratic form given by Eq. (3.13) can be rewritten as:

$$\left\| S^m(\lambda) - \frac{\varepsilon}{I_m(\lambda)} - P_\varepsilon(\lambda) \right\|^2 \rightarrow min \; , \tag{3.16}$$

in which the parameter ε is to be retrieved as a total infilling of the Fraunhofer lines due to SIF and the zero-offset effect:

$$\varepsilon = \varepsilon_a + \frac{f}{C_a} = \varepsilon_a + \varepsilon_f \; . \tag{3.17}$$

It follows that the parameter ε represents the linear combination of additive component ε_a and fluorescence emission $\varepsilon_f = f/C_a$.

If no SIF emission is influencing the measured radiance, f equals zero (see Eq. 3.12) and the additive component ε_a can be obtained solving the minimization problem (3.16) for measurements over ground pixels free of SIF, since ε equals ε_a for such a case (Eq. 3.17).

To illustrate the influence of ε_a on the retrievals when it is not subtracted from the overall infilling effect a sample global map of the retrieved ε values is presented in Fig. 3.3 and discussed by Khosravi [2012]. One can clearly see the barren regions (e.g. Sahara) demonstrating ε values comparable to the highly vegetated regions (e.g. Europe

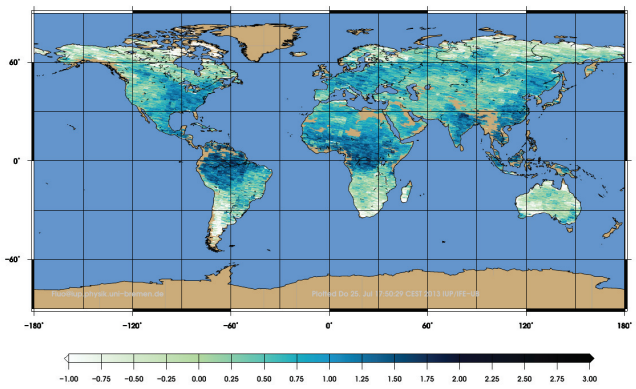

Figure 3.3: A global map of retrieved ε values (within the far-red spectral region before the O_2-A absorption band) from SCIAMACHY instruments measurements during summer 2008 (from 01.06 to 31.08). This map contains only raw data without any post-processing.

and North American agricultural regions). Comparing the map from Fig. 3.3 with the ground reflectance databases for this spectral interval one can infer that the retrieved ε values increase with radiance.

Fig. 3.4 provides an example of the retrieved ε versus the average radiance values for one day of measurement provided by SCIAMACHY (see Section 4.1 for details). The measurements are obtained from specific regions free of vegetation to estimate ε_a and vegetated regions for the sake of comparison. The process in which the regions of parameterization are chosen is described in section 4.1. Measurement-based studies showed that the ε_a values, obtained for variety of observations at TOA, are clearly dependent on the spectrally averaged radiance for any measurement ($\bar{I}_m$) and can be approximated as $\hat{\varepsilon}_a$:

$$\hat{\varepsilon}_a(\bar{I}_m) = a\,\bar{I}_m^2 + b\,\bar{I}_m + c\,, \tag{3.18}$$

where a, b, and c are coefficients of this parabolic approximation, $\bar{I}_m$ is the measured radiance averaged over spectral window under consideration, i.e.,

$$\bar{I}_m = \frac{1}{\lambda_2 - \lambda_1} \int_{\lambda_1}^{\lambda_2} I_m(\lambda)\, d\lambda\,. \tag{3.19}$$

λ_1 and λ_2 are the minimal and maximal wavelength of the chosen spectral window. Accordingly, $\hat{\varepsilon}_a(\bar{I}_m)$ is the fitted polynomial to the ε_a values at each radiance $\bar{I}_m$.

Having obtained the approximation of $\hat{\varepsilon}_a$, the estimation of the scaling factor f is performed solving the minimization problem (Eq. 3.16) for the measurements over

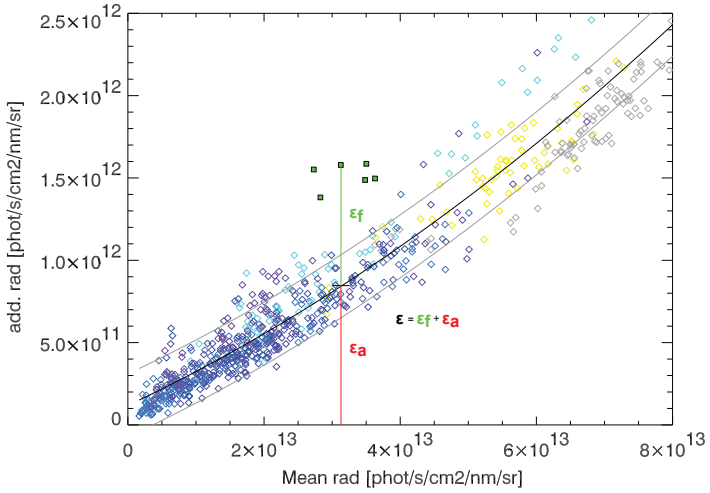

Figure 3.4: The additive radiance ε as a function of the mean radiance ($\bar{I}_m$) for one day of data: green symbols, in presence of vegetation; blue, over open ocean; gray, over permanent land ice; yellow, over desert; black solid line is the fitted curve; gray solid lines are ($\pm\boldsymbol{\sigma}$) standard deviation curves. All retrieved ε_a in absence of vegetation might be affected by cloudiness.

ground pixels expected to be influenced by SIF. The retrieved parameter ε allows the determination of the scaling factor f. Indeed, employing Eq. (3.17) f is obtained:

$$f = C_a \left[\varepsilon - \hat{\varepsilon}_a(\bar{I}_m)\right] \ , \tag{3.20}$$

where the additive component $\hat{\varepsilon}_a$ is calculated according to Eq. (3.18) using the averaged measured radiance $\bar{I}_m(\lambda)$.

In essence, as the flowchart in Fig. 3.5 shows, the retrieval approach adapted in this study consists of the following steps:

1. Retrieval of additive component ε_a solving the minimization problem given by Eq. 3.16 for measurements over ground pixels without impact of SIF.

2. Quantification of $\hat{\varepsilon}_a$, i.e., determination of parabolic approximation coefficients a, b, and c in Eq. 3.18. Since also instrumental effects can contribute to ε_a which can vary faster than natural ones, coefficients of parabolic approximation were created on a daily basis. The time span of one day provides sufficient statistics but is short enough to represent day-to-day variation of the additive component.

3. Retrieval of the component ε, by solving the minimization problem given by Eq. (3.16) for measurements over ground pixels influenced by SIF.

4. Determination of C_a solving the minimization problem given by Eq. (3.14).

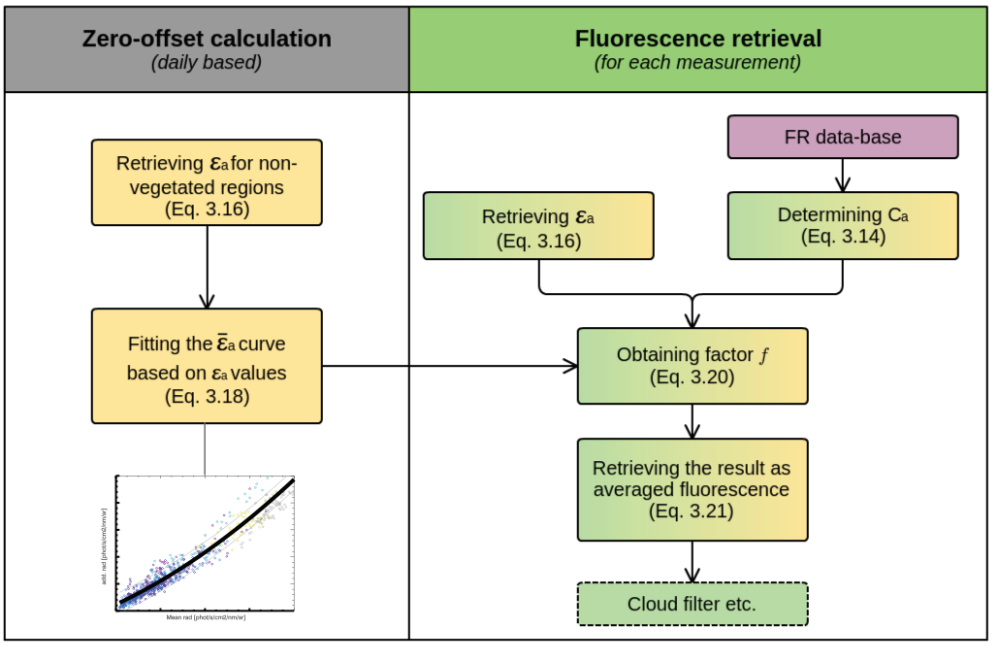

Figure 3.5: The developed method including approximating the so-called zero-offset effect and its utilization to retrieve fluorescence. Each box represent one step in the retrieval progress. Parametrization of zero-offset is shown in boxes color-coded in beige implying that measurements over non-vegetated regions are used for those processes. Similarly, green-beige boxes represent all measurements over vegetated and non-vegetated ground pixels. The final retrieval results are filtered with respect to clouds and NDVI illustrated in green. FR data-base is from model-based simulations and is shown in purple.

5. Calculation of scaling factor f according to Eq. (3.20) using estimated values of ε, ε_a, and C_a.

6. The retrieval results are presented in the form of *scaled spectrally averaged fluorescence emission at the top of canopy layer* ($\bar{\mathcal{F}}'_b$):

$$\bar{\mathcal{F}}'_b = f \frac{1}{\lambda_2 - \lambda_1} \int_{\lambda_1}^{\lambda_2} \mathcal{F}_b(\lambda)\, d\lambda = f \bar{\mathcal{F}}_b \,. \tag{3.21}$$

It is worth to notice that the auxiliary variables C_a and ε could be excluded from the retrieval process: Theoretically, after correcting for ε_a, the Eq. 3.12 could be solved directly with respect to the parameter f without considering C_a and ε. Although this would simplify the retrieval algorithm, the results of numerical experiments, presented in the following section demonstrate that subtraction of the obtained $\hat{\varepsilon}_a$ from the measured radiance leads to numerical instability of the fitting process.

3.1.3 Necessity of C_a for the retrieval

On a theoretical level, the variable C_a is not necessary for the retrieval process. In fact, the measurement over non-vegetated pixels can be used to estimate $\hat{\varepsilon}_a$ according to Eq. 3.18 and the estimated value could then simply be subtracted from the measured signal for vegetated pixels. Using this corrected LSR instead of $S(\lambda)$ on the left-hand side of Eq. 3.12, one can see that the right-hand side does not contain $\varepsilon_a/I^+(\lambda)$ and therefore, Eq. 3.12 can be rewritten in the form of the following minimization and the scaling factor f can be obtained without implementation of C_a and ε as in Eq. 3.20:

$$\left\| \ln \frac{I_m(\lambda) - \hat{\varepsilon}_a(\lambda)}{I_0(\lambda)} - f\,F(\lambda) - P_a(\lambda) \right\|^2 \rightarrow min\ , \tag{3.22}$$

in which $P_a(\lambda)$ is the third order polynomial compensating for broadband features as discussed in section 3.1.1.

To illustrate the total infilling of I_m from both the additive and SIF signals, a sample measurement from a vegetated region free of clouds have been used in the minimization Eq. 3.16 and plotted in Fig. 3.6. To examine the effect of the ε_a and SIF on f, the following minimization has also been applied on the same measurement sample [Khosravi, 2012]:

$$\left\| \ln \frac{I_m(\lambda)}{I_0(\lambda)} - f\,F(\lambda) - P_s(\lambda) \right\|^2 \rightarrow min\ , \tag{3.23}$$

and the fit result is plotted in Fig. 3.6 as well. $P_s(\lambda)$ is the third order polynomial (section 3.1.1). It can clearly be seen from the Fig. 3.6 that Eq. 3.16 and 3.23 are closely related and their residuals show similarities.

To compare, the fit results from Eq. 3.22 are presented in Fig. 3.7. The fit is clearly affected by noise and is not as instructive anymore. Therefore, it has been assumed that there is a linear relationship between the $F(\lambda)$ and $1/I_m$ which can be obtained from Eq. 3.14.

Comparing the upper plots of Fig. 3.6 and Fig. 3.7 it can be seen that after subtraction of the additive component, $\hat{\varepsilon}_a$, the new LSR has a smaller amplitude than the LSR before the correction and the impact of the random noise on the minimization increases significantly. To avoid this problem, the solution provided by Eq. 3.14 has been developed. The fit result of the latter (for the same measurement as before) are presented in Fig. 3.8. The obtained fit factor C_a connects f and ε_f as shown in Eq. 3.20.

To summarize, numerical studies showed that the subtraction of the additive component ε_a decreases the remaining spectral structure of Fraunhofer lines and increases

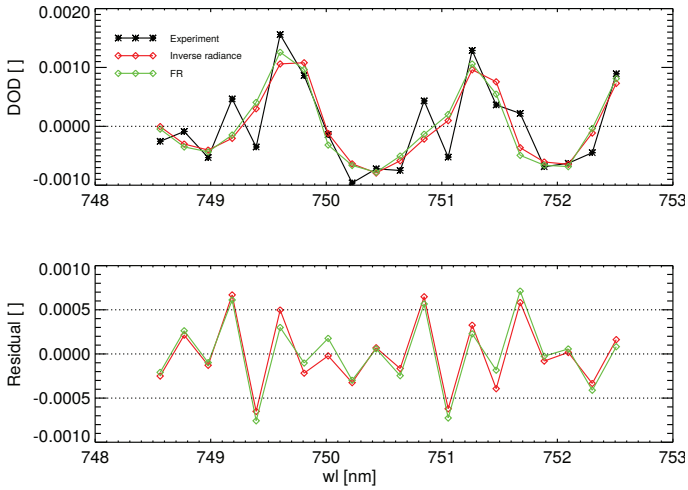

Figure 3.6: A LSR based on SCIAMACHY measurements (black) together with the fitted $1/I_m$ according to the Eq. 3.16 (red) and the fitted FR spectrum according to the Eq. 3.23 (green). The residuals from both fits show similarities (below) [Rozanov, 2014]

.

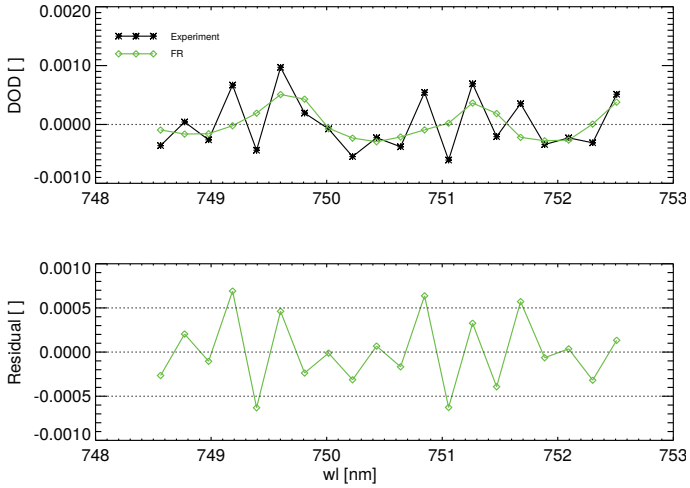

Figure 3.7: The fit results according to the Eq. 3.22. The first term of the minimization is significantly smaller than the measured DOD before subtraction of $\hat{\varepsilon}_a$ (LSR) and therefore the fit shows more sensitivity to the noise. [Rozanov, 2014]

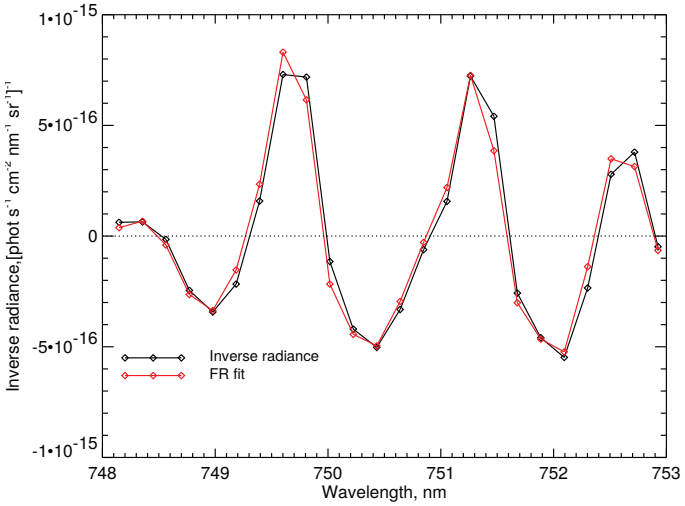

Figure 3.8: The relationship between the inversed radiance $1/I_m$ and the FR spectrum according to the Eq. 3.14. [Rozanov, 2014]

the impact of random errors, which is especially important in the case of the weak fluorescence signal. Taking into account this finding, in this investigation, the retrieval algorithm has been modified to include the auxiliary variables C_a and ε to improve the retrieval as has been presented in section 3.1.2.

The radiative transfer model behind the development of the retrieval method, numerical simulations and parameterization of the fit parameters is SCIATRAN, version 3 [Rozanov et al., 2014]. Additionally, the Fluorescence Reference spectra (FR), which is necessary in order to solve the minimization (Eq. 3.14) for each measurement case is calculated using this radiative transfer model. The radiances produced by SCIATRAN have been implemented in Eq. 3.4 to produce FR spectra in form of data-base.

3.1.4 SCIATRAN

SCIATRAN is a comprehensive software package capable of simulating the radiative transfer process in the terrestrial atmosphere and ocean in the broad spectral range of 175.44 nm in UV to 40 μm in the infra-red range. SCIATRAN as a Radiative Transfer Model (RTM[2]) is able to simulate multiple scattering processes, thermal emission and polarization as well as radiative coupling of ocean and atmosphere. Radiative transmission, scattering, reflection, and emission processes can be modeled by SCIATRAN based on either a plane-parallel or a spherical atmosphere. The vector mode simulation is to describe the polarization of the electromagnetic radiation in the

[2]Any reference to RTM in this dissertation is referring to SCIATRAN unless otherwise stated.

atmosphere. The observer position can be set to the space or TOA, or an altitude within the atmosphere, on the oceanic surface, on the ground and under water. The geometry of the observation can also be set to various modes such as nadir, limb, occultation, zenith-sky, etc.

Some of the important atmospheric processes for which SCIATRAN is accounting are Rayleigh scattering, scattering by aerosols and cloud particles and absorption by gaseous components. Some of the other features provided by SCIATRAN to simulate radiative transfer are bidirectional surface reflection, coupling the reflection profile of different surface classifications (e.g. vegetated and bare soil), accounting for latitude and seasonal variation, rotational Raman scattering in air and vibrational Raman scattering in (liquid) water, calculation of gaseous optical depths and weighting functions.

Within the framework of this thesis SCIATRAN has been ignoring thermal emission (see section 3.1.1) as well as polarization but accounting for multiple scattering processes and Lambertian surface reflection for the following aspects of the work:

- developing the retrieval method,
- assessing the sensitivity of the approach to the uncertainties in atmospheric and measurement parameters and
- calculating the FR spectrum for a wide range of measurement scenarios.

3.1.5 Fluorescence Reference Spectra

Terrestrial plant fluorescence has been implemented into SCIATRAN version 3 by adding fluorescence emission as a source term in the lower boundary condition of the radiative transfer equation (see section 2.2).
The fluorescence emission spectrum at the top of canopy layer, $\mathcal{F}_b(\lambda)$, has been selected through FluorMOD (Development of a Vegetation Fluorescence Canopy Model) project data documented for example in Miller et al. [2003, 2005] and Zarco-Tejada et al. [2006]. **FluorMOD** project (started in 2002) aims to model SIF for unstressed vegetation. A leaf and a canopy vegetation model have been developed based on experimental studies and field measurements [Miller et al., 2003].

The spectral window to calculate FR spectra (as is needed for the retrieval) has been selected according to the requirements formulated below (For details see section 4.2):

- A sufficiently strong fluorescence signal contribution is needed for accurate retrievals.

- The considered wavelength range is free of surface or telluric absorption features.
- The filling-in of Fraunhofer lines caused by the RRS and VRS should be as small as possible.

One can derive estimates of the Gross Primary Product (GPP) and the plant physiological state from the retrieved SIF. The latter was shown by Daumard et al. [2010] for a wavelength range nearby the O_2-A absorption band. The relationship between GPP and SIF was given by e.g. Frankenberg et al. [2011b], Guanter et al. [2013].

The selected spectral wavelength window between $\lambda_1 = 748.5\,\text{nm}$ and $\lambda_2 = 753.0\,\text{nm}$ is free of gaseous absorption and located near to the PSI peak of fluorescence emission. Although the selected window is $\sim 5\,\text{nm}$ wide, it contains two pronounced Fraunhofer lines (see Fig. 3.1) which are strong enough to be the main source of information about the strength of fluorescence emission in the considered retrieval algorithm.
Moreover, numerical experiments show that RRS and VRS do not play an important role in this spectral range as discussed in section 4.3.4 (and Joiner et al. [2013a], Vasilkov et al. [2013]) i.e. maximum RRS effect does not exceed $\sim 3\%$ of the total in-filling of the considered Fraunhofer lines.

3.2 Instruments

Based on the model studies (described in section 4.3) the satellite-based instrument selected to provide the data for the SIF retrieval is **SC**anning **I**maging **A**bsorption spectro**M**eter for **A**tmospheric **CH**artography (SCIAMACHY) since it provides measurements with sufficient spectral resolution and signal to noise ratio. Although SCIAMACHY has similar spectral resolution to some other instruments e.g. the Global Ozone Monitoring Experiment–2 (GOME-2), its spectral stability makes it preferable considering the resulted measurements inaccuracies (see section 5.6). A short description of the instruments and their main characteristics making them proper candidate is given below.

3.2.1 SCIAMACHY

SCIAMACHY was a grating spectrometer on board the ENVIromental SATellite (ENVISAT) [Burrows et al., 1995, Bovensmann et al., 1999] providing measurements at TOA based on passive spectroscopy. SCIAMACHY measured the extraterrestrial solar irradiance and the upwelling radiance (from Earth) in different viewing geometries and

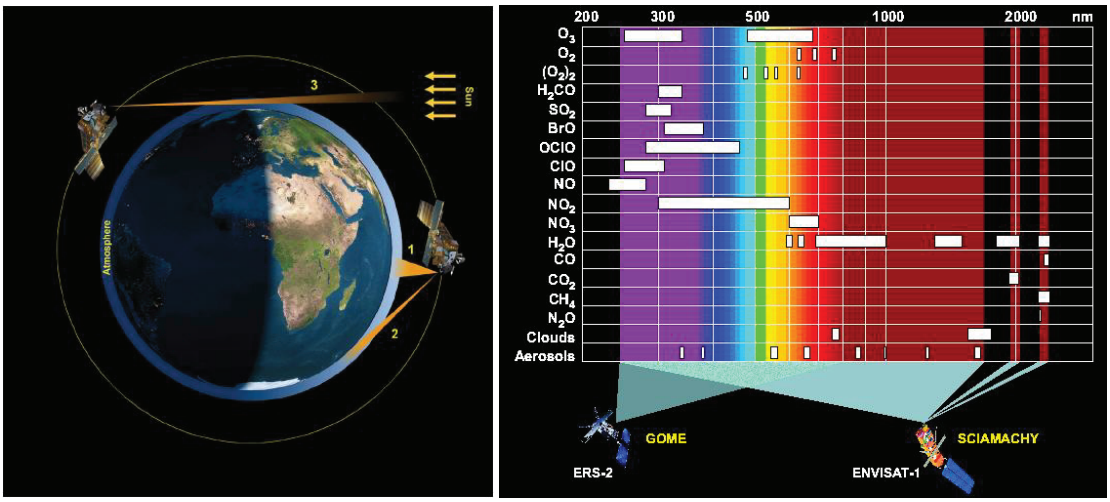

Figure 3.9: Left: SCIAMACHY in operation: 1. Nadir, 2. Limb and 3. Occulation viewing modes. (graphic: DLR-IMF). Right: The SCIAMACHY's spectral coverage, comparing to GOME. SCIAMACHY covers the spectral absorption regions of different trace gases, aerosols and clouds as shown. [Gottwald and Bovensmann, 2011]

in the ultraviolet, visible and near infrared spectral wavelength regions within 240 nm and 2380 nm at the spectral resolution of 0.2 to 1.4 nm. Its spectral band pass was divided into eight channels.

SCIAMACHY was launched in March 2002, on the ENVISAT having an equator crossing time of 10:00 a.m. which is reported to be suitable to retrieve SIF [Amorós-López et al., 2008]. Unfortunately, SCIAMACHY's mission ended in May 2012 after connection to ENVISAT was lost in April 2012.

The main scientific objective of SCIAMACHY was to measure trace gases in the terrestrial atmosphere by measuring the solar irradiance and its reflected radiance from the Earth. Moreover, due to its broad spectrum coverage, it was also providing information about aerosol properties and clouds (Fig. 3.9).

SCIAMACHY had different spatial resolutions depending on the integration time and operates in three main measurement geometry modes known as Nadir, Limb and Occulation modes. The measurement mode utilized for the current work is Nadir geometry, which is when the instrument is looking directly towards the Earth's surface. Therefore, it provides a direct measurement of the upwelling spectral radiance from Earth. The spatial coverage of the instrument was up to 960 km across track.

The solar reference spectrum is measured once a day, tracking the unattenuated extraterrestrial solar irradiance.

SCIAMACHY provides high quality measured radiances with relatively large Signal to Noise Ratios (SNR) for all measurement channels and modes. However, The largest

SNR is provided for channel 3 and 4 varying from $\sim$ 2000 to $\sim$ 11000 (Fig.4.11) [Gottwald and Bovensmann, 2011]. For the approach taken in here, measurements from channel four have been utilized. The nominal spatial resolution of the instrument in nadir mode is 60 km across track by 30 km along track which was considered to be sufficient for the objectives of the current work. Unfortunately the selected wavelength range (748.5-753.0 nm) is given at lower spatial resolution (due to the increase of integration time), leading to ground pixel sizes of 240 km across by 30 km along track. Accordingly the resolution of the retrievals (shown later) are useful wherever continuous vegetation prevails, such as the large tropical forests in South America and Africa. On the other hand it provides sufficient accuracy to specify the abilities, requirements and limits of the developed method.

Due to the following reasons SCIAMACHY was selected to be the first and main source of data to retrieve SIF:

- sufficiently high spectral resolution, necessary to detect spectral infilling of the Fraunhofer lines,
- sufficiently large Signal to Noise Ratio (SNR) (see section 4.3.2) and
- relatively high spectral stability and calibration.

SCIAMACHY level 1b data have been used and all relevant corrections/calibration measures have been applied, among them radiometric calibration, stray-light correction, correction for the memory effect, polarization and leakage current were the most important.

3.2.2 GOME-2

In the same way, GOME-2 measures the Earth's backscattered radiance and extraterrestrial solar irradiance. The spectral range of measurements is the ultraviolet and visible spectral range (240-790 nm). GOME-2 has moderate spectral resolution of $\sim 0.2 - 0.4$ nm from four detector channels. For the spectral region of interest for this work the measurement spectral resolution is 0.48 which is close to the spectral resolution of SCIAMACHY within this wavelength region. GOME-2 has been operating on Metop-A since 2006. The Metop-B operation started in 2012. The footprint size of GOME-2 is 80×40 km^2 and it is flying with 9:30 AM equator crossing time.

The Metop-A and -B data from GOME-2 have been selected for this study in addition to SCIAMACHY, since GOME-2 performs measurements in a comparable spectral and spatial resolution. Joiner et al. [2013a] reported the SNR of GOME-2 to be sufficiently large to retrieve fluorescence in far-red spectral region. Although the

outcome from Wolanin et al. [2015] and Köhler et al. [2015b] showed less spectral stability and larger noise in the fluorescence retrievals, GOME-2 has been frequently used for this purpose (see section 2.4). Therefore, it has been chosen as a candidate to apply the developed retrieval method on its measurements.

Chapter 4

Sensitivity and Uncertainty Analysis

The objective of this chapter is to justify the retrieval process described in the previous chapter and to compare the algorithm's sensitivity to the measurement conditions.

The need to explicitly consider the effect of spectral in-filling (ε_a from the previous chapter) in the retrieval process will be demonstrated, and the choice to retrieve SIF in the selected spectral region will be justified.

Finally, potential sources of uncertainty in the retrieval of the in-filling effect ε will be discussed, since any error in the retrieved ε (Eq. 3.16) directly propagates to the retrieved SIF value, as the in-filling caused by SIF and ε_a are of similar magnitude.

4.1 Parameterization of zero-offset effect

Retrieved values of the parameter ε are obtained solving the minimization problem Eq. 3.16. Individual retrievals of ε for one day of data as a function of the average radiance $\bar{I}_m$ (see Eq. (3.19)) are illustrated using color codes in Fig. 3.4. Only squares in green color show results retrieved over densely vegetated regions. All other colors and symbols show ε values for regions where SIF can safely be neglected (ε_a only). SCIAMACHY's radiance measurement contains an additive radiative component denoted above as ε_a which was first mentioned by Frankenberg et al. [2011b] regarding to the GOSAT measurements and referred to as the "zero-offset effect" (section 3.1.1).

In order to parameterize ε_a, values of ε are considered to be retrieved over regions which are free of vegetation. Fig. 3.4 also demonstrates that the ε_a values show a rather simple dependence on the measured average radiance and can be approximated by second order polynomial as introduced in Eq. 3.18. The fitted curve (black line), $\hat{\varepsilon}_a$, along with standard deviation curves (gray lines) represent the parabolic approximation of retrievals over non-vegetated regions. It can be also seen that the retrieved values of ε

over regions with vegetation appear to have a clear contrast and are well separated from the standard deviation curves in Fig. 3.4. The function given by Eq. 3.18 is considered to be a fair estimation of the additive signal which is not induced by SIF but other sources.

Taking into account that the accuracy of the scaling factor f depends on the accuracy of the approximation of $\hat{\varepsilon}_a$ (Eq. 3.20), non-vegetated pixels utilized for $\hat{\varepsilon}_a$ estimation should be selected optimally for the most adequate values of ε_a.

In order to separate the additive component caused by fluorescence, ε_f from any other additive contribution, ε_a, whether natural or instrumental, regions with minimum chlorophyll concentration have to be defined within no vegetation, thus no contribution by ε_f, is expected. Therefore, the regions selected in this study include the oligotrophic open ocean areas, deserts and northern regions of Greenland or Antarctica.

The potential impact of phytoplankton fluorescence which has its peak contribution near 680 nm with less wide spectral contribution than terrestrial SIF has been investigated. Maximum contribution by phytoplankton fluorescence to the wavelength range considered in this study has been tested with several most realistic simulations using SCIATRAN. No contribution for any numerical experiment using different realistic spectral widths of the Chl-a emission band could be found within these tests.

However, the oceanic regions chosen for ε_a estimations are compared to the ocean color maps provided by NASA's Earth Observatory group [Feldman and Kuring] to ensure the selection of oligotrophic regions. Therefore, no chlorophyll fluorescence-related contribution is expected when retrieving ε_a within the selected oceanic regions shown in Fig. 4.1 because of the strong absorption of water in the NIR and low concentration of Chl-a in such areas [Wolanin et al., 2015].

As stated in the previous chapter, potential mineral luminescence from desert sand and rocks might be part of the "natural" additive signal (as already pointed out by Joiner et al. [2012]). Wrong assumptions about the in-flight slit function of SCIAMACHY [Burrows et al., 1999] may be as well a source for increased levels of ε.

Additionally, as overcast or partly overcasted scenes exhibit a large span of different brightness levels, depending on the cloud fraction, such scenes are incorporated in the creation of the fit (Eq. 3.18) to derive $\hat{\varepsilon}_a$. The regions were also selected to ensure a broad spatial extent of overcasted scenes.

Temporal aggregation

To achieve a sufficient amount of retrievals to be able to reliably fit a $\hat{\varepsilon}_a$ curve the retrievals have to be aggregated temporally. One day of SCIAMACHY data led to

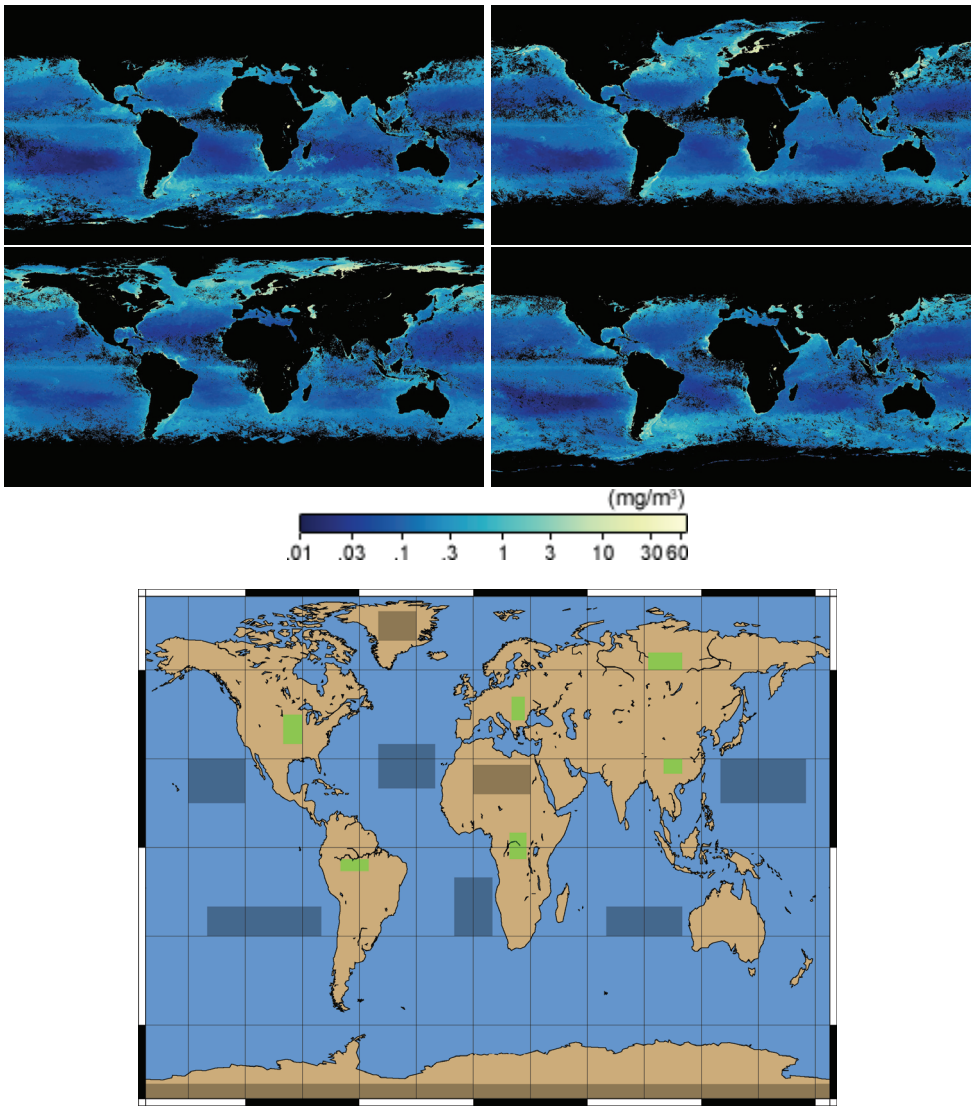

Figure 4.1: Above: The chlorophyll concentration maps [Feldman and Kuring] from January, April, August and November 2008 (top-left to bottom-right respectively). Below: the regions highlighted in gray are either barren land or expected to have the minimum Chl concentration and are selected for the ε_a estimations in this study.

around 1000 to 5000 values of ε on average when considering the above defined regions depending on the spectral window and the corresponding channel of the instrument. This leads to stable fits based on Eq. 3.18.

Fig. 4.2 (a,b) shows two daily examples, (for March 1st and and September 9th 2008) from the same spectral interval as the Fig. 3.4 ($748.5 - 753.0$ nm) according to Eq. 3.16 and Eq. 3.18. The dependence between the average radiance and ε is shown through a corresponding quadratic fit specifying $\hat{\varepsilon}_a$ as in Eq. 3.18. It can be seen that at moderate ε values depend nearly linearly on the average radiance. The gray solid lines represent the first standard deviation ($\pm\boldsymbol{\sigma}$) of the fitted $\hat{\varepsilon}_a$ curve.

The scatter around the fitted curves increases for larger average radiances. The most important reason for this is the range of validity of the determination of ε and thus ε_a, as the relationship between ε and $1/I^m(\lambda)$ is assumed to be linear in Eq. 3.16. One should note that the obtained ε over vegetated regions (as shown in Fig. 3.4) mostly lie within the ranges of average radiances where the linear assumption is still valid. This is due to the fact that the reflectance of vegetation, even in the far-red/NIR spectral range (spectrally located after the red-edge) is clearly smaller than the reflectance over bright sand or ice or thick clouds.

Accordingly, Fig. 4.2 (c) is an example of all fitted curves for the year 2008. Practically, all of them are confined within the standard deviation of one of the example curves (Fig. 4.2 (a) and (b)) for dark to moderately bright scenes (mean rad. $< 5 \times 10^{13}$ photons s^{-1} cm^2 nm^{-1} sr^{-1}). This also shows a rather stable offset feature over a time span of a year through different seasons. Repeating the same practice for other years (than 2008) showed a stable feature for all years. Retrieved data over vegetation were rarely exceeding the above mentioned level of mean radiance and corresponding fits to derive daily $\hat{\varepsilon}_a$-values are well suited to derive ε_f-values.

As illustrated in Fig. 3.4, the quality of the retrieval results are driven by the difference of ε and $\hat{\varepsilon}_a$-values. For many data points this difference will not always be as pronounced. Certainly, there are cases where values of ε_f were above the fitted but below the upper $\boldsymbol{\sigma}$-curve. Obtaining sufficient difference between ε_a from non-vegetated areas and ε values retrieved over vegetation strongly depends on the spectral window owing to the fact that the strength of SIF signal, at TOA varies with the biophysical status of plants and the measurement spectral wavelength.

4.2 Choosing the wavelength window

SIF emission occurs within a large spectral region roughly between 600 nm to 800 nm which is mainly affected by oxygen and water vapor absorption (Fig. 3.9) among which

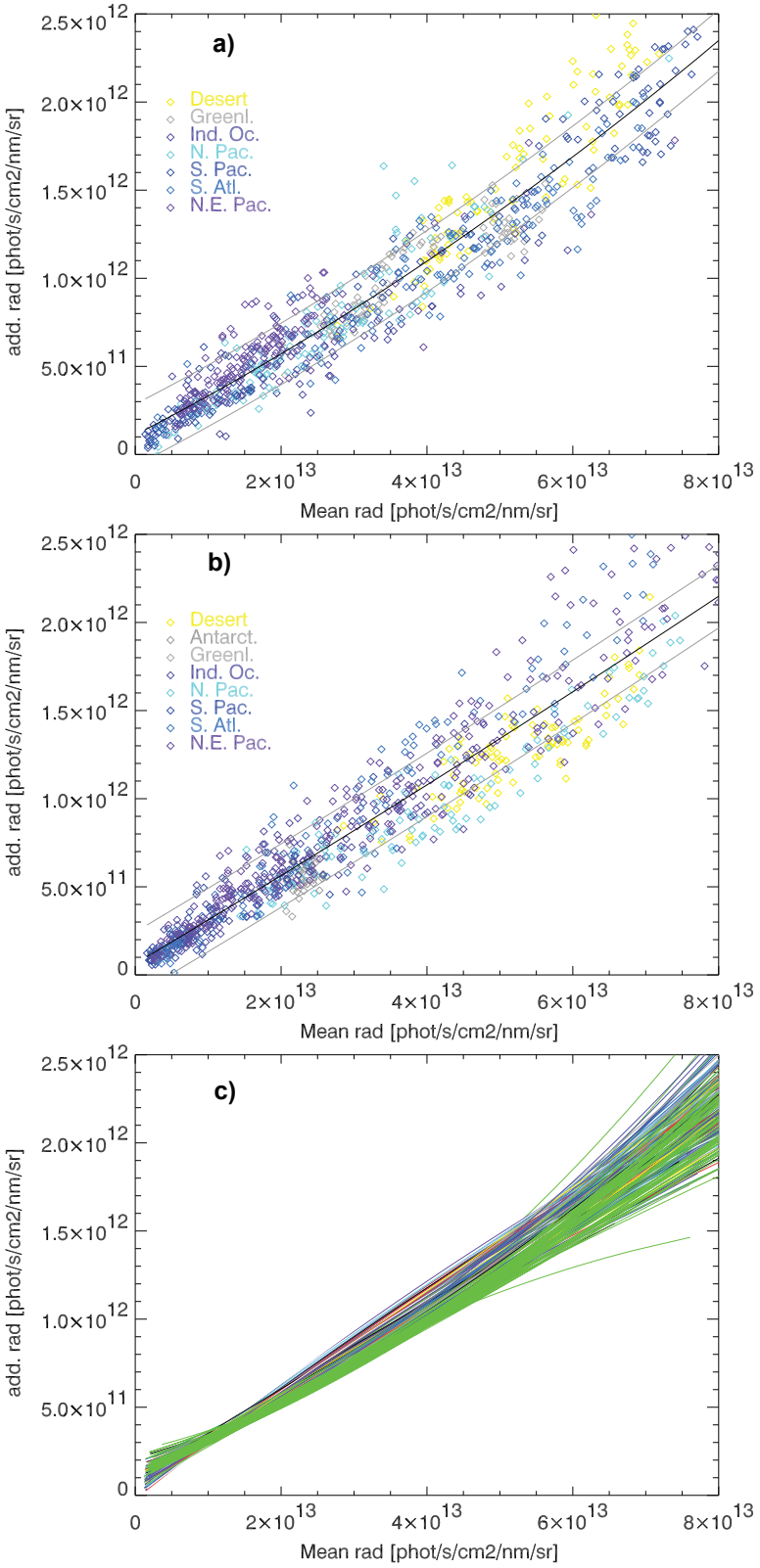

Figure 4.2: Dependence of ε (additive radiance component) on the mean radiance in the fit window for one day of data on (top) 9. Sept. 2008 and (middle) 1. March 2008 for regions defined in Fig. 4.1. Finally, all fitted curves for 2008 (bottom). The average slope is located at 0.02 and is well confined with $\pm$ 0.01.

O_2 is more homogeneously distributed in the atmosphere.
As stated by Frankenberg et al. [2012], the SIF signal retrieved inside the telluric absorption bands (e.g. O_2) will be distorted because of reduction of the upwelling signal due to absorption. In fact, there have been several attempts to retrieve SIF from O_2 absorption bands, but always the O_2 lines have been utilized combined with Fraunhofer lines [Joiner et al., 2011, Guanter et al., 2012, Joiner et al., 2013a, 2016, and the references therein]. As stated by Joiner et al. [2016], since the Fraunhofer lines have an extraterrestrial source their depths are not affected by surface pressure and temperature, aerosol and gaseous absorption and scattering as well as clouds and reflectance. Moreover, the SIF signal outside the telluric absorption bands is not absorbed passing through the atmosphere.

Therefore prior to further investigations, for the purpose of this work, the spectral regions with minimum to no gaseous absorption signature has been selected.

Several simulations have been conducted using the RTM, SCIATRAN (section 3.1.4), to find the most appropriate spectral ranges. Accordingly, two wavelength windows have been selected as shown in Fig. 4.3. These wavelength intervals lie near the red and far-red SIF maxima respectively, henceforth referred to as red and far-red retrieval windows:

1. The red window (682 - 685.5 nm), close to the O_2-B absorption band which is utilized by Wolanin et al. [2015] and Joiner et al. [2016] consists out of a single (relatively) pronounced solar Fraunhofer line. However, water vapor absorption cannot be neglected in this spectral range (see below). SCIAMACHY and GOME-2 provide spatial resolutions of 30×60 km^2 and 40×80 km^2 for this spectral region.

2. The far-red window (748.5 - 753 nm), close to the O_2-A absorption-band consists out of two strong solar Fraunhofer lines and although it cannot be considered to be free of H_2O absorption signature, the absorption features are negligible with respect to SIF. However, the spatial resolution of SCIAMACHY for this spectral range is a relatively coarse 30×240 km^2.

An advantage of retrieving SIF in both wavelength windows is that retrieving fluorescence from a combination of red and far-red SIF measurements provides more information on the vegetation status [Joiner et al., 2016]. For instance, some studies have been conducted on the effect of stress on the relative ratio of red to far-red SIF [Corp et al., 2010, Campbell et al., 2007, Zarco-Tejada et al., 2003, Daumard et al., 2010]. Although the SIF retrieval algorithms have been mainly focused on far-red SIF,

red-SIF has been retrieved from space-borne measurements by Wolanin et al. [2015] and Joiner et al. [2016] (after this study had been conducted). red-SIF has been retrieved from space-borne measurements by Wolanin et al. [2015] and Joiner et al. [2016] (after this study had been conducted).

Since the first step in the presented retrieval method is to obtain ε (and the corresponding $\hat{\varepsilon}_a$ curves in order to discriminate between SIF and the so-called zero-offset effect) the spectral windows have been assessed with respect to the retrieval of ε according to Eq. 3.16 based on simulated data. As Eq. 3.16 will be implemented frequently in this work, it will be referred to as the ε-fit hereafter to avoid repetition.

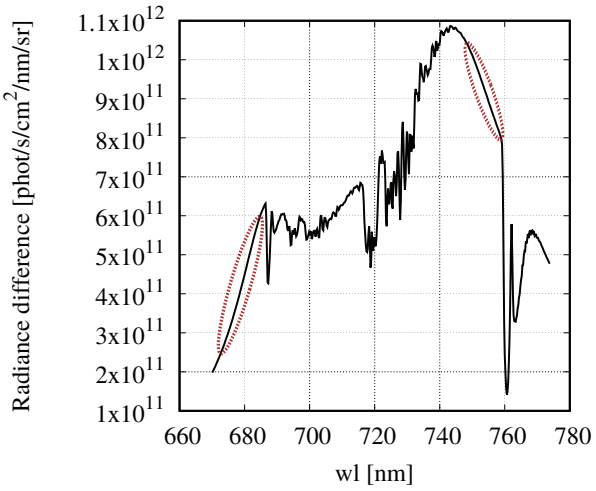

Figure 4.3: The difference between a sample I^+ and I^- which are modeled at TOA in presence and absence of SIF emission at TOC. Within the entire wavelength window of the SIF emission, the only spectral regions with minimum impact by telluric gaseous absorption are marked red.

.

Simulated SIF retrieval from the red window

As the first step, samples of $I^+(\lambda)$ were produced implementing a SIF emission spectrum in the RTM and ε is calculated from the ε-fit (according to Eq. 3.16). Bearing in mind that the only source of Fraunhofer line in-filling for such simulated radiance is SIF, the obtained ε should be equal to the known ε_f value as in Eq. 3.17. However, as shown in Fig. 4.4, the strong correlation between the H_2O absorption signature and the target Fraunhofer lines leads to retrieving a negative result from the ε-fit and the residuals follow the spectral shape of the H_2O absorption. This can be explained by the fact that the net in-filling of the chosen Fraunhofer line is negative since a larger

number of photons (within the Fraunhofer line width) are absorbed by water vapor than are added by fluorescence emission.

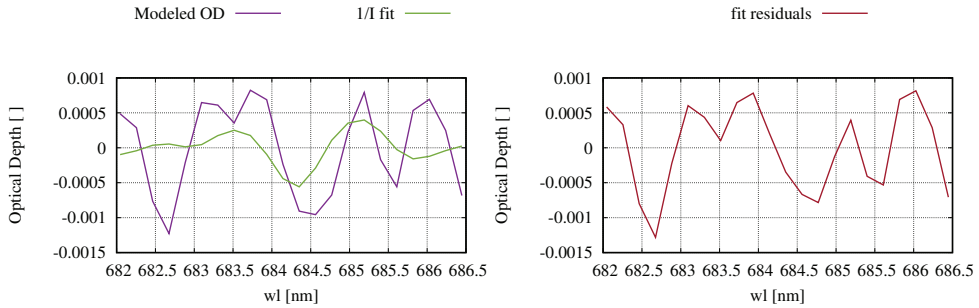

Figure 4.4: H_2O absorption features alternate the shape of Fraunhofer lines and as a result the retrieved ε is negative. Left: the modeled OD after removing the broadband features (purple) and the fitted $1/I^+$ (green). Right: The fit residual which is relatively large and comparable to the OD.

.

Numerical studies showed that the actual in-filling of the Fraunhofer lines can be disentangled from the H_2O absorption effect by modifying Eq. 3.16 to the following:

$$\left\| S^m(\lambda) - \frac{\varepsilon}{I^m(\lambda)} - hH(\lambda) - P_\varepsilon(\lambda) \right\|^2 \rightarrow min \ , \tag{4.1}$$

in which, $H(\lambda)$ is the spectral influence of H_2O on the radiance at TOA, also known as the H_2O optical depth (OD), and is defined as the natural logarithm of the ratio between radiances in the presence and absence of H_2O absorption in the modeled atmosphere ($I^{+H_2O}(\lambda)$ and $I^{-H_2O}(\lambda)$):

$$H(\lambda) = \ln \frac{I^{+H_2O}(\lambda)}{I^{-H_2O}(\lambda)} \ , \tag{4.2}$$

and h is the fit factor for H. It is worth mentioning that in order to separate the spectral signature of H_2O absorption and the in-filling by minimizing the correlation between them, the SIF emission $\mathcal{F}_b$ was not taken into account while producing $I^{+H_2O}(\lambda)$ and $I^{-H_2O}(\lambda)$ ($\mathcal{F}_b = 0$ in Eq. 2.24). Therefore, SIF has no contribution to the spectral shape of $H(\lambda)$ in the presented model results.

The fitted H and $1/I^m(\lambda)$ are presented in Fig. 4.5. The obtained $\varepsilon = 5.87 \times 10^{11}$ photons s^{-1} cm^2 nm^{-1} sr^{-1} is 98.7% similar to the average $\mathcal{F}_b$ for this spectral window ($\sim$ 5.95×10^{11} photons s^{-1} cm^2 nm^{-1} sr^{-1}), as the only source of in-filling for the simulated radiance.

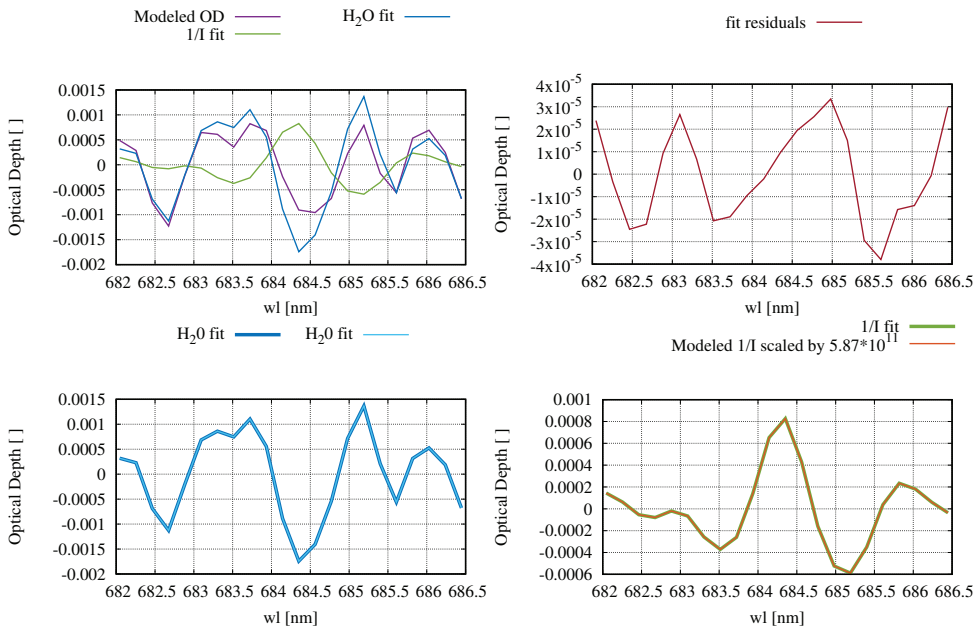

Figure 4.5: A sample of fit results implementing Eq. 4.1. Top-left: The fitted Logarithm of the Sun-normalized Radiance (LSR) simulated at TOA in presence of SIF and H_2O absorption. Top-right: the total fit residuals. The fit results of $H(\lambda)$ (bottom-left) and $1/I_m(\lambda)$ (bottom-right)

In essence, the model study confirms that for this wavelength interval the gaseous absorption is strong enough to be comparable with the in-filling effect of fluorescence. Therefore, the absorption effect has to be disentangled from the ε retrieval by fitting the absorption OD in the ε-fit process.

Consequently, the minimization of Eq. 4.1 is applied on one day of SCIAMACHY measurements over the selected regions free of SIF as well as the highlighted vegetated areas as shown in colors gray and green respectively in the Fig. 4.1. The retrieved ε_a values for different ground pixels from red wavelength window for a single day is shown in Fig. 4.6 (gray dots) together with ε values obtained over vegetated regions (green dots) which are known to be affected by SIF in addition to the zero-offset effect. It can be clearly seen that the ε values obtained from the vegetated and non-vegetated regions overlap to a high extent. To examine the distribution of the retrievals from vegetated and non-vegetated measurements, all the ε values over non-vegetated areas for the year 2008 are binned and the frequency of occurrence for the $\varepsilon_f = \varepsilon - \varepsilon_a$ is plotted in Fig. 4.6 (gray color). The maximal number of occurrence, corresponding to ε_f values for non-vegetated measurements is zero. The same exercise was repeated for ε values retrieved over vegetated regions, illustrated in Fig. 4.6 (green color). Although the average ε_f over the vegetated areas is larger than zero ($\sim 0.2 \times 10^{12}$ photons s^{-1} cm^2

nm^{-1} sr^{-1}), the overlap between vegetated (green color) and non-vegetated (gray color) distributions is significantly large. Since in the transition zone of both distributions the SIF retrieval is potentially hampered by other factors creating the additive component, the potential SIF retrieval in this condition can be highly affected.

There are several reasons for this outcome which are summarized in the following:

- One possible explanation is the larger standard deviation $\boldsymbol{\sigma}$ of the ε values retrieved from Eq. 4.1 for the red window than from Eq. 3.16 for far-red window (Fig. 4.6 versus Fig. 4.2). Uncertainties might have been introduced by fitting $H(\lambda)$ as long as the water vapor profile can vary significantly based on topological and environmental characteristics of the target region.

- Re-absorption of the red SIF signal within the canopy [Fournier et al., 2012, Porcar-Castell et al., 2014, and section 2.1.4 of the current work] which leads to a weaker red than far-red SIF signal at TOC and TOA respectively. The smaller ε_f, the less pronounced it appears to be related to the zero-offset in-filling ε_a.

- The uncertainties solving Eq. 4.1 are higher when the spectral wavelength window consists of a single solar Fraunhofer line which is not as deep as the two Fraunhofer lines within the far-red window.

- Since the red window is spectrally located before the red-edge, due to smaller reflectivity of vegetation in this spectral range the resulting radiance at TOA has smaller intensity. Therefore, the corresponding SIF signal is more probable to be affected by the instrumental noise than in far-red window (see section 4.3.2 on SNR).

The utilization of O_2-γ and O_2-B absorption bands together with the solar Fraunhofer lines is reported by Joiner et al. [2016] to provide more information on red SIF emission amplitude. The method applied in their study is the Principal Component Analysis (PCA) which does not share many similarities with the approach taken here except that orthogonal spectral information is fitted to measured spectra. Although red SIF is successfully retrieved by Joiner et al. [2016] their results are also reported to be more sensitive to the environmental properties (soil moisture) than the far-red SIF. The principal components implemented by Joiner et al. [2016] might compensate for the H_2O absorption variations. Additionally, O_2-γ, located in a SIF-free spectral region, is used as an indicator for more accurate assumptions of O_2 absorption effect over each measurement target.

On the other hand, Wolanin et al. [2015] reported sensitivity of their retrieval method to water vapor concentration as well as Raman scattering. Their retrieval method is

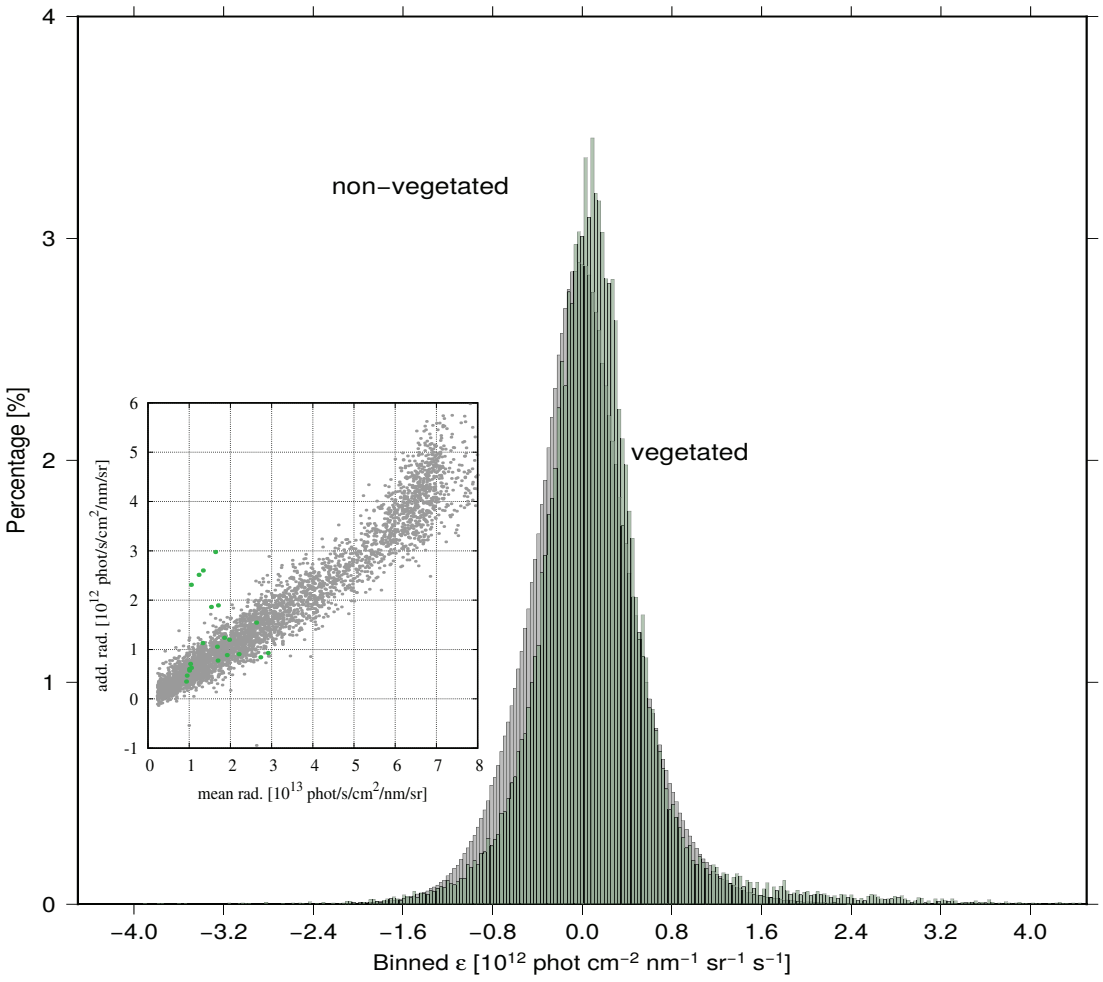

Figure 4.6: The histogram of the distribution of ε values retrieved for the red window (682 - 685.5 nm) for both vegetated and non-vegetated regions shown in green and gray respectively. Inside the frame of the histogram, the ε retrieval for one day of SCIAMACHY red window measurements is shown. The vegetated (green) and non-vegetated (gray) pixels are partially mixed.

based on a least square fitting method which has more similarities to the method used in this study. Wolanin et al. [2015] introduced two additional wavelength windows to retrieve H_2O concentration and Raman retrieval separately to correct their obtained SIF values accordingly. This could be a possible solution for the SIF retrieval from the red window in the current work and has to be investigated.

In summary, to detect the relatively small red ε_f signal a more adequate estimation of H_2O concentration for each measurement is necessary in order to obtain more realistic estimations of ε which furthermore improves the SIF retrieval quality due to reduction of the uncertainties for the retrieved ε values.

Simulated SIF retrieval from the far-red window

Unlike the red window, the far-red window is not strongly affected by H_2O absorption. Therefore, the minimization Eq. 3.16 is implemented to retrieve the in-filling (ε).

Again, as a "self-consistency" test for the method, the RTM has been utilized to simulate $I^+(\lambda)$ spectra within the far-red window ($748.5 - 753.0$ nm) at TOA and the SIF emission is assumed to be the only additive component to the modeled radiance. A sample of ε fit, together with the residuals are presented in Fig. 4.7 (top). The obtained ε is 99% equal to the ε_f as expected. The remaining 1% difference can be explained by the fact that ε_f is retrieved approximating SIF using only the linear term of Taylor expansion (see Eq. 3.5). Thus, SIF is assumed to be independent on the spectral wavelength within the narrow far-red window. However, the implemented fluorescence emission spectrum in the model ($\mathcal{F}_b$) has $\sim 10\%$ variation within the far-red window (see section 4.3.1). Thus, only 1% deviation from the average value is acceptable.

A combination of SIF and a spectrally constant additive signal (representing the zero-offset feature) have been used to model $I^+(\lambda)$ at TOA. The latter is added to the $I^+(\lambda)$ at TOA manually in replacement of an actual measurement. The additive signal is assumed to be wavelength independent as well (see section 4.3.1). Applying the ε-fit, the obtained ε equals the $\varepsilon_a + \varepsilon_f$ by 97% as expected. The fit and its residuals are presented in Fig. 4.7 (middle).

Finally, random noise has been introduced to the modeled radiance to produce a realistic scenario. Random noise has been produced according to the Signal to Noise Ratio (SNR) for the SCIAMACHY instrument within this channel (see section 3.2.1) and radiance intensity. A value of SNR$= 4000$ (see section 4.3.2) is added to the simulated $I^+(\lambda) + \varepsilon_a$. The ε-fit result and residuals (Fig. 4.7 (bottom)) show a perturbation with respect to the previous condition. Based on a 10000[1] times application

[1] this number is shown to be sufficiently large to create a set of values normally distributed around the

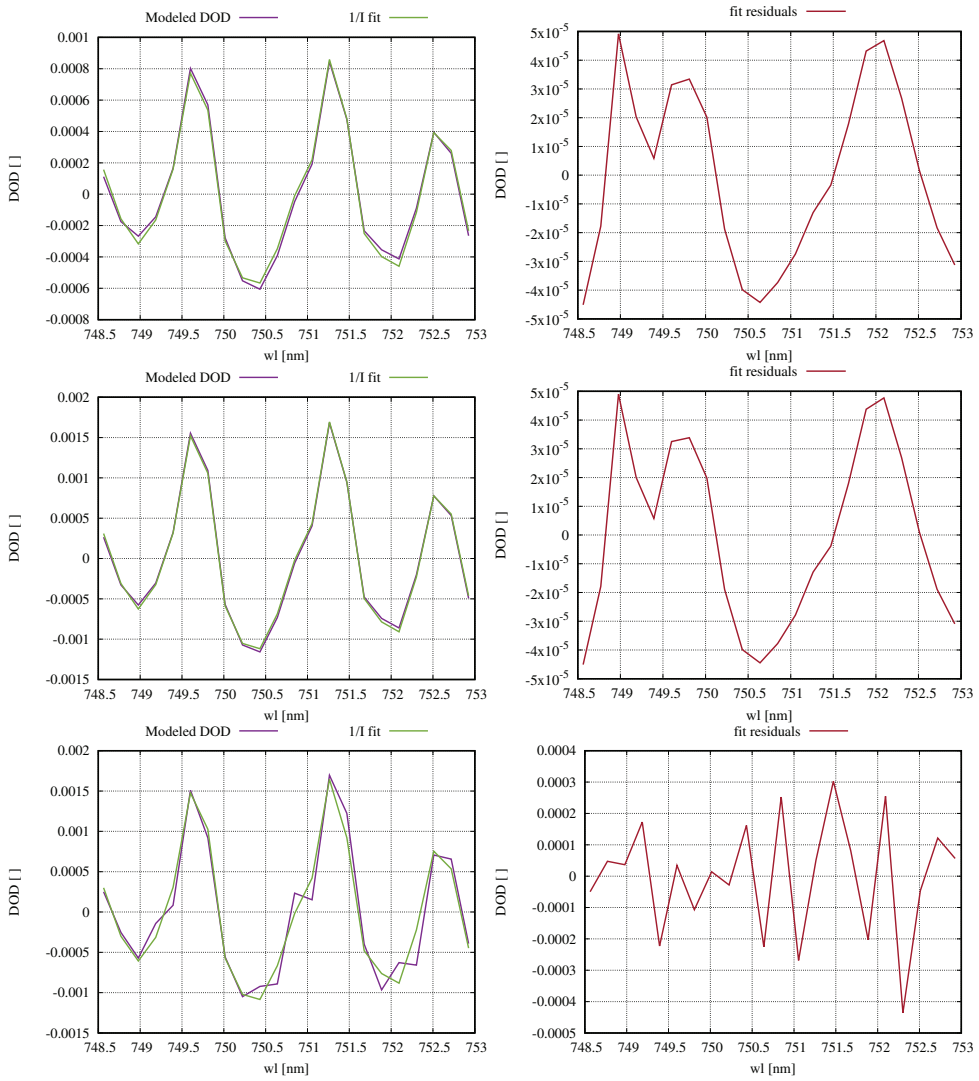

Figure 4.7: Top: Fitted $1/I^{+}(\lambda)$ for simulated radiance in presence of SIF emission within the far red window (left) and the fit residuals (right). Middle: The same fit for $1/(I^{+}(\lambda)+\varepsilon_a)$ in which simulated ε_a is assumed to be spectrally independent (left) and the fit residuals (right). Bottom: The same fitting results for the modeled $1/(I^{+}(\lambda)+\varepsilon_a+\delta)$ (left) in which δ is a random error 4000 times smaller than the $I^{+}(\lambda)$ signal. The fit residuals being significantly larger than other two scenarios are presented in left.

of the random noise the retrieved ε values are found to have an average equal to $\varepsilon_a + \varepsilon_f$ (as expected) and a standard deviation of 1.3 $\times 10^{11}$ photons s^{-1} cm^2 nm^{-1} sr^{-1} which implies an error of 11% in estimating ε due to SNR within this range.

It is worth mentioning that although the far-red spectral window is assumed to be free of telluric absorption, it is influenced by weak spectral features from H_2O absorption. Numerical studies based on SCIATRAN simulations showed an up to 12% overestimation of ε due to the perturbation of the signal because of H_2O absorption. Unlike the red window, the effect of H_2O in the far-red window is small and can be corrected based on the seasonal and latitudinal variation of the atmospheric H_2O profile. The global average atmospheric water vapor is presented in Fig. 4.8. Numerical model studies showed that the higher amount of atmospheric H_2O in the tropics lead to an overestimation of ε values up to a maximum of 15%. Comparing the average error in estimating ε due to the random noise ($\sim$ 11% for SNR $=$ 4000) the H_2O effect does not seem to disturb the retrievals (see section 4.3.2). However, since the retrieval error due to water vapor always applies a positive bias to the retrieval, the SIF retrieval results over tropical regions might be somewhat larger than the true values. To the first degree of approximation, the final results could be corrected by latitudinal scaling (see Fig. 4.8).

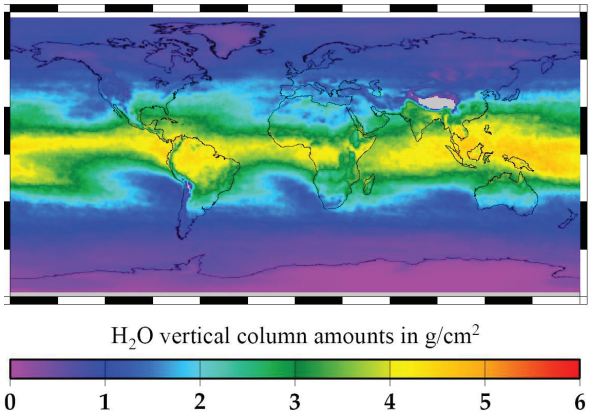

Figure 4.8: The average atmospheric water vapor concentration for the year 2006 from SCIAMACHY measurements [Mieruch et al., 2008].

In order to assess how well values of ε_f are separated from $\hat{\varepsilon}_a$ (and the corresponding $\boldsymbol{\sigma}$ curve), again all ε_a values, obtained in absence of vegetation, are binned and the frequency of occurrence of $\varepsilon_f = \varepsilon - \hat{\varepsilon}_a$ has been plotted for one year of data

mean which equals to the value in absence of random noise. Therefore 10000 repetition of the exercise is statistically representative.

(2008) making up about 300.000 retrievals. The result is the histogram in Fig. 4.9 (gray columns) corresponding to ε-retrievals over regions (specified by gray boxes) in Fig. 4.1.

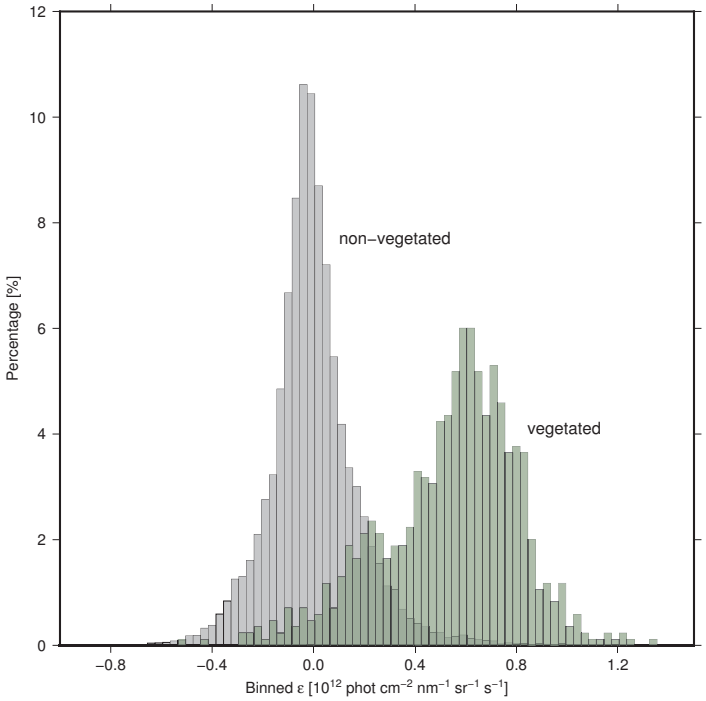

Figure 4.9: Distributions of values of ε for far-red window (748.5 - 753 nm), calculated for vegetated and non-vegetated regions shown by green and gray colors, respectively.

.

The ε retrieval procedure has been repeated for fully vegetated regions (ε-retrievals over green-colored regions, Fig. 4.1, for the year 2008 for about 10.000 retrievals) and again, the $\varepsilon_f = \varepsilon - \hat{\varepsilon}_a$ values have been calculated and plotted (green) as a histogram in Fig. 4.9. While the gray distribution is centered around zero (as expected), the maximum value of the green distribution is shifted to about 0.5 $\times 10^{12}$ photons s^{-1} cm^2 nm^{-1} sr^{-1}. In the zone were both distributions are well separated and f can be retrieved uniquely from Eq. 3.20. Where the two distributions overlap, the SIF retrieval is potentially hampered by other origins creating the additive component, such as for example instrumental effects.

To summarize, so far a suitable spectral range for the retrieval is chosen. The obtained results from the far-red window numerical simulations confirm the feasibility of retrieving SIF from the far-red window. However, the effects of the measurement conditions and atmospheric properties on the spectral signature of SIF and the dependence of

vegetation fluorescence on measurement properties still has to be assessed. Additionally, since some of the measurement properties (e.g. reflectance (A) and aerosol optical depth (AOD)) are not known as a priori and have to be approximated, their contribution to the retrieval have been studied. Moreover, considering the fact that Raman scattering has also an in-filling effect on the solar Fraunhofer lines it has been compared and analyzed with respect to the retrieval method utilized for this work. In addition, the effect of clouds and the sensitivity of the method to some fundamental assumptions are examined as well within the next section.

4.3 Sensitivity study

The SIF retrieval method discussed in chapter 3 is examined with respect to the atmospheric and measurement properties which affect the measured radiance at the TOA. From the radiative transfer equation discussed in chapter 2, it becomes clear that the illumination and measurement geometry as well as the absorption, scattering and reflection of light play crucial roles on measured radiance.

However, since the measurement geometrical properties (illumination and measurement zenith and azimuth angles) are known for each measured radiance at TOA, the most adequate FR spectrum with this respect can be provided by SCIATRAN simulations. Therefore, the focus of this section is to study the sensitivity of the retrieval method to the light and ground/atmosphere interactions. The uncertainties due to the SNR of the instrument affect the retrieval and have to be quantified as well.

So far, the SIF emission spectrum implemented in all the modeled data as well as the FR spectra was the $\mathcal{F}_b$ for velvet grass provided by Rascher et al. [2009]. The effect of this assumption is discussed in the following.

4.3.1 SIF retrieval at the TOA and the a priori SIF emission spectra

The spectral shape of the canopy level fluorescence varies with respect to time and species as well as the density of the vegetation and canopy characteristics (e.g. Fig. 4.10). However, a smooth descending behavior is always expected within the narrow spectral window selected here and has been referred to as far-red window so far. The total change of the SIF emission spectrum, $\mathcal{F}_b$, utilized in this study from Rascher et al. [2009] in the corresponding far-red wavelength range is ~ 0.3 mW m^{-2} sr^{-1} nm^{-1} or $\sim 5.1 \times 10^{11}$ photons s^{-1} cm^2 nm^{-1} sr^{-1}. However, in the developed forward model, it is considered to be wavelength independent and therefore, its **average** value within this spectral range is retrieved solving the inverse problem.

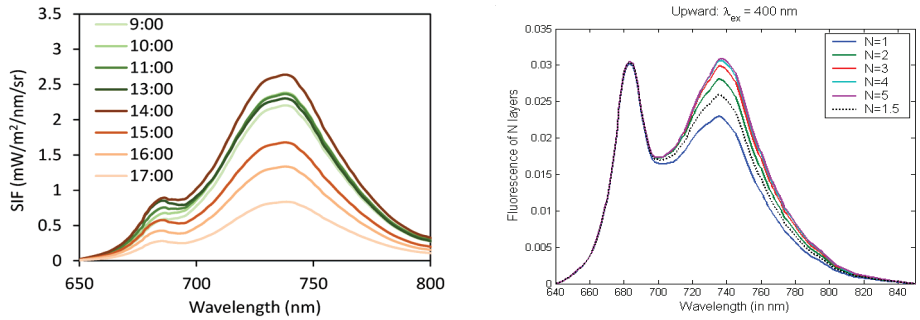

Figure 4.10: Left: The full-spectrum SIF retrieved by Liu et al. [2015] in April 25th, 2015. The results are plotted from 9:00 a.m. to 5:00 p.m. Right: Simulated chlorophyll fluorescence calculated for N layers of Chlorophyll molecules exposed to radiation with $\lambda = 400$ *nm [Miller et al., 2003].*

To assess the sensitivity of the retrieval method to the SIF emission spectrum, SCIATRAN is utilized implementing the following three SIF emission spectra:

1. independent on wavelength,
2. with a larger slope than the original $\mathcal{F}_b$ with respect to wavelength,
3. with a smaller slope than the original $\mathcal{F}_b$ with respect to wavelength,

and a fixed spectral mean value. Comparing the ε retrievals from the corresponding ε-fits for these three hypothetical SIF emission spectra, it has been confirmed that the variation of a priori fluorescence emission spectrum does not change the retrieved ε significantly. The retrieved ε_f does not significantly differ from the mean of emission spectrum, independent of the spectral shape of its emission spectrum. As stated before, this can be explained considering that, while deriving Eq. 3.5, a linear approximation of the Taylor expansion has been taken into account and therefore, SIF is assumed to be independent on the spectral wavelength. Hence, within this wavelength window, SIF can be safely set to a single a priori spectrum.

Additionally, the numerical simulations confirmed that obtaining a single value as an average SIF within the spectrally narrow far red window is a reasonable approximation since the expected spectral variation of the SIF emission spectrum is relatively small. As stated before, 10% variation in a priori SIF emission signal leads to 1% deviation of its mean value for the retrieval.

In the forward model, the additive ε_a signal is assumed to be a function of radiance intensity. It is also assumed to be wavelength independent and comparable with SIF emission spectrum since they are both approximated by the linear term of Taylor

expansion (see above and section 3.1.1). Additionally, within the narrow far-red spectral window the spectral shape of ε_a is not of interest for this study, bearing in mind that only a single ε value is retrieved for the entire spectral window for each measurement.

4.3.2 The instrument's SNR and SIF retrieval

SNR is defined as the ratio between the measured signal to the noise (δ); SNR $= \frac{I^m}{\delta}$ and has no units. Fig. 4.11 shows the expected SNR for all channels and measurement modes of SCIAMACHY.

Since nadir measurements are utilized here, the minimum and maximum SNR for the selected channel, 4, is given as $\sim$ 2000 for minimum signals (low intensity) to $\sim$ 11000 for high intensity (maximum) signals.

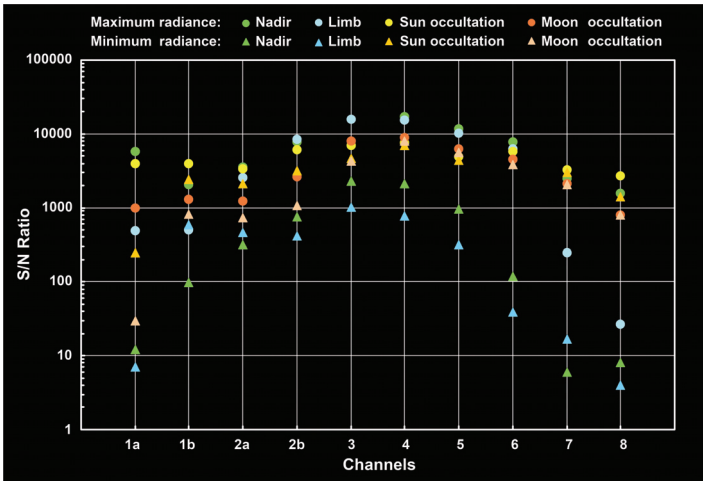

Figure 4.11: The signal-to-noise ratios (SNR) for all channels as obtained during OPTEC-5 tests [Gottwald and Bovensmann, 2011] for minimum and maximum radiance signals. (Courtesy: DLR-IMF)

SIF is only a small percentage of the total upwelling signal at the TOA. Therefore, the potential influence of the SNR on the retrieval is of importance.

The mean measured radiances are presented in Fig. 3.4 and 4.2. The distribution of the mean radiance values shows that the minimum radiance intensities are expected over non-cloudy oceanic regions, in the same way that the largest radiance magnitudes are from cloud/ice covered pixels where reflectance is larger. Consequently, a set of $I^+(\lambda)$ scenarios are simulated ranging from minimum to maximum average radiances ($\bar{I}^m$) representing SCIAMACHY measurements as close as possible. To model a realistic noise dependent variation of ε retrieval, for each $I^+(\lambda)$ scenario, 10000 random errors have been generated according the adequate SNRs and the corresponding ε has been

retrieved. The results are presented in Fig. 4.12. The standard deviation of the obtained ε values for minimum and maximum radiances (corresponding to the maximum and minimum SNR respectively) are 1.08 and 1.70 $\times 10^{11}$ photons s^{-1} cm^2 nm^{-1} sr^{-1} which is one order of magnitude smaller than the expected ε_f values within the far-red spectral window (from 10 to maximum 17%). The obtained standard deviations are acceptable bearing in mind that the variation of SIF within this spectral window is $\sim$ 5.1 $\times 10^{11}$ photons s^{-1} cm^2 nm^{-1} sr^{-1} (see section 4.3.1 for details). To conclude, the expected SNR values for SCIAMACHY in channel 4 are not found to be significant for the proposed retrieval method. Given this, the sensitivity of the method to the measurement conditions and setup has to be assessed, specially since not all of the environmental factors for each measured condition are accurately known. In particular, the measurement conditions define $F(\lambda)$ which is utilized to obtain C_a from Eq. 3.14. Thus, in the following section sensitivity of the FR to the uncertainties in estimating environmental/measurement factors has been assessed.

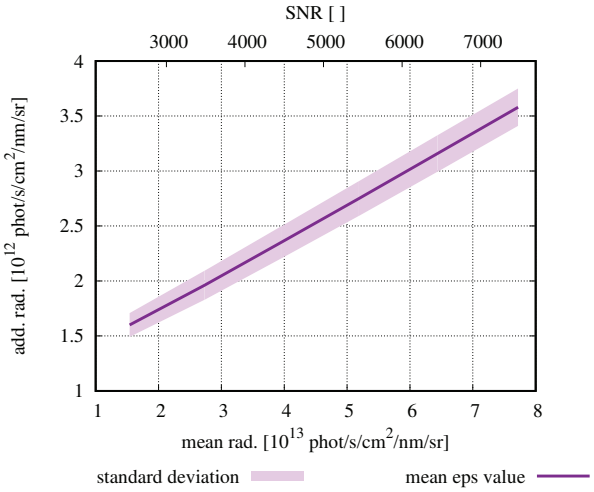

Figure 4.12: Sample ε values versus mean radiance; The true ε values and the SNR estimations are prepared based on realistic expectations of $\hat{\varepsilon}_a$ and SNR for SCIAMACHY within the selected wavelength window.

4.3.3 Fluorescence reference spectrum and measurement characteristics

To recap the SIF optical depth, $F(\lambda)$, equals to $\ln\left(I^+(\lambda)/I^-(\lambda)\right)$ (Eq. 3.4). One can see that the larger the radiance, the smaller is the FR because of smaller difference between I^+ and I^-. In fact, although the broadband spectral features (e.g. reflectance and elastic scattering) are removed from the measured OD using polynomials, the $F(\lambda)$ spectrum remains influenced by the magnitude of the measured radiance (also

referred to as the brightness of the scene). This means, FR is affected by the ground reflectance as well as the topography of the measurement target and the concentration of scattering molecules and particulate matter in the atmosphere. To examine the influence of geometry, surface reflectance and AOD on the retrieval method, the dependence of the FR spectrum on them has been investigated. While the situation for the measurement geometry is simple, as it is given alongside with the satellite product, the actual surface reflectance and AOD are not known a priori and should be approximated for the retrieval. Therefore, their significance to the spectral signature of SIF has to be analyzed.

To do so, a set of FR values are produced for a single spectral point of 751.26 nm (inside a Fraunhofer line within the far red window) utilizing the RTM by implementing a variety of AOD and Lambertian ground reflectance (A). The results are plotted with respect to the variation of surface reflection, in Fig. 4.13 (left). It can be clearly seen that larger albedo leads to smaller FR values as expected, since the relative significance of the SIF signal is smaller compared to larger background radiances (see Eq. 3.5). This has been tested by plotting the FR values for the same wavelength based on the solar zenith angle (SZA) variation instead of albedo. The results (Fig. 4.13-right) confirm that for smaller solar zenith angles (larger radiance), FR is less significant and accordingly less sensitive to AOD uncertainties.

The expected surface reflection, A, within the far-red spectral window is between $\sim 20 - 40\%$. From the Fig. 4.13 one can see that within this range FR is not drastically changing with AOD. Therefore, uncertainties in AOD assumptions are not significantly disturbing the SIF retrieval in this spectral window.

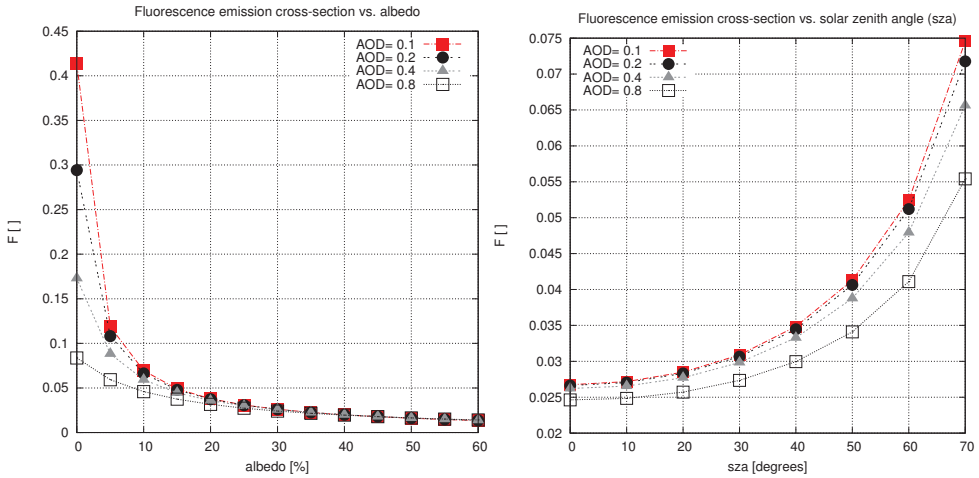

Figure 4.13: The dependence of the FR spectrum, F, on (left) ground reflectance, albedo, and (right) solar zenith angle together with AOD.

Among the retrieval factors which can potentially affect the SIF retrieval, Raman scattering (which also has an in-filling effect in absorption lines) have been investigated by Sioris et al. [2003] and its effect has been reported to not to be on a comparative level with fluorescence. Later on, Joiner et al. [2012] discussed the effect of the RRS and VRS on SIF retrieval for SCIAMACHY at 866 nm and reported insignificant influence of it on their retrieval. However, since the retrieval approach taken in the framework of this dissertation is different from their approach, the importance of RRS for the retrieval method presented in this study is assessed.

4.3.4 Significance of Raman scattering

As explained in section 2.2.3, inelastic scattering has an in-filling effect in the absorption (Fraunhofer) lines. The reason is that the scattered photon has a different energy (wavelength) than the incident photon which leads to a spectral redistribution of the scattered photons.

A study by Lampel et al. [2015] in the visible (blue) spectral range showed that the effect of VRS for fitting methods similar to what is utilized in the framework of this study is negligible if the Root Mean Square (RMS) of the fit is larger than 4×10^{-4}. Considering the fact that VRS (due to its dependence on wavelength) is even smaller in the red and far-red spectral region, the RMS for the fits demonstrated here (4.1×10^{-4}) is allowing the neglection of VRS in the framework of this dissertation.

Joiner et al. [2012] and Wolanin et al. [2015] reported that they had to take Raman scattering into account while retrieving SIF. For instance, Joiner et al. [2012] used SCIAMACHY measurements for a Fraunhofer line at 866 nm, stating that Raman scattering is strongly dependent on the SZA. However, for the near-infrared spectral range and SZA< 60 the total in-fillings of the RRS and VRS are reported to be less than 0.1% and 0.05% respectively. Wolanin et al. [2015] however, did not neglect the effect of RRS and fitted Raman scattering for their fluorescence retrieval. Although, since the "zero-offset effect" is not mentioned by the authors, their so-called "Raman scattering fit" might have compensated for such unknown in-filling effects as well.

Again, the RTM is utilized to produce $I_R^-(\lambda)$ at TOA, which represents a sample radiance in absence of SIF emission but presence of RRS in the atmosphere. The natural logarithm of the radiance influenced by the RRS effect and the radiance free of RRS effect in absence of SIF emission ($R = \ln \frac{I_R^-}{I^-}$) is compared to FR produced in absence of RRS. Fig. 4.14 illustrates the relative impact of RRS and SIF on the simulated radiance. The different spectral shapes of $F(\lambda)$ and $R(\lambda)$ as shown in Fig. 4.14 (top) are due to the different origins of the two in-filling effects. What causes the RRS

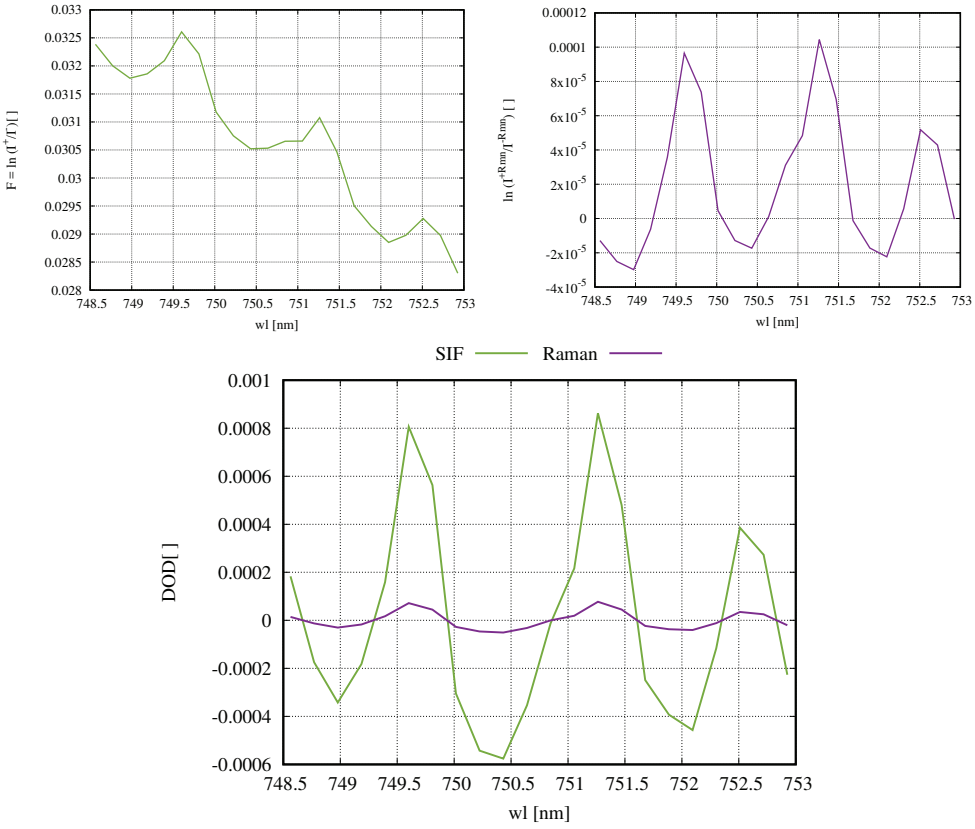

Figure 4.14: The relative in-filling effect of a TOA radiance sample due to the Raman scattering comparing to the FR. Top-left: $F(\lambda)$ before subtracting the polynomial. Top-right: $R(\lambda)$ before subtracting the polynomial. Bottom: $F(\lambda)$ and $R(\lambda)$ after removing the broadband spectral structures (in the form of DOD) and their relative magnitude (green for F-DOD and purple for R-DOD)

in-filling effect is the spectral redistribution of the photons, unlike SIF which is an additive signal within a limited spectral region. Bearing in mind that all the broadband features are excluded from the Eq. 3.16 by subtracting polynomials, the net in-filling effect of SIF and RRS after removing the polynomials are compared in the Fig. 4.14 (bottom) to show their relative magnitude as perceived by the retrieval algorithm. For the above reasons, the ε-fit has been conducted on simulated radiance $I_R^-(\lambda)$. The only source of in-filling effect in this case is RRS. As shown in Fig. 4.15 (top), the obtained $\varepsilon = 0.07 \times 10^{12}$ photons s^{-1} cm^2 nm^{-1} sr^{-1} instead of zero which is two orders of magnitude smaller than the typical ε_f values $\sim 1.00 \times 10^{12}$ photons s^{-1} cm^2 nm^{-1} sr^{-1}.

The in-filling effect due to SIF dominates the in-filling due to RRS in this wavelength region. To compare the spectral in-filling of RRS and SIF, the ε-fit has been conducted on the modeled $I^+(\lambda)$ in the absence of Raman effect and in the presence of SIF emission. The fit results are shown in Fig. 4.15 (middle). The obtained ε is 99% similar to the expected averaged SIF emission spectrum over the far-red window indicating that (comparing to fluorescence) RRS had no significant influence on the depth of the Fraunhofer lines.

Finally, simulating a realistic case in which the modeled radiance is affected by both SIF and RRS ($I_R^+(\lambda)$), the ε obtained from the similar fit is to 93% similar to the expected ε_f ($\varepsilon_a = 0$). This is in agreement with the findings of previous studies conducted by e.g. Sioris et al. [2003] and Joiner et al. [2012]. The RRS-induced in-filling is found to be two orders of magnitude smaller than SIF (RRS $\sim 10^{10}$ vs. SIF $\sim 10^{12}$ photons s^{-1} cm^2 nm^{-1} sr^{-1}).

The corresponding fit results are presented in Fig. 4.15 (bottom) together with the residuals. Assuming the unavoidable systematic uncertainties in the retrieval results due to the assumptions on SIF emission spectrum and the random error due to SNR (10 - 17%), the potential error due to RRS ($\sim 7\%$) can be safely neglected.

To conclude, the spectral signature of SIF is the main reason for the Fraunhofer line in-filling and the presence of RRS does not impose a significant difference since the RRS effect is found to be smaller than the minimum error due to random instrumental noise. Therefore, the Ring effect can be considered negligible for SIF retrieval within the framework of this study.

4.3.5 The effect of clouds

Retrieving the ε_a values is conducted over ocean, desert and ice without applying any cloud-filter, aiming to cover a large variety of radiances within which SIF emission

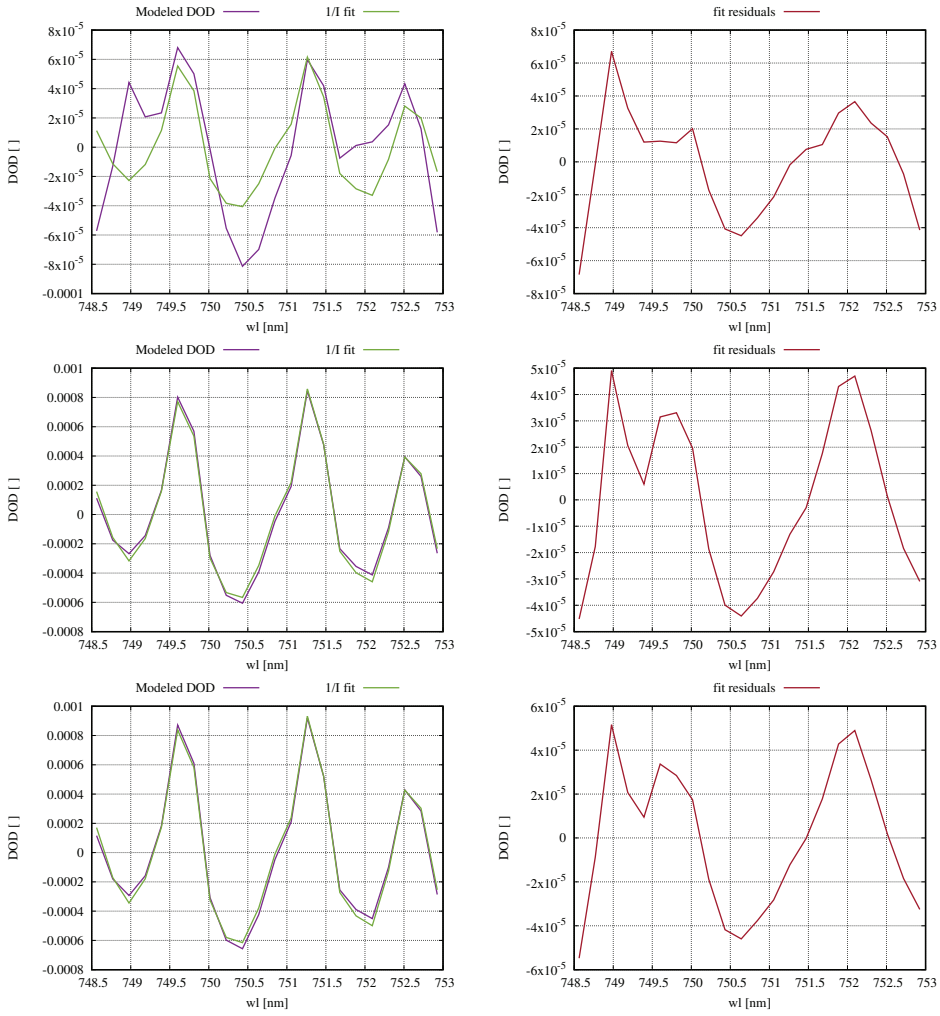

Figure 4.15: Top: The fitting results from the ε-fit for a radiance sample at TOA in absence of SIF for the simulated radiance including only Raman scattering, $I_R^-(\lambda)$.
Middle: The same fit for a TOA radiance in the absence of Raman scattering and presence of SIF, $I^+(\lambda)$ (SIF emission being $\bar{\mathcal{F}}_b = 1.01 \times 10^{12}$ photons s^{-1} cm^2 nm^{-1} sr^{-1})
Bottom: the same fit including SIF and Raman effect, $I_R^+(\lambda)$. All results are shown together with their corresponding residuals in the left side.

is zero. However, cloudiness can influence the SIF signal reaching TOA as well as distorting the retrieval by changing the scattering pattern. Given this, the sensitivity of the retrieval method to cloudiness has to be assessed since clouds can mask some spectral information as well as alter the reflectivity of the measurement target which is related to the ε calculations.

Joiner et al. [2013a], Köhler et al. [2015b] and Joiner et al. [2016] reported low sensitivity of their results to cloud contamination. Therefore, the cloud filters implemented for these studies are reported to be "relaxed". Indeed Köhler et al. [2015a] stated that their SIF retrieval approach (based on GOSAT FTS) does not show a strong dependence on cloudiness. However, Guanter et al. [2015] reported undetectable thin clouds to be a source of SIF depletion through the atmosphere. Reduction of SIF within the far-red wavelength region is reported to be 15% for the simulation-based retrievals using cloud optical thickness of 5.0 at 550 nm. Frankenberg et al. [2012] also stated that even in moderate cloudiness, SIF signal can still be retrieved. Therefore, cloud filtering has a significant statistical influence on the retrieval averages [Joiner et al., 2016]. Among the recent studies using SCIAMACHY data to retrieve SIF (e.g. Köhler et al. [2015b] and Joiner et al. [2016]) 0.3 was the most stringent Cloud Fraction (CF) by which the results were filtered. Krijger et al. [2007] assessed the amount of cloud-free scenes given the area of the footprint of a sensor. Considering the footprint of SCIAMACHY in the selected channel (wavelength), the probability of having a cloud-free pixel is below 20%. Given these points, it is clear that optimum cloud filtering should be set to minimize the retrieval disturbance due to cloudiness as well as to prevent uncertainties due to sampling reduction.

The cloud fraction method used to cloud-mask the SIF retrievals in the framework of this study is MICROS (MerIs Cloud fRation fOr Sciamachy) [Schlundt et al., 2011].

To assess the sensitivity of the developed retrieval algorithm to cloudiness and selecting the optimum cloud filtering threshold, the effect of two different types of clouds have been modeled for a variety of atmospheric and surface scenarios. The following cloud types are chosen for this study:

1. thin semi-transparent ice clouds near the tropopause (e.g. cirrus clouds)

2. thick opaque water clouds in low-mid latitudes (e.g. stratus clouds)

These two categories have been selected based on their different yet influential and representative characteristics. Thin ice-clouds are hard to detect and therefore, the CF is of no use. Thicker water-clouds are mostly detectable and their fraction is of importance for cloud-filter application.

Thin ice clouds

Thin and semi-transparent clouds are difficult to detect by cloud fraction algorithms [Schlundt et al., 2011] and can easily be missed by the cloud filter methods. Therefore, there may be some SIF values retrieved over this (undetected) cloud coverage. However, assessing the impact of the Cloud Optical Thickness (COT) for thin clouds reveals the extent by which it is safe to have undetected thin clouds.

To have a rather realistic estimation of the satellite measurements different TOA radiances have been created using SCIATRAN based on COT values from 0.1 to 2.0 for high altitude ice clouds (located from 7.0 to 7.5 km above the ground). It has been assumed that for each scenario the whole scene is covered by thin homogeneous clouds (CF $= 1.0$) for all ice-cloud scenarios. The same SIF emission spectrum as before has been used simulating radiances. Due to the high reflectivity of the clouds in this spectral range, the larger the COT, the larger is the simulated radiance intensity $I^{+}(\lambda)$ due to larger reflection and scattering. To achieve more realistic simulations the following points were taken into account:

- Additional zero-offset values have been added to the modeled radiances which were produced realistically as functions of the average radiances (Eq. 3.18).
- Realistic random noise has been prepared for each simulated radiance according to the expected SNR and radiance intensities (Fig. 4.11)

Ultimately, the ε-fit has been conducted utilizing modeled radiances 10000 times (see section 4.3.2) for each cloud thickness scenario. The obtained ε values together with their standard deviations ($\pm\boldsymbol{\sigma}$) are plotted with respect to the average radiances, in Fig. 4.16. From this plot, one can see that thin clouds at high altitudes cause an underestimation in the ε retrieval due to their shielding effect. However, the difference between the true ε values and the mean retrieval remains within the $\pm\boldsymbol{\sigma}$ which the results are not altered significantly due to undetected thin clouds ($\sim$ COT up to 2.0).

Thick water clouds

Low water clouds are thicker and easier to detect. Thus, as long as they are thick enough to be detected, the CF by which they are filtered should be assessed. Given this, the optical thickness can be set to a fixed value while the CF is assessed. Accordingly, the relatively low COT of 6.0 is chosen to be fixed for this model study. Water clouds with COT of 6.0 are thick enough to be detected and documented by MICROS algorithm and optically thin enough to prevent strong shielding effect on SIF signal reaching TOA.

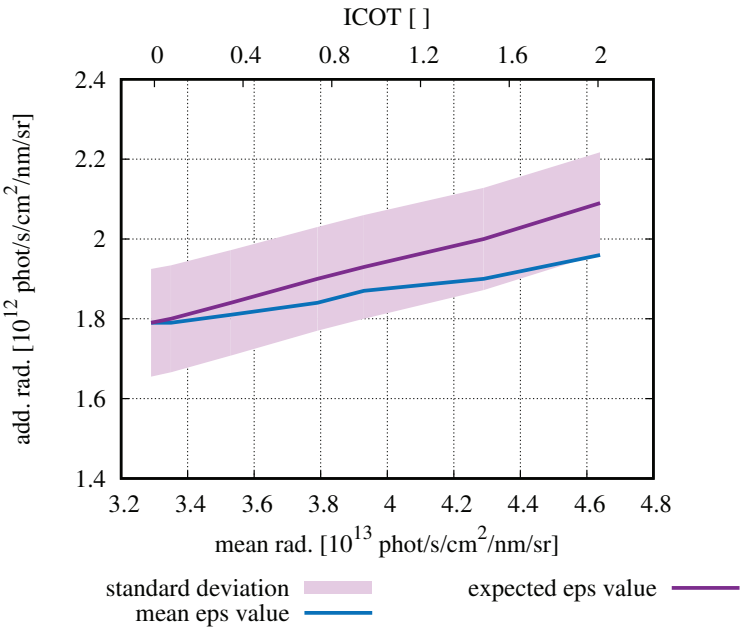

Figure 4.16: ε retrieval modeled at TOA over a scene covered by thin ice-clouds compared to the true ε values. The expected $\varepsilon = \varepsilon_a + \varepsilon_f$ is plotted versus mean radiance (in purple) with its standard deviation modeled based on realistic SNR values (in light purple). The retrieved ε values modeled for cloudy scenes are shown in dark blue. The retrieved ε curve has a smaller slope with respect to the true ε curve due to the shielding effect of clouds. The Ice Cloud Optical Thickness (ICOT) has been varied from zero (no clouds) to 2.0 (thin clouds) which can be missed by the cloud filter although the cloud fraction for all scenarios is assumed to be 1.0 (full coverage). The clouds are assumed to consist of ice and located between 7.0 to 7.5 km above the ground.

Therefore these characteristics are chosen to study the effect of CF on the ε retrieval. To simulate a set of realistic radiance scenarios the following are taken into account:

- Each radiance scenario is produced as a a linear combination of two independent simulated radiances which only differ based on the presence and absence of clouds in the modeled atmosphere.
- The two main simulated radiances which are used to prepare multiple CF conditions are first, a "clear sky" radiance modeled as $I^{+}(\lambda)$ and second, a "cloudy sky" radiance modeled for the similar condition but fully covered with clouds; $I_c^{+}(\lambda)$. The CF scenarios are created using Independent Pixel Approximation (IPA) [Marshak et al., 1995]:

$$I_F^{+}(\lambda, \mathrm{CF}) = \mathrm{CF}\, I_c^{+}(\lambda) + (1 - \mathrm{CF})\, I^{+}(\lambda)\,, \tag{4.3}$$

  in which $I_F^{+}(\lambda, \mathrm{CF})$ is the radiance simulated for a certain CF.
- The cloud setup for "cloudy sky" is the COT of 6.0 for clouds consisting out of water droplets, located from 2.5 to 3.5 km above the ground.
- The CF for water clouds has been varied from 0.0 for 100%, clear sky to 1.0 for 100% cloudy sky in steps of 10%.
- The SIF emission signal is present while producing all scenarios and its magnitude is unchanged.
- One can see from the model simulations that increasing the cloud fraction leads to the larger radiance intensity. Additional zero-offset values have been added to the modeled radiances which were produced realistically as functions of the average radiances (Eq. 3.18).
- Realistic random noise has been prepared for each simulated radiance according to the expected SNR ($\sim$4000 to 6000 depending on the radiance magnitude) and radiance intensities.

Accordingly, the ε-fit has been conducted utilizing the modeled radiances 10000 times (see section 4.3.2) for each COT scenario. The obtained ε values together with their standard deviations ($\pm\boldsymbol{\sigma}$) are plotted with respect to the average radiances, in Fig. 4.17. One can see that even for clouds with sufficient optical thickness, detectable by the space-borne instruments, CFs more than 40% lead to an underestimation of the retrieved ε values exceeding the first $\boldsymbol{\sigma}$. This confirms the findings by Joiner et al.

[2013a, 2016] and Köhler et al. [2015a,b]. However, it is worth to mention that a COT of 6.0 is relatively small and in this model study (as well as the studies conducted by Joiner et al. [2012, 2013a, 2016] and Köhler et al. [2015a,b]), the effect of the inhomogeneity of the clouds, the horizontal radiative transfer and the spectral absorption by the cloud water droplets are not taken into account. Although H_2O absorption is negligible in this wavelength window, its effect on the ε retrieval can increase in very high concentrations e.g. as in clouds (see end of the section 4.2). Additionally, as clouds can increase the brightness of the measured scene leading to an increased level of mean radiance (see Fig. 3.4), the ε_a retrievals over clouds have larger statistical uncertainties.

Opposite to the previous studies mentioned above, a more stringent cloud filter for CF > 5% is applied in this work. Although the ε-fit results will not be affected by cloud brightness/shielding effect, the impact of water vapor inside clouds and their vicinity can deteriorate the fit results. However, this impact is not yet quantified. Therefore, during the process, measurements contaminated by clouds were avoided when at all possible. The reason why PCA-based methods (taken by e.g. Joiner et al. [2013a]) seem to be rather insensitive to clouds might be due to the attribution of one or more PCs to this effects based on the selection of the underlying statistical ensembles.

To summarize the model study showed a clear feasibility of the method to retrieve SIF at TOA and the error assumptions due to uncertainties in measurements showed promising retrieval results. Numerical studies combining the uncertainties due to RRS, SNR and gaseous absorption showed the net error of ε-fit does not exceed 25% of the true value. However, although simulations did not demonstrate any significant distortion of the retrieval results due to cloudiness, the actual effect of clouds on the retrieval cannot be estimated from model-based studies.

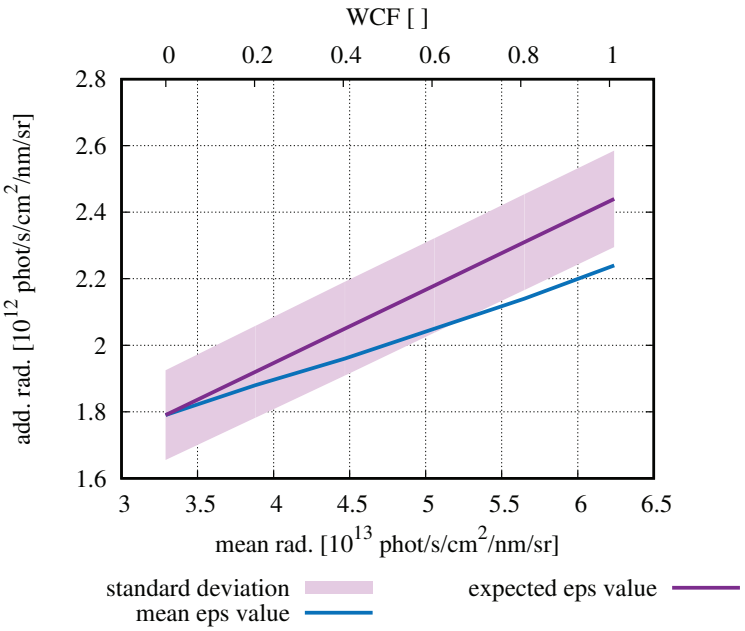

Figure 4.17: The expected $\varepsilon = \varepsilon_a + \varepsilon_f$ at TOA versus mean radiance (purple) together with its standard deviation expected based on SNR assumptions (light purple). The retrieved ε values are shown in blue. The retrieved ε curve has a smaller slope with respect to the true ε curve due to the shielding effect of clouds. The Water Cloud Fraction (WCF) has been varied from zero (no clouds) to 1.0 (full coverage) and the Cloud Optical Thickness (COT) is 6.0 (relatively thin but visible to the MICROS cloud data base). The clouds consist out of water and located between 2.5 to 3.5 km above the ground.

Part III

Results and Further Developments

Chapter 5

Retrieval Results and Comparison

In the present chapter, the globally retrieved solar-induced vegetation fluorescence from SCIAMACHY is presented and compared to the SIF results provided by NASA [Joiner, 2014] (section 5.2 and 5.3). An essential pre-requisite of the retrieval is to establish a data-base, which is adequately substantial to cover the variation of fluorescence reference spectra for the possible measurement conditions (e.g. geometry, AOD). Therefore, the first section of this chapter is to describe this data-base and its development progress.

Since SIF is a by-product of photosynthesis, on large spatial and temporal scales, it follows the spatial patterns and temporal dynamics of vegetation. Therefore, in section 5.4 the seasonality of global vegetation is compared to an averaged SIF retrieval for each season over 10 years of data.

Recent studies showed that SIF can provide valuable information of photosynthetic efficiency [Rossini et al., 2015]. Frankenberg et al. [2011b] showed strong correlation between SIF and model-based GPP. Guanter et al. [2014] also demonstrated that the satellite-based SIF retrievals are directly related to the GPP of crop- and grass-lands. Likewise, it has been shown that the changes in vegetation due to environmental stress (e.g. drought) can be seen from SIF [Daumard et al., 2010] even though the NDVI (section 2.3) and chlorophyll content of the leaves may remain unchanged. These findings clarify that SIF is more informative on photosynthesis and plant's health than the vegetation indices. Therefore, the fifth section of this chapter is dedicated to the relationship between SIF and photosynthesis. In order to observe the correlation between SIF and photosynthetic efficiency, the APAR and GPP, measured locally, are compared to the fluorescence values on regional scale.

Additionally the application of the retrieval method on GOME-2 instrument's measurements is discussed in the final part.

As explained in section 3.1.2, the SIF emission spectrum is retrieved by using Eq. 3.21 as mean fluorescence emission within the 748.5 - 753 nm window, $\bar{\mathcal{F}}'_b$. This is a direct measure of the fluorescence emission intensity at TOC level in mW m^{-2} sr^{-1} nm^{-1}.

In contrast to the retrieval of the ε-fit where the minimization problem (Eq. 3.16) can be solved using solely measured radiance and irradiance spectra, retrieving the TOC fluorescence signal requires the proper selection of a FR spectrum to solve the minimization problem given by Eq. 3.14. Therefore, a large set of FR spectra (also referred to as the fluorescence OD) have been prepared which represents the variation of $F(\lambda)$ values due to different environmental and observational scenarios.

5.1 The reference spectrum data-base

As each measurement from the satellite is taken under different conditions (defined by measurement geometry, surface reflectance and AOD) the used FR spectrum, being the quantity describing the net effect of SIF on the radiance reaching TOA, needs to be selected appropriately for utilization in the Eq. 3.14. For this purpose, a collection of prescribed scenarios is developed based on the most dominant measurement parameters on $F(\lambda)$.

As mentioned in section 4.3.3, FR does not strongly depend on the AOD and A. The surface reflectance has been taken from the database provided by Koelemeijer et al. [2003] (and the corresponding files from the website: http://www.temis.nl). Likewise, the AOD given by Kinne et al. [2013] (and personal correspondence with S. Kinne) has been used as the AOD database to simulate the representative FR spectra.

Additionally, the determination of an a priori fluorescence emission spectrum at TOC ($\bar{\mathcal{F}}_b$) is necessary. However, the selection of an a priori fluorescence emission spectrum has comparatively small impact on the outcome FR as shown in the section 4.3.1 and stated also by e.g. Joiner et al. [2013a], Guanter et al. [2013]. Therefore, in the framework of this study, the $\bar{\mathcal{F}}_b$ has been fixed to a single emission spectrum which is selected through FluorMODgui [Zarco-Tejada et al., 2006] for velvet grass (*Holcus lanatus*) as measured and provided by Rascher et al. [2009]. For each measurement scenario the process of simulating $F(\lambda)$ is as follows:

$I^+(\lambda)$ is obtained implementing the chosen $\bar{\mathcal{F}}_b$ as an emission spectrum at TOC (see section 2.2.4). The propagation of SIF in addition to the upwelling reflected radiance has been modeled through the atmosphere considering its interaction with aerosol particles as well as air molecules. In the same manner, $I^-(\lambda)$ has also been modeled at

Surface reflection (A)	0 - 0.2, step 0.02 0.2 - 0.3, step 0.01 0.3 - 0.5, step 0.02 0.52, 0.54, 0.58, 0.60, 0.65, 0.70, 0.75, 0.80, 0.85, 0.90, 1.00
Solar zenith angle (ϑ_0) [degrees]	0, 10, 20, 30, 40, 60, 80
Relative azimuth angle ($\varphi - \varphi_0$) [degree]	0, 30, 60, 90, 120, 150, 180
Viewing zenith angle (ϑ) [degrees]	0, 10, 15, 20, 25, 30, 35, 40
Aerosol Optical Depth (AOD) []	0.01, 0.02, 0.04, 0.08, 0.10, 0.20, 0.40, 0.60, 0.80, 1.00, 1.50

Table 5.1: The values of surface reflection, solar zenith angle, relative azimuth angle, viewing azimuth angle and AOD used for creation of the FR TOA radiance scenarios using SCIATRAN. The values are selected based on the range variations expected over vegetated and non-vegetated areas.

TOA excluding SIF emission. Finally, FR is calculated according to Eq. 4.2.

In order to cover the full range of possible scenarios when using satellite-borne measurements, a set of FR spectra (more than 170.000 scenarios) have been calculated at high spectral resolution, varying observation/illumination geometries, surface reflectance spectra and AOD (Table 5.1). The spectra were created for global observation conditions of all relevant spectrometers in orbit (or with available data) with needed spectral bands such as GOME, GOME-2 and SCIAMACHY. The FR spectra are created by successive runs of SCIATRAN model at spectral resolution of 0.01 nm and are afterwards convolved to the required instrumental resolution using the appropriate slit function of the instrument (in case of SCIAMACHY a Gaussian slit function with full width at half maximum of $\sim$ 0.48 nm [Gottwald and Bovensmann, 2011]).

The resulted FR spectra are utilized in a Look-Up Table (LUT) setup, providing the most adequate FR for each satellite measurement spectrum $I_m(\lambda)$ to minimize the retrieval uncertainties due to atmospheric/measurement properties when solving Eq. 3.14.

The sensitivity studies on cloudiness and its influence on SIF retrieval provided in section 4.3.5 suggest that cloud "contamination" disturbs SIF retrieval to a certain extend. However, since modeled clouds were not comprehensively summarizing all of their effects, a more stringent cloud filter (than e.g. Joiner et al. [2013a], Köhler et al.

[2015b]) has been implemented (see section 4.3.5).

5.2 Far-red SIF from SCIAMACHY measurements

The level 1 SCIAMACHY measurements have been utilized to perform seasonally resolved SIF signal at TOC for all available years (2003-2012), gridded to 80 arc minutes (130 km at equator). Results are depicted in a color-coded fashion in Fig. 5.1. This SIF dataset will be referred to as "IUP-data" henceforth in this dissertation. The seasonal features for global distribution of SIF are consistent with the logical expectation: Larger values of SIF are observed over densely vegetated areas and a SIF "belt" with evaluated SIF values is spanning from central Europe over Siberia to Eastern China (which is more pronounced during summer as presented in section 5.4). This is also consistent with the results shown recently by Joiner et al. [2013a] and Guanter et al. [2013, 2014]. The annual average of fluorescence also shows higher values over the tropical regions which do not show seasonality.

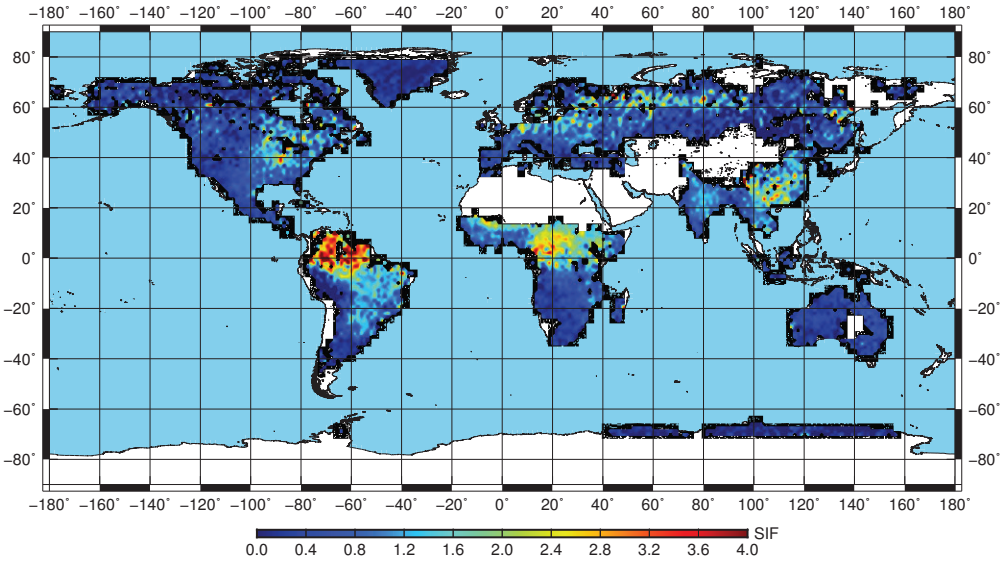

Figure 5.1: The annually averaged SIF retrieval at TOC for years 2003-2012 of SCIAMACHY measurements for ∼ 750 nm

The spectral wavelength region selected for this study is almost free of gaseous absorption, which caused a relatively low spatial resolution. Originally each retrieval result is covering an area of 240 × 30 km^2. Especially, near the coasts the results are therefore likely to be influenced by water, causing the retrieval to be diluted as a result of wrong ε_a estimation as well as having no contribution from ε_f over water.

Moreover, removing the cloudy pixels leads to a poor sampling which can cause the SIF average values to be less reliable. Accordingly, the SIF retrievals over the Indonesian Archipelago are an example of the results to be lower than expected near the shores.

Another example is the large SIF variability expected over managed agricultural areas in Europe which cannot be well resolved at this spatial resolution. However, the large and well pronounced US "corn and soybean belt" (Fig. 5.2) is qualitatively in accordance with studies using finer spatial signatures (e.g. Joiner et al. [2013a], Guanter et al. [2014]).

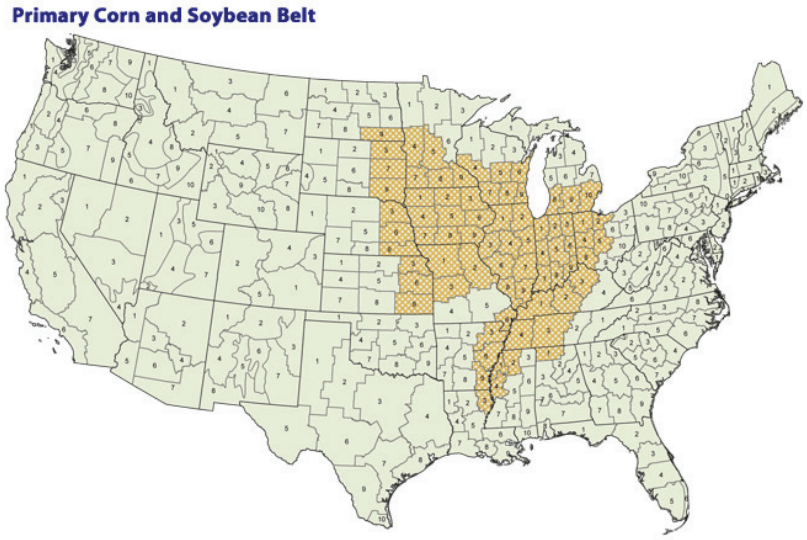

Figure 5.2: The so-called corn and soy belt of the US according to NOAA [2015].

5.3 Comparison with NASA fluorescence data

Joiner et al. provided access to their SIF data, derived from GOME-2 measurements using the approach previously published in Joiner et al. [2013a] but using an optimized spectral window defined in Joiner et al. [2013b]. This dataset is henceforth called GSFC-data, and is labeled as "version 25" (v25). Recently "version 26" (v26) has been also released. Specifically, when the spectral window for GSFC-data (v25) was compared with the previously published version of Joiner et al. (labeled as "version 14"), it had been set to 734-758 nm, thereby avoiding the O_2-band and strong water vapor absorption lines. The number of principal components used in V14 (25 PCs) is also reduced to 12 PCs in v25. The latest version of GSFC-data which was publicly accessible during the course of this work is v26. The comparison of IUP-data to

GSFC-data of version 25 can be found in Khosravi et al. [2015].

To compare the SIF retrievals to the GSFC-data (v26), the GSFC-data is binned to the same grid as IUP-data (80 arc minutes). In Fig. 5.3 the resultant globally mapped data sets for the year 2009 are presented. SCIAMACHY achieves global coverage in its nadir-mode within six days. In comparison, GOME-2 achieves global coverage in approximately 1.5 day. As a result, the SCIAMACHY data set appears somewhat more patchy.

The US-corn and soybean belt or the rain forests (and surroundings) are identified by both datasets. Some of the differences are attributable to the different spatial resolution and local overpass time. Metop, the satellite carrying GOME-2, has an equator overpass time of 9:30h, whereas that of ENVISAT carrying SCIAMACHY is 30 minutes later (see Fig.3.9).

Recall that the spectral window in which the fluorescence results of IUP-data achieved is between 748.5 and 753 nm. However, for GSFC (v25) data the average fluorescence at 740 nm is reported. Respectively, a difference between these two sets of data is expected. The numerical studies based on the RTM and the SIF reference spectrum from Rascher et al. [2009] suggest that SIF at 740 nm is $\sim 10\%$ larger than the 751 nm. These mapping results are adjusted accordingly in Fig. 5.3. Comparisons with the originally published GSFC data sets (version 14) showed closer agreement, especially over regions where the IUP-data tends to show higher SIF values than the current GSFC data (v26). It is important to notice that changing the retrieval window in v25 caused a significant decrease in the retrieved SIF values [Köhler et al., 2015b].

To have a more reliable statistical view, a gridcell-by-gridcell comparison between the two data sets have been performed. The resulting scatter plot (Fig. 5.3, below) depicts only those gridcell results where both IUP data sets have valid values. As can be clearly seen, GSFC-data values are confined within a narrow data interval up to 2 mW m^{-2} $sr^{-1}nm^{-1}$ while the IUP-data can amount up to 4 mW m^{-2} sr^{-1} nm^{-1}. The results are filtered for SZA$>$ 80 degrees and NDVI.

Personal correspondence with the first author of [Joiner et al., 2013b] clarified that the used data (v26) is considered to be of higher quality than the previous versions and there have been several changes since the published version 14 by Joiner et al. [2013a]. Furthermore, according to the author, version v26 uses an Earth spectrum as a reference, instead of an extra-terrestrial solar spectrum needed for a reference based retrieval (as used in Joiner et al. [2012]), which can together with the implemented principle components, mitigate the effects of the zero-level offset as compared with the use of a solar spectrum. However, in the recent publication by Joiner et al. [2016], they applied an additional zero-offset correction to their retrieved SIF values although the

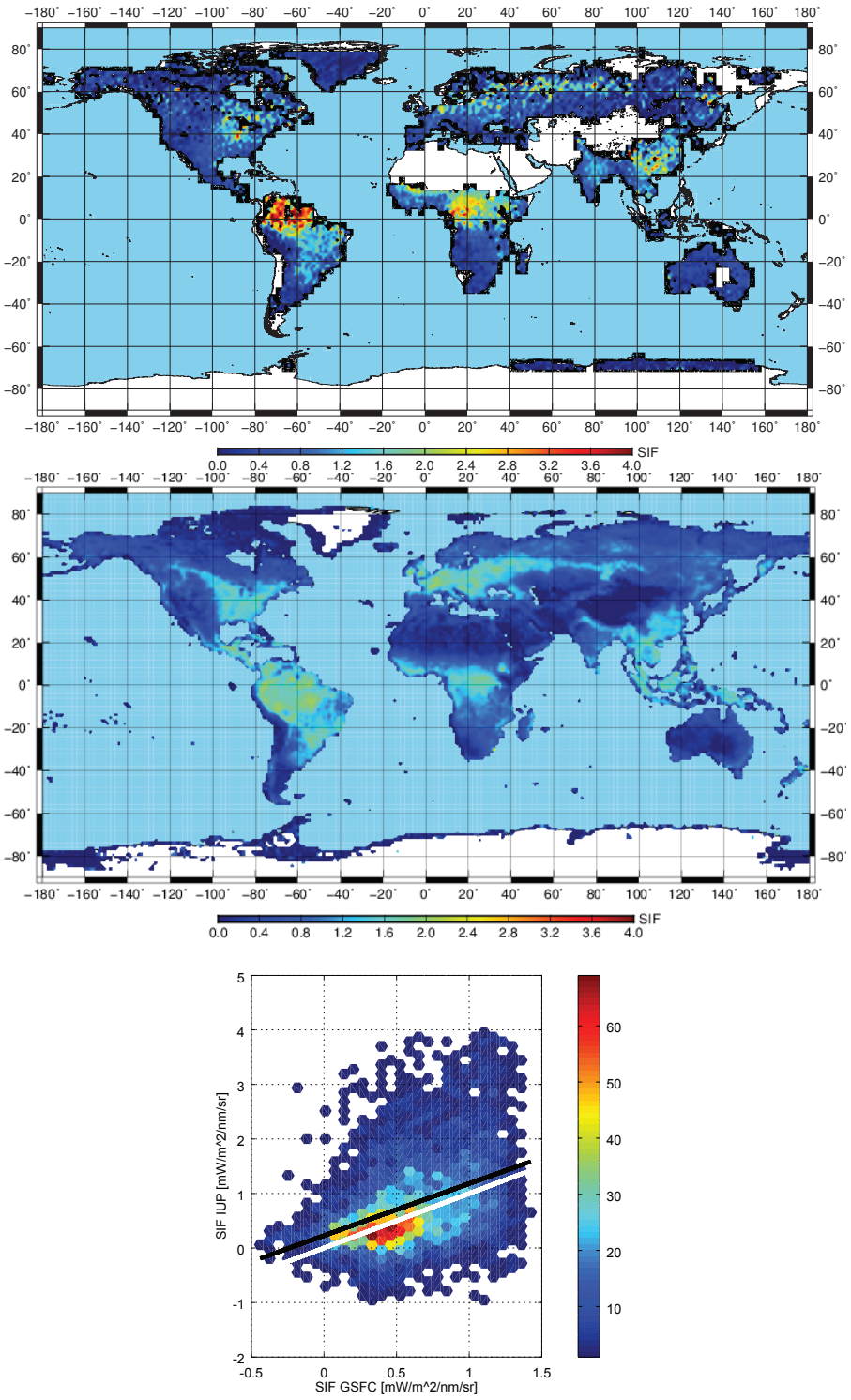

Figure 5.3: Global values of fluorescent emission strength in [mW m^{-2} sr^{-1} nm^{-1}] at the top of canopy layer and at TOA for the year 2009; Upper: results of this work, Middle: as reported by Joiner et al. [2013b] (v26, NASA), Bottom: a scatter (density) plot of both data sets with underlying color code (from dark red: frequent occurrence to dark blue: less occurrences).

corresponding approach they took was principal component analysis as before. This raises the question of whether this could lead to an overcompensation for the zero-offset effect in the recently published datasets.

An important aspect in the retrieved SIF within the framework of this dissertation and e.g. GSFC-data is the sampling and statistics which has been discussed by many authors e.g. [Joiner et al., 2012, 2013a, 2016, Guanter et al., 2013, 2014, Köhler et al., 2015b, and others]. Another source of the difference between both data sets might also be traced back to sampling of IUP-data over certain areas. Due to the the relatively low spatial resolution of SCIAMACHY measurements within the chosen wavelength region, especially over areas where persistent clouds obstruct the view to the canopy layer for longer time-spans, poor sampling can lower the accuracy of the retrieval. For instance in Venezuela (or generally Northern parts of South America) such conditions lead to gridded (annual averaged) values which were made up of five individual observations only, while in other less cloudy regions (and time spans) easily 30 or more individual observations were used for averaging one year of data. Accordingly, the spatial resolution is related to this problem, as also the likeliness of cloud appearance is clearly higher for larger ground pixels.

The relationship between SIF and the photosynthetic activity of plants has been discussed in section 2.1.4. Eq. 2.8 shows how fluorescence emission is related to carbon uptake by plants. The growing season within a region could be observed through an increase in SIF emission, as an increase in the leaf density can be translated to an increase of Chl molecules which absorb light and emit fluorescence. In a similar manner, winter for deciduous vegetation is observed through the lack of fluorescence emission due to the absence of Chl receptors. Thus, the SIF values retrieved from SCIAMACHY far-red measurements are assessed with respect to the large scale (global) vegetation seasonal trends.

5.4 Vegetation seasonality and SIF

As SIF is generated during the photosynthetic process (see section 2.1.4), temporal variation of the global vegetation can be observed through the seasonal variation of SIF [Joiner et al., 2013b].

The retrieved and gridded SIF values between the years 2003 and 2012 are seasonally averaged and plotted in Fig. 5.4. Winter, spring, summer and autumn are shown sequentially from top to bottom. Winter in northern hemisphere is associated with significant decrease in the number of leaves, in particular for deciduous forests.This can be observed from little to no SIF emission in the northern hemisphere during winter. At

the same time, southern hemisphere shows stronger fluorescence emission. During the spring months, vegetation growth in the northern hemisphere is visible by an increase in SIF emission in the areas such as the corn-belt in the US as well as agricultural areas and forests in Europe and China. Consequently, from June to August, the SIF emission is on average at its maximum. The SIF signal declines again during autumn together with vegetation density and potosynthetic activity in northern hemisphere.

Comparing the seasonal maps to the GSFC-data, qualitative similarities can be seen showing similar trends (Fig. 5.3). However, the IUP-data is significantly larger as discussed in the previous chapter.

Köhler et al. [2015b] presented retrieved SIF from SCIAMACHY and GOME-2 instruments within the far-red spectral region. Although the retrieved data are not publicly accessible, values of up to 4 mW m^{-2} sr^{-1} nm^{-1} can be seen in their maps. They provided a linear relationship between their results and the GSFC-data in order to produce maps which are visually better comparable. Their approach may not be scientifically representative but makes it possible to indirectly compare the mapped IUP-data to the SCIAMACHY SIF retrievals by Köhler et al. [2015b]. The resulted maps are shown in Figure 5.5 and Figure 5.6. The main purpose of these illustrations is to show qualitative similarities, although there is not much of scientific value in such comparison. However, since the results from Köhler et al. [2015b] (obtained from both SCIAMACHY and GOME-2 instruments) are at least 50% larger than the GSFC-data (from GOME-2), the necessity for reliable validation sources is clear [Köhler et al., 2015b].

Bauerle et al. [2012] showed that the photoperiod[1] is a driver of variation in leaf activity and photosynthesis in addition to temperature (e.g. before and after summer solstice). It has been shown that taking this effect into account can improve the predictions of seasonal variations in atmospheric CO_2. Therefore, the relationship between space-borne measured SIF with the photo-biochemical properties of the canopy is of a significant interest. For instance, Guanter et al. [2014] could show that high photosynthetic rates for croplands are better observed by SIF than vegetation indices. Additionally, they stated that comparing remotely sensed SIF with the seasonality of GPP and APAR shows the potential of fluorescence to be utilized in vegetation and climate models, improving their accuracy.

[1] the time period within which an organism e.g. plant is exposed to illumination

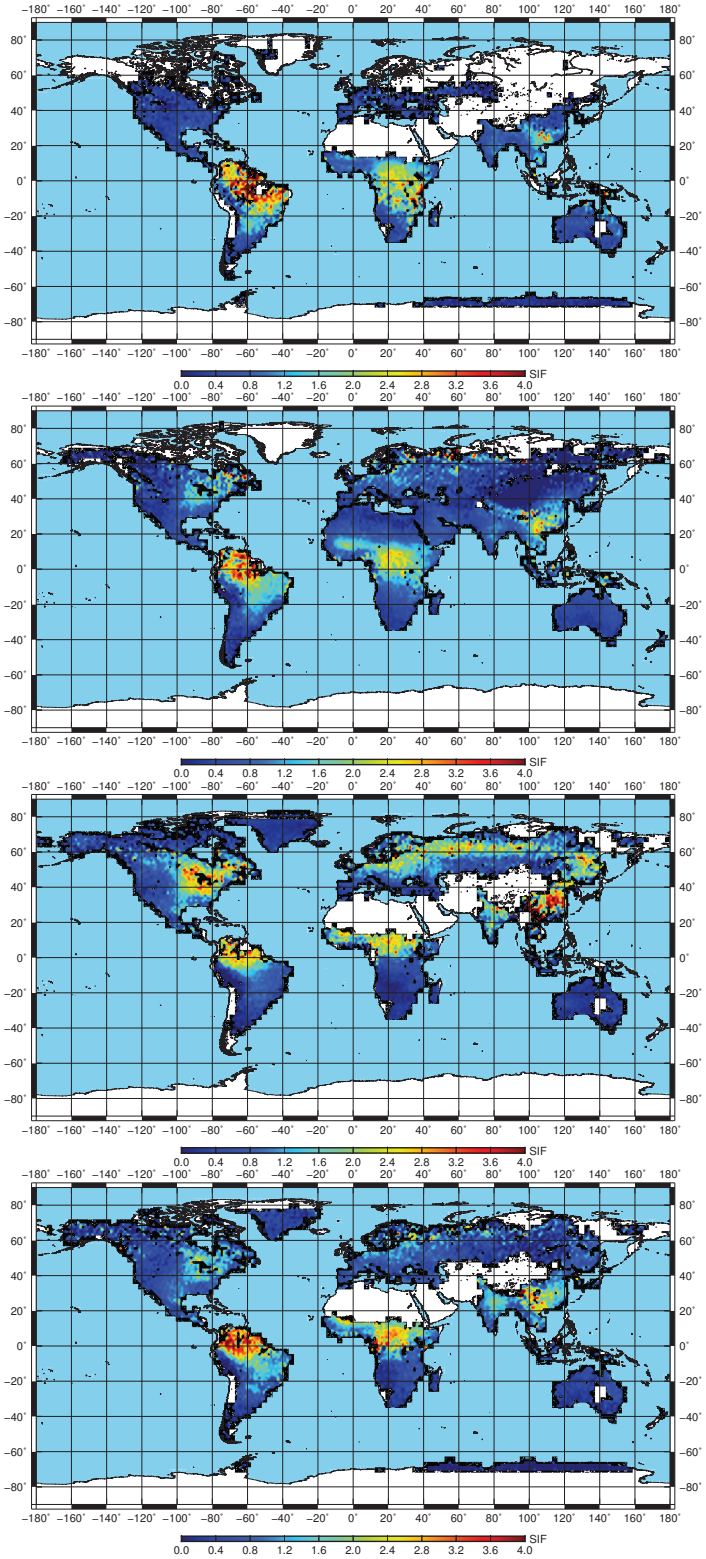

Figure 5.4: Global values of fluorescent emission strength in mW m^{-2} sr^{-1} nm^{-1} at the top of canopy layer as seen from SCIAMACHY data; (1. upper) For Northern winter (DJF); (2. upper) For spring (MAM); (3. lower) For summer (JJA) and (bottom) For autumn (SON) months. The data is from the years 2003 - 2012 and is gridded to 80 arc minutes.

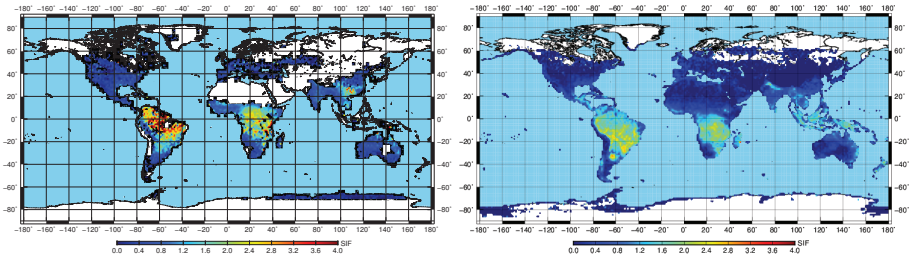

Figure 5.5: A comparison between the SIF retrieved for the winter months (December, January and February) averaged between 2003 to 2012 from SCIAMACHY (left) and the GSFC-data (v26) for the year 2009, scaled according to Köhler et al. [2015b]

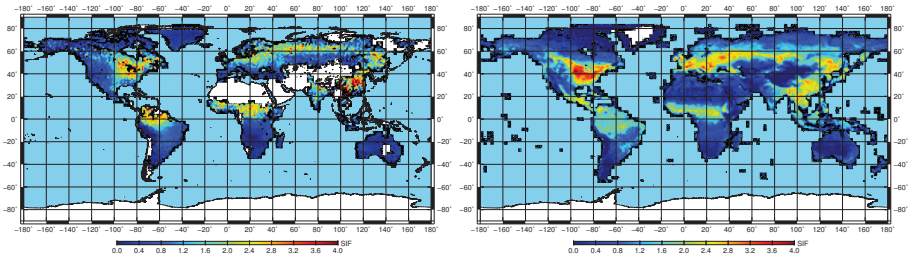

Figure 5.6: A comparison between SIF retrieved for the summer months (June, July, August) averaged between 2003 to 2012 from SCIAMACHY (left) and the GSFC-data (v26) for the year 2009, scaled according to Köhler et al. [2015b]

5.5 SIF correlation with bio-geochemical properties

As explained in section 2.1.4 SIF shows linear dependency on GPP. Considering the effect of the photoperiod on the carbon-uptake by vegetation, the correlation between SIF, APAR and GPP has been studied so far by e.g. Louis et al. [2005], Amorós-López et al. [2008], Van der Tol et al. [2009a], Guanter et al. [2014] and Joiner et al. [2014]. Utilizing SIF retrievals to estimate GPP, Guanter et al. [2014] obtained 50-75% larger results as from state-of-the-art carbon cycle models, especially in the regions corresponding to the US corn belt and the Indo-Gangetic plain. The SIF values retrieved within the framework of this thesis from SCIAMACHY far-red measurements over the latter region are not as well pronounced which might also be due to the comparatively low spatial resolution used here. However, the values provided by Guanter et al. [2014] had spatial resolution of the GOME-2 (80 km$\times$ 40 km^2). Accordingly, a benchmark comparison between the retrieved SIF and locally measured APAR and GPP, has been done in order to investigate the information content of SIF for these parameters.

The IUP-data and its temporal variation has been compared to GPP and APAR measured at eddy covariance flux towers (see section 2.1.2) such as those from FLUXNET. This is a global network of eddy covariance measurement stations, providing direct measures of CO_2, water vapor and energy between the atmosphere and the canopy from more than 800 measurement towers globally. The stations selected for this study were from AmeriFlux[2]. The chosen stations are listed in Table 5.2. The quality-controlled GPP and APAR data (for each half an hour) between 2007 to 2012 have been chosen for the purpose of this study and are hereafter referred to as *flux-tower data*. Due to the footprint size and the local overpass time of SCIAMACHY, co-locating the SCIAMACHY ground pixels and flux-towers is challenging. For this reason, only those pixels have been selected, for which the centers are displaced by a maximum distance of 100 km from the measurement tower. Eventually, the chosen SIF retrievals are filtered with respect to clouds and averaged over each month. The local overpass time for SCIAMACHY is 10:00. Consequently, for each day the mean APAR and GPP between 9:00 and 11:00 are calculated and utilized to obtain monthly average values.

Due to the different vegetation types of the stations US-KUT and US-Ne, they have been assessed separately. The temporal variations of the retrieved SIF, APAR and GPP from flux-towers are presented in Fig. 5.8. One can clearly see that the overall pattern of the curves represents the seasonal variation of the plants. From almost no fluorescence in winter, the emission increases to the mid-summer months and declines again from

[2]a network of measurement stations for ecosystem fluxes in North, Central and South America (http://ameriflux.lbl.gov/about/about-ameriflux/)

Site Code	Station name	Coordinates	Specifications
US-Ne1	Mead-irrigated continuous maize site	41.165, -96.476	maize-soybean irrigated with a center pivot system.
US-Ne2	Mead-irrigated maize-soybean rotation site	41.165, -96.470	maize-soybean irrigated with a center pivot system.
US-Ne3	Mead-rainfed maize-soybean rotation site	41.180, -96.440	maize-soybean but relies on rainfall
US-KUT	KUOM Turfgrass Field	44.995, -93.486	A 1.5 ha turf-grass field in suburb area

Table 5.2: The chosen FLUXNET stations providing APAR andGPP variation from and to the canopy. US-Ne1, 2 and 3 are three stations which are located within 1.6 km from each other at the University of Nebraska Agricultural Research and Development Center. The US-KUT station, is located in a turf-grass field in a first-ring suburb of Minneapolis-Saint Paul, Minnesota [https://fluxnet.ornl.gov/]

August-September till February. Since the US-Ne stations are located in agricultural fields of soy and maize, the growing season lasts till end of summer and there is only one maximum for the GPP and APAR annually. It can be seen that SIF results follow this pattern as well. Although the spatial footprint of SCIAMACHY has significantly larger coverage and is not limited to these specific fields only, located within the US corn-belt, the area is assumed to be dominated by the same species. Fig. 5.7 shows the land cover map [Bontemps et al., 2011] specifying different biomes with a high spatial resolution of 300 m. The land cover within the so-called US corn-maize belt is visibly dominated by agricultural fields and grasslands. Therefore, the region is assumed to be a relatively homogeneous combination of managed and cultivated regions for the corresponding SIF retrievals.

From Fig. 5.8 one can see that the annual curves of SIF retrieval results (from 2008 to 2011) have larger width than the curves for GPP and APAR (not only in the growing season). This implies that SIF emission is not limited to growing seasons. It has also been noticed that the relatively small values of GPP and APAR are followed by slightly larger SIF emission and vice versa. However, due to the small sampling of SIF measurements for the limited temporal and spatial intervals, this should not be over-interpreted.

The US-KUT flux tower station, provides GPP and APAR measures over a rain-fed

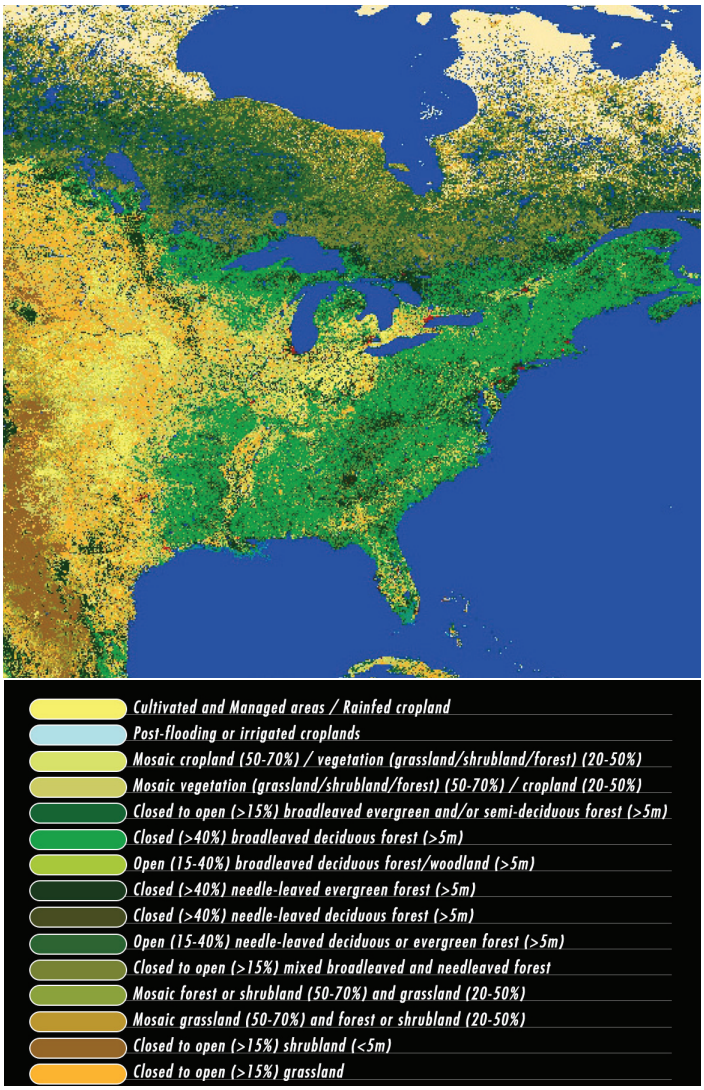

Figure 5.7: The GlobCover-2009 map from ESA [Bontemps et al., 2011], with a spatial resolution of 300 m. The land-cover composition of the so-called US corn belt is dominated by cultivated and managed areas together with dense to coarse grasslands.

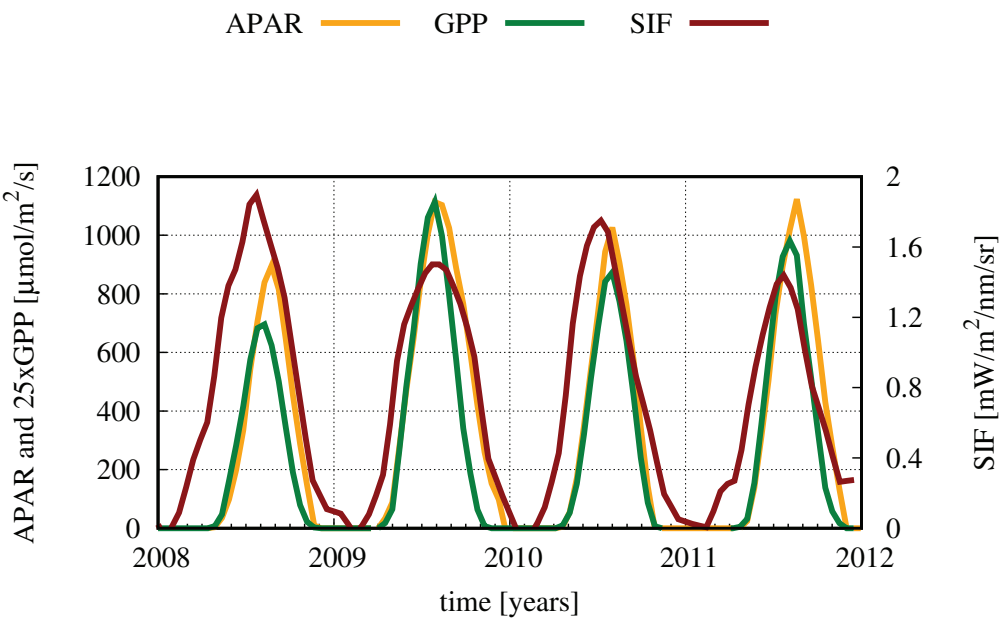

Figure 5.8: The monthly averaged APAR and GPP from the US-Ne1, 2 and 3 flux tower stations together with the monthly averaged SIF values retrieved from SCIAMACHY measurements co-located with the flux towers. The results are plotted for years 2008 to 2012.

grass-field. One can see from Fig. 5.9 that unlike APAR, the GPP for this region has two maxima in late spring and early autumn during the years 2007 and 2008. As the turf-grass field around this station is rain-fed, the daily precipitation for both years are also presented in Fig. 5.10. GPP has a close correlation with precipitation. SIF also shows a clear dependence on GPP even though the influence of APAR on it cannot be neglected. Generally speaking, an increase in GPP can be observed by an increase in SIF although monthly averaged SIF appears to be more stable during the months in which GPP declines but APAR stays high due to the presence of green leaves (e.g. mid-summer time). Zhang et al. [2016b] conducted a model study on the relationship between SIF and the GPP, concluding that the linearity between SIF and GPP is regulated by APAR which shows good agreement with the outcome of the current study.

Again, it is worth mentioning that the SIF values utilized for this comparison are from averaging over SIF signals of several species (inhomogeneity of the canopy) and the sampling number is small. However, the importance of this study is that SIF retrieved over these stations show different behaviors closely related to their GPP and APAR variation as stated by e.g. Joiner [2014], Guanter et al. [2014]. According to Damm et al. [2015], the correlation between SIF and GPP depends on the species and should be stronger for croplands than grasslands. However, a thorough analysis of such

dependences requires better spatial sampling.

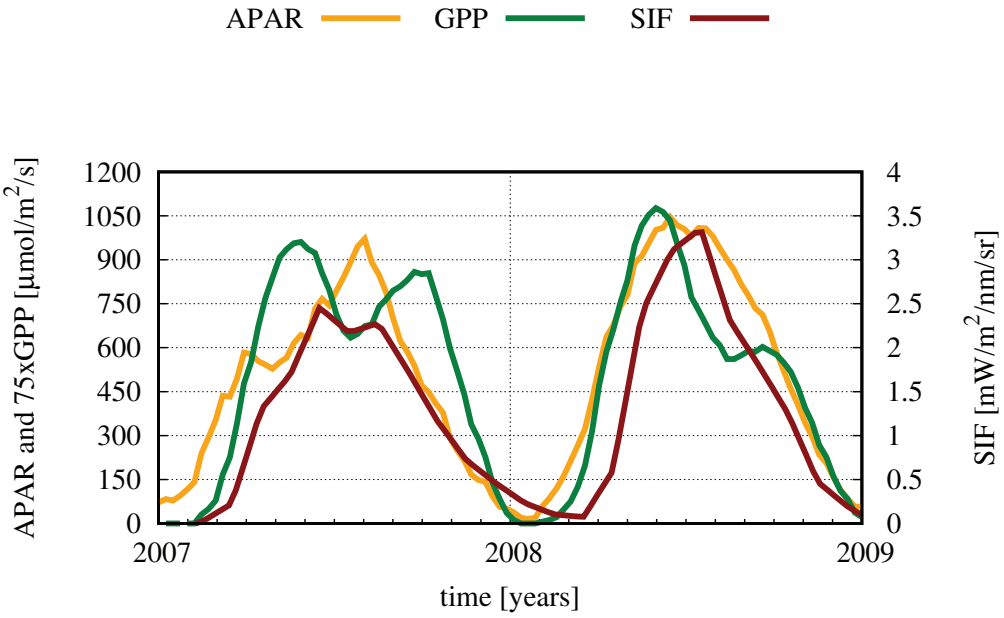

Figure 5.9: Monthly averaged APAR and GPP from US-KUT flux tower station together with the monthly averaged SIF values retrieved from SCIAMACHY measurements co-located with the flux tower station. The results are plotted for years 2007 to 2009.

The approach presented here is of generic nature and can thus be applied to other data sets. Theoretically, the retrieval method proposed in this dissertation is applicable on other hyper-spectral space borne instruments with a fair spectral resolution which can detect the infilling of the solar Fraunhofer lines. Therefore, the method is applied to GOME-2 level 1 data, as the instrument has a better spatial resolution, in the wavelength range needed, and better coverage, since this instrument is operated in nadir mode only, opposite to SCIAMACHY.

5.6 Application of the method to GOME-2 data

Joiner et al. [2013a], Wolanin et al. [2015] and Joiner et al. [2016] have provided measurements of the solar-induced fluorescence over land (and ocean), using the GOME-2. According to Köhler et al. [2015b] the zero-offset effect for GOME-2 can be significantly larger than for SCIAMACHY. However, applying the minimization Eq. 3.16 on the TOA radiances measured by GOME-2 in the far-red window over the non-vegetated regions shown in Fig. 4.1, did not lead to larger ε_a values comparing to SCIAMACHY results. As it is shown in Fig. 5.11, although the obtained ε_a values for GOME-2 have

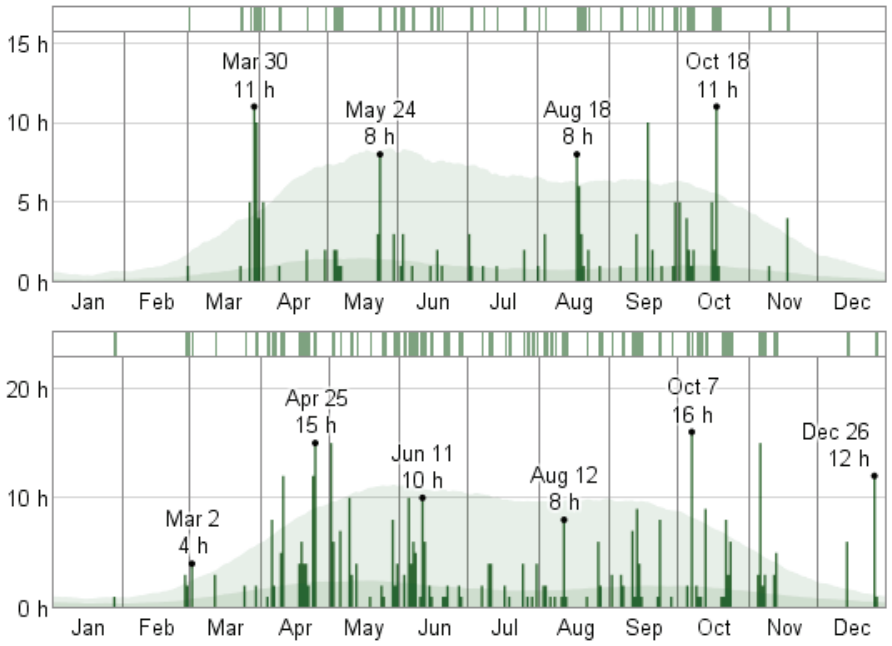

Figure 5.10: The daily number of hourly observed liquid precipitation reports during the years 2007 (top) and 2008 (bottom). The shaded areas represent the climate normals and the bars at the top of the graph indicates the presence of liquid precipitation reported that day. [Weatherspark]

significantly larger standard deviation ($\boldsymbol{\sigma}$), the fitted $\hat{\varepsilon}_a$ curve (according to Eq. 3.18) shows smaller slope than typical $\hat{\varepsilon}_a$ curves for SCIAMACHY data. Therefore, the "larger" zero-offset found by Köhler et al. [2015b] could be due to larger spectral noise in GOME-2 measurements with respect to SCIAMACHY.

Bearing in mind that the typical SIF values within the selected far-red spectral window are $\sim 10^{12}$ photons s^{-1} cm^2 nm^{-1} sr^{-1}, one can see from Fig. 5.11, that the standard deviation of the fitted $\hat{\varepsilon}_a$ curve is from the same order of magnitude as the typical SIF values. The highly scattered results of the ε-fit for GOME-2 emphasizes on the importance of SNR and spectral calibration for an instrument being utilized for SIF retrieval. The mapped SIF retrievals provided by Wolanin et al. [2015] also shows higher uncertainties for GOME-2 than SCIAMACHY. Given these points, application of the retrieval method on GOME-2 measurements needs further investigations.

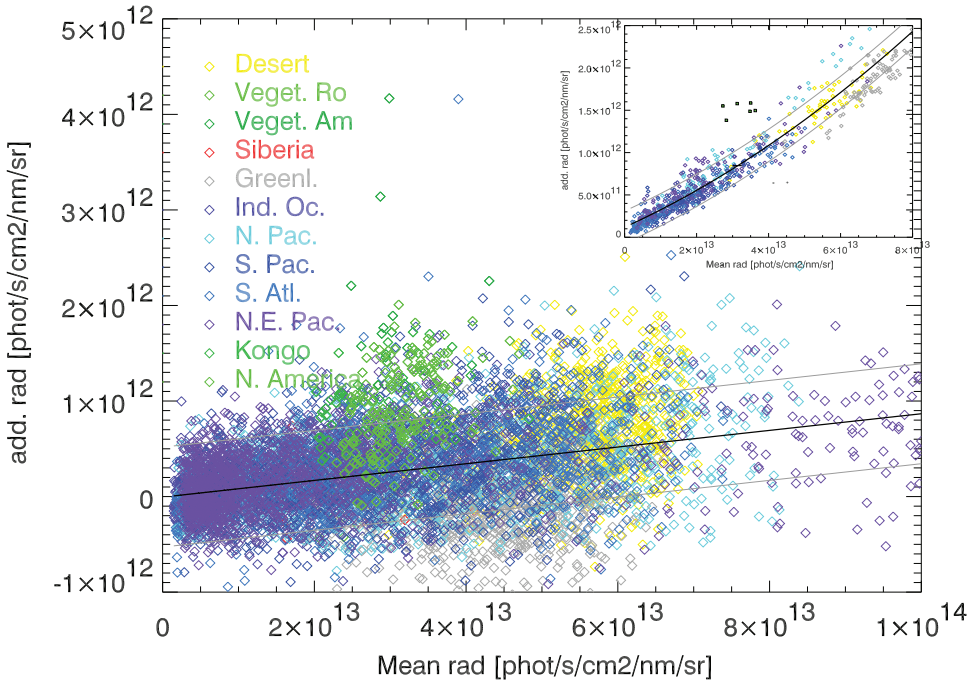

Figure 5.11: The retrieved ε values from GOME-2 for one day of measurements over vegetated and non-vegetated regions. For the sake of comparison, the same plot for SCIAMACHY measurements has been shown in the corner (top-right). Each non-green color represents a region shown in Fig. 4.1. The green points represent retrievals over densely vegetated areas (amazon forests and DR Congo). The obtained ε values for GOME-2 show significantly larger uncertainties than for SCIAMACHY although the fitted $\hat{\varepsilon}_a$ curve is less steep than for SCIAMACHY suggesting smaller zero-offset effect on average.

Chapter 6

Characterization of the Full-Spectrum SIF

The relationship between SIF and the vegetation properties is not limited to the absorbed radiation and CO_2 exchange by the canopy. Retrieving fluorescence over its entire emission spectrum is advantageous, since the relative magnitude of the red and far-red peaks of fluorescence provide additional information on plants health and status. For example, increasing leaf Chl content is associated with a decrease in the red/far-red fluorescence ratio in plants [Buschmann, 2007]. From a different perspective, the plant physiology and biological characteristics of the leaf are also closely connected to the spectral shape of the canopy reflectance within this spectral region (see Fig. 6.4), here referred to as the red-edge. Bearing in mind that SIF emission is also driven by the same characteristics, an interconnection can be seen between SIF signal and the red-edge spectral shape. Therefore, by modeling the canopy reflectance around the red-edge spectral area, SIF can be retrieved from its full emission spectral window. However, the feasibility of such retrieval strongly depends on the modeling accuracy, considering the relative magnitude of the SIF emission signal and reflected radiance from the canopy. An independent study has been conducted on the contribution of SIF and canopy/leaf parameters to the net reflected radiance. The main objective of this study is to assess the possibility of retrieving SIF from its full emission spectral range using hyper-spectral radiance measurements from TOA.

With currently available sun-induced plant fluorescence retrievals, including the one presented in this work, it is not possible to derive the full spectrum in its entirety. Instead, retrievals will typically be set up in a spectrally segmented manner (shown by e.g. Joiner et al. [2011, 2012, 2016]). However, as specific wavelength intervals typically need

specific adoption, and since calibration errors will play different roles in different wavelength segments, such retrievals will most likely lead to none-seamless/discontinuous results.

Nevertheless, while far-red SIF has been shown to be useful for several applications, retrieving both the red and far-red SIF will offer additional information. For example, the ratio of the red and far-red peaks and their individual emission intensities are sensitive to nitrogen uptake (see Rossini et al. [2015], Joiner et al. [2016]) and stress levels of the plant. Analyses of stress responses by red and far-red signals for both leaf and canopy measurements indicate a better detection of water stress in the far red as compared to the retrievals of red fluorescence only. Red and far-red canopy fluorescence measurements may give also information from different layers of a canopy or leaf due to higher amounts of reabsorption within the red spectral intervals. This may lead to higher sensitivity of the far-red signal to deeper layers of the canopy [Verrelst et al., 2015]. Agati et al. [2000] discussed the impact of PSI and temperature sensitivity on the ratio of far-red to red fluorescence emissions. The radiative contribution of PSI increases with wavelength and is considered to be less affected by biochemistry than the PSII contribution which is, according to Verrelst et al. [2015], affected by physiological regulations, leaf structure and chemical composition of the leaves. They also showed that the photosynthetic capacity (through quantification of the carboxylation rate), has its greatest influence on the red emission peak. They claim further that when trying to relate SIF to GPP, it would be more beneficial to exploit the full broadband emission flux as compared with a single band in the far red.

Overall, the retrieval of the full spectrum sun-induced plant fluorescence emission will be highly beneficial but also challenging. Using the methods presented so far, SIF cannot be simply disentangled from the dominant broadband spectral features, such as the red-edge and atmospheric scattering signatures. The principle idea, developed in the course of this study, was to characterize the spectral behaviour of vegetated ground pixels (red-edge) as close as possible without taking into account SIF. The difference between such a spectrum and the measured spectra ubiquitously should carry the (more or less strong) spectral signature of the SIF signal if a certain accuracy level is exceeded.

6.1 Resembling of broad-band measurements to retrieve SIF

Two different methodologies have been tested: the first one was related to signal processing methods, not accounting for the biophysical processes but rather resembling the red-edge by well-known signals which can flexibly be adjusted/fitted to a measured red-edge. The second was using the coupled canopy-leaf-level model PROSAIL with

SCIATRAN to resemble the red-edge based on model assumptions.

Only very few attempts (e.g. Miller et al. [1990]) have been made to simulate the red-edge accurately using signal-processing techniques. To test the abilities of such techniques, several functional descriptions of the red-edge have been utilized. An example is the Heaviside step function, which is defined as the integral of the Dirac delta function. Due to its characteristics, it demonstrates a sudden variation from zero to one in its original form. A smoother approximation of it is the Sigmoid function, which, in its simplest form, can be defined as $H(x) = 1/(1 + \exp(-2kx))$, in which k is a coefficient for x. Smaller k corresponds to smoother transition for the function. However, the complex dependency of the red-edge's spectral shape on physiology of the plants and canopy structure could not be approximated by these functions. The Sigmoid function could roughly resemble the overall shape of the signal, although it fails to reach the required accuracy. The SIF signal is usually less than 5% of the reflected radiance (Fig. 6.1). Therefore, successful retrieval of SIF by approximating the reflectance requires high accuracy. Other attempts such as Chebyshev polynomials or resembling the first derivative of the red-edge by a Gaussian were also not reaching critical levels of accuracy.

An important outcome of the former study (retrieving SIF from a spectral micro-window) was that the spectral reconstruction of the red-edge clearly necessitates a more accurate description of the bio-photochemical processes at leaf and canopy levels in order to reach the required accuracy to finally retrieve SIF. The second step was therefore to involve the above mentioned coupled canopy-leaf-level model PROSAIL with SCIATRAN to resemble the red-edge based on model assumptions. PROSAIL[1] [Jacquemoud et al., 2009] is a combination of PROSPECT leaf optical properties model and the Scattering by Arbitrary Inclined Leaves (SAIL) being a canopy BRDF model. The structural and physiological characteristics of the canopy drive the spectral shape and magnitude of the reflected radiance, thus red-edge and SIF. Please note, that the latter (SIF) dependence is not part of the standard PROSAIL.

To recap, PROSAIL simulates the canopy reflection spectrum. The main input variables of PROSAIL are the leaf structure parameter (N_{str}), chlorophyll content (C_{ab} [μg cm^{-2}]), Dry matter content (C_m [g cm^{-2}]), equivalent water thickness (C_w [cm]) and brown pigment content (C_{bp}) together with the LAI, leaf inclination distribution function (LIDF), soil reflectance and measurement geometry.

Bacour et al. [2002] applied a least square fitting method on the parameters of PROSAIL to estimate the relative contribution of each parameter to the directional

[1] see section section 2.1.3

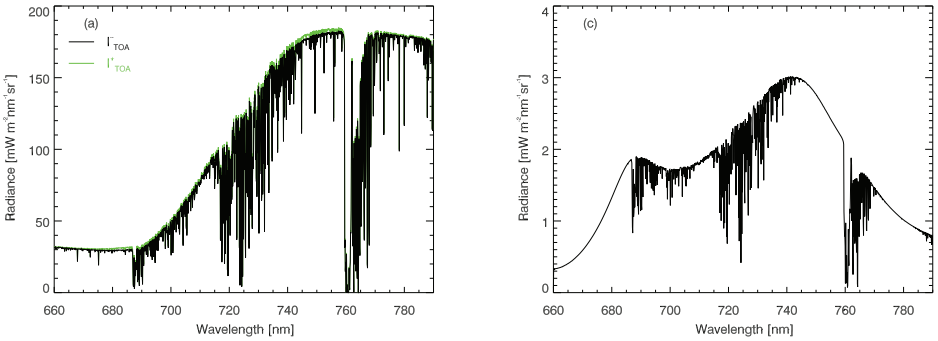

Figure 6.1: Modelled monochromatic radiances at TOA using SCIATRAN/PROSAIL to illustrate the difference between such radiances in (a) presence I^+ (green curve) and absence I^- (black curve) and (b) the difference $I^+ - I^-$. The maximum values of I^+ or I^- in the far-red part of the red-edge is two orders of magnitude larger than the corresponding SIF signal.

hemispherical reflectance[2] at TOC. From Fig. 6.4 one can see that in the spectral region of fluorescence emission, chlorophyll content, Average Leaf Angle (ALA) and LAI are the main contributors to the red-edge spectral shape although their influences vary significantly moving from visible to the near-infrared range [Jacquemoud et al., 2009].

The dependence of the vegetation reflectance on the leaf/canopy properties has been studied for decades (e.g. Dawson et al. [1998]). Specially, the foliar biochemical characteristics and their relationship to the reflection have been investigated e.g. by Curran et al. [1992], Dawson et al. [1999], Jago et al. [1999].

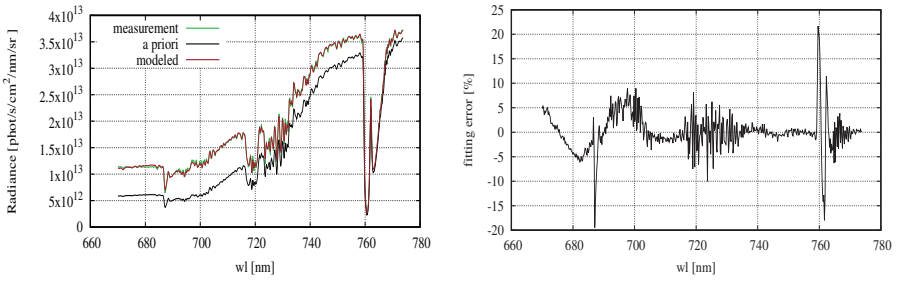

Figure 6.2: Left: Radiance at TOA measured by SCIAMACHY has been reproduced utilizing the SCIATRAN RTM coupled with PROSAIL leaf-canopy model. The spectral resolution of the model is synchronized to the FWHM of 0.48 nm for SCIAMACHY. Right: The fit residuals

[2] is the integral of the BRDF over all viewing directions

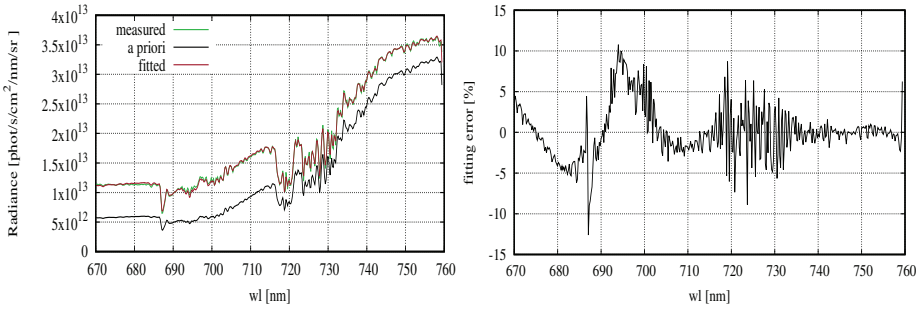

Figure 6.3: Left: Radiance at TOA measured by SCIAMACHY has been reproduced utilizing the SCIATRAN RTM coupled with PROSAIL leaf-canopy model. The spectral resolution of the model is synchronized to the FWHM of 0.48 nm for SCIAMACHY. Right: The fit residuals

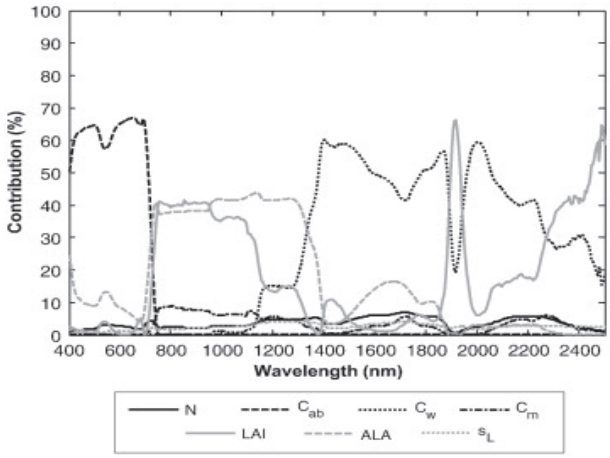

Figure 6.4: Spectral variation of the contributions of the PROSAIL variables to the TOC directional hemispherical reflectance [Jacquemoud et al., 2009].

6.2 Data selection

The radiance measured by SCIAMACHY and GOME-2 at TOA over vegetated regions has been modeled to investigate the quality of the SCIATRAN/PROSAIL to describe real space-borne measurements over vegetation. Two different locations have been chosen in vegetated areas in order to fit the model-based weighting functions to GOME-2 top of atmosphere measurements on Metop-A (level 1 data/version 5.3). The latter has been chosen, as GOME-2 provides significantly better spatial resolution (80 $\times$ 40 km^2) over the entire red-edge wavelength range than SCIAMACHY (240 $\times$ 30 km^2). Both locations have been selected to be densely vegetated and over the United States: region A, being a site dominated by oak tree forest in West Virginia centered at 41.05 latitude and -96.59 longitude; region B, being over agricultural fields mostly covered by different crop types in South-Western Missouri centered at 36.54 latitude and -90.28 longitude. The period investigated was June 2010. It has been ensured that cloud coverage in the selected regions is minimum by using the cloud fraction given with the level 1 data sets. The cloud fraction threshold used for this study was < 0.01.

Additionally, a measurement over Sahara has been chosen, located at 11.78 longitude and 23.62 latitude. This measurement has been used as a training data set in order to ensure that the SIF retrieval is not feasible over non-vegetated areas and any other SIF-like signal does not interfe with the retrieval. Since the training data set should not necessarily be cloud free, no cloud fraction threshold has been specified for this measurement.

6.3 Retrieval method

The retrieval is formulated based on a weighting function concept. In the framework of this study, a weighting function is defined as the Jacobian matrix of an a priori radiance with respect to the leaf/canopy properties as defined in the model. It has been assumed that any small difference between a modeled radiance and a measured radiance over vegetation can be compensated by a proper combination of scaled weighting functions:

$$I_m(\lambda) \approx I(\lambda) + \sum_{n=1}^{N} w_n(\lambda)\, x_n\,. \tag{6.1}$$

In Eq. 6.1, $I(\lambda)$ and $I_m(\lambda)$ are the modeled and measured radiances respectively. $w_n(\lambda)$ is the weighting function of each parameter if N different parameters are taken into account. x_n are the corresponding scaling factors.

In the course of this study, several minimization methods have been used of which

the simplest was linear least squares fitting to determine the values of x_n. It has been found, that unconditioned scaling of the weighting functions could in fact minimize the difference between GOME-2 reflectance measurements and SCIATRAN/PROSAIL model results to an acceptable level. However, no retrieved quantity had meaningful physical values.

Given the measurement-based fit quality, a study has been conducted to assess the possibility of fitting SIF over its full spectral range using model-based studies. This study aimed to investigate the feasibility of such method to disentangle the spectral shape of SIF from the canopy reflection, despite inter-connections. In fact, the spectral signature of SIF and some of the relevant leaf/canopy characteristics are not orthogonal. As Verrelst et al. stated in 2015, SIF shows the highest dependence on LAI, the canopy structure and chlorophyll content (C_{ab}) of the leaves. The numerical studies within this work, using PROSAIL/SCIATRAN combination confirmed this finding. Among the parameters provided by the model, the spectral influence of LAI and C_{ab} have been found to have highest correlation with fluorescence. That being provided, a study has been performed introducing an a priori and a modeled radiance which differs from the a priori by 10% variation in the C_{ab} parameter and SIF emission spectrum. SIF has been retrieved with high accuracy (average errors were smaller than 0.01%). The fitted reflectance and errors are plotted and shown in Fig. 6.5. One can see that the fit residuals are sufficiently small.

However, due to the non-orthogonality of the parameters, the fitting uncertainties increase by varying LAI and C_{ab} simultaneously. Fig. 6.6 illustrates the same fit but with 10% increase in both chlorophyll content and LAI with respect to the a priori radiance. The fitting errors are one order of magnitude larger than the fit errors in Fig. 6.5. This indicates that the fit is sensitive to the correlations between the fitting parameters. However, the uncertainties are still in an acceptable range and SIF can be retrieved with high accuracy. Fig. 6.7 illustrates the scaled SIF weighting function together with the fitted spectrum for SIF. Given the high sensitivity of the fit to the internal dependencies between leaf/canopy parameters, a thorough analysis is necessary to define boundary conditions and internal dependencies in order to reduce the degrees of freedom in the fit.

Model-based studies confirmed the feasibility of the method to retrieve fluorescence from its full emission spectrum as long as AOD and atmospheric gaseous profiles are known to a certain extent. Extending the spectral wavelength window to the outside of fluorescence emission window showed an improvement in the retrieval since the spectral signatures of leaf/canopy parameters can be fitted independently in the regions of no correlation with SIF. Applying additional boundary conditions to the model, the

spectral stability of the fit has been improved in the model-based retrieval.

Furthermore, extending the fitting spectral window to the visible range can have potential benefits since parameters such as chlorophyll concentration (C_{ab}) can be retrieved in this spectral region without contribution from SIF (see Fig. 6.4). It should be also taken into account that the canopy model has certain simplifications and uncertainties which can affect the fit.

Baret and Buis [2008] could show that there is a clear instability in the solution of the inverse problem when fitting these leaf/canopy parameters. As they stated high correlation is found between some sets of leaf/canopy parameters, which should be compensated for solving the inverse problem. They stated that "...regularization techniques are necessary to obtain a stable and reliable solution of the ill-posed inverse problem. This could be achieved both by using prior information on the distribution of the variables, and by exploiting some constrains on variables." [Baret and Buis, 2008]

In absence of a model to constrain the individual retrieval values and potentially iterate them another approach has been taken: here, Quadratic Programming (QP), a process of solving a (linearly constrained) quadratic optimization problem has been used.

In Eq.6.1, to obtain x as the vector of unknown scaling factors (x_n), the quadratic problem solved in the current approach is defined as follows:

$$0.5\, x^T H x + q^T x \rightarrow min, \tag{6.2}$$

in which x^T denotes the vector transpose of x. H represents the Hessian matrix of weighting functions and q is the product of $I_m(\lambda) - I(\lambda)$ with the matrix of weighting functions (the Jacobian). The advantage of such, rather sophisticated, retrieval method is to supply meaningful physical constrains to the minimization. Please note, that in presence of a full-physical retrieval such constrains would have been taken over by a RTM.

Weighting functions have been prepared and utilized for the following atmospheric and canopy parameters, as, after careful model studies, they have been found to be the most influential and/or orthogonal ones:

- chlorophyll a+b content C_{ab}
- aerosol optical depth (AOD)
- leaf structure parameter N_{str}
- average leaf inclination angle

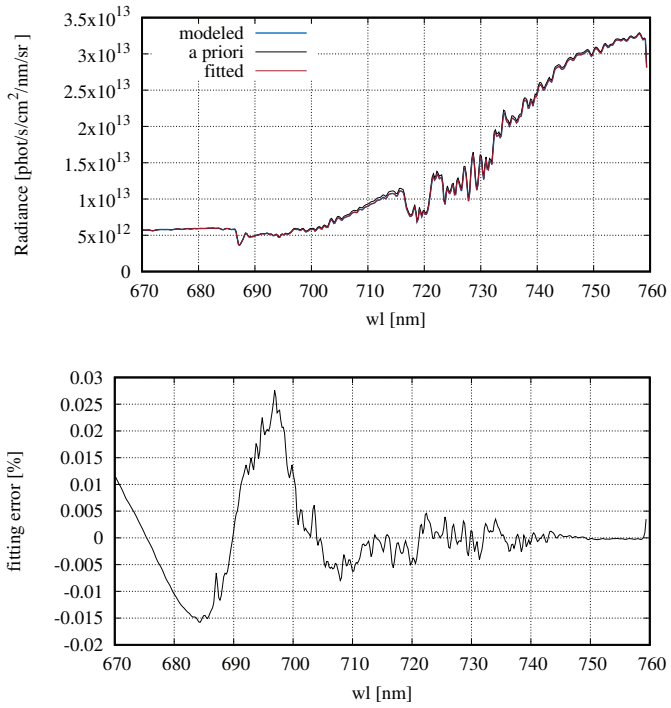

Figure 6.5: Top: Simulations of the fitted canopy reflection applying 10% *error to Chlorophyll concentration of the leaves in the leaf-canopy model (PROSAIL). Bottom: The fit residuals.*

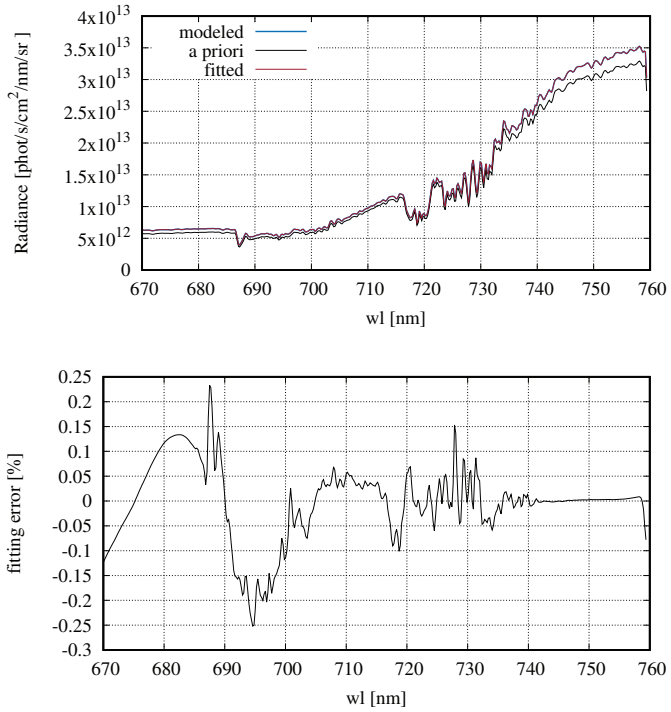

Figure 6.6: Top: Simulations of the fitted canopy reflection applying 10% *error to Chlorophyll concentration of the leaves and* 10% *error to the LAI of the canopy in the model. Bottom: The fit residuals.*

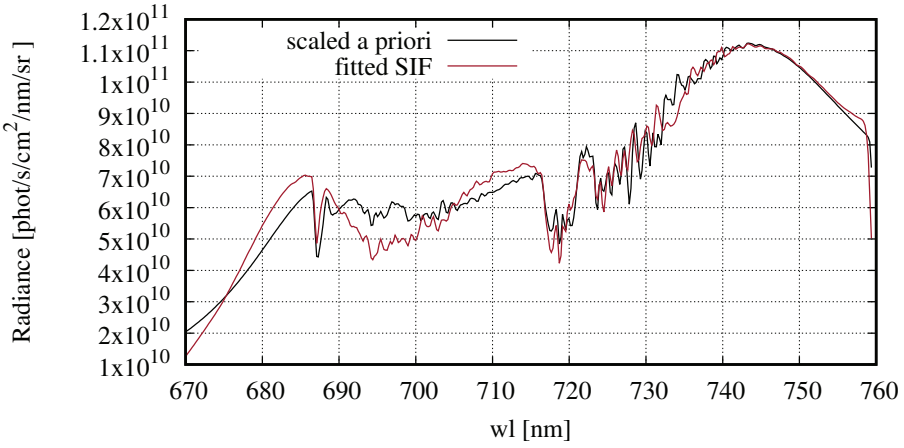

Figure 6.7: The fitted fluorescence for model-based retrieval, varying LAI and C_{ab} each by 10%.

- equivalent water thickness C_w
- leaf area index LAI
- water vapour concentration in the atmosphere

The a priori has been modeled based on the adequate measurement geometry, elevation and surface pressure of the corresponding measurement. Additionally, the gaseous absorption scenarios have been selected according to the month and latitude in which the measurement has been taken, in order to produce the most adequate a priori radiance for each measurement scenario.

6.4 Results

To investigate the feasibility of applying QP, the first step was to fit the measured radiances to the scaled sum of weighting functions (according to Eq. 6.1) without taking fluorescence into account. The fitting has been done through iterations. To find the first approximation of the a priori it is necessary to avoid strong influences of gaseous absorption to obtain parameters, that are sufficiently close to the reality. Therefore, a segmented radiance has been modeled in the spectral regions, with small to no gaseous absorption. Fig. 6.8 illustrates a sample of segmented red-edge fit, providing the a priori values for the parameters necessary as the starting scenario for the full spectral fit. Similarly, a segmented fit only in O_2-A absorption band is conducted to provide an a priori AOD close enough to the measurement condition.

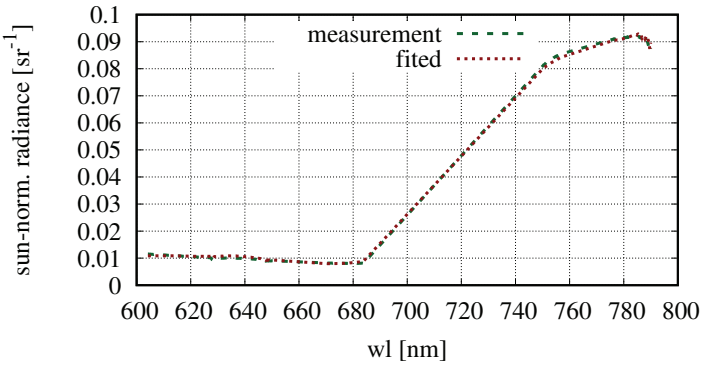

Figure 6.8: The fitted radiance for segmented spectral intervals, containing minimum gaseous absorption. The fit error for such case has reached 1% providing adequate a priori values to be utilized in the first iteration while fitting the red-edge over its full spectral window.

As stated above, the dependence of the radiance on the leaf/canopy properties identified by the PROSAIL model is extremely non-linear. Therefore, the constrains set for each parameter, within each iteration, were based on literature studies on the model (mostly based on Jacquemoud [1993], Jacquemoud et al. [2009] and Borel [2010]) and for each iteration, the maximum allowed variation for each parameter is set to be as follows:

- $C_{ab} \sim 20\%$.
- $AOD \sim 20\%$
- $C_w \sim 50\%$
- leaf inclination angle $\sim 10\%$
- LAI $\sim 20\%$

Fig. 6.9 shows the resulting residuals for using constrained QP. While the residuals for the retrievals over region A and B were following similar spectral patterns, the residual for a retrieval over Saharan desert (clearly not vegetated) shows obvious differences. As all retrievals used here where aiming to minimize the differences between measured and modeled radiances (through scaled weighting functions) fluctuations of those residuals around a zero baseline is inevitable. However, for both vegetated regions, the peaks of SIF located near 680 nm and 740 nm stand out, showing evidence of a retrievable spectral signature of SIF. Thus, in the next step a parametrization of the SIF canopy emission spectrum has been introduced to the minimization problem together with above mentioned weighting functions within QP. Subhash and Mohanan

[1997], Zarco-Tejada et al. [2000] and Joiner et al. [2013a] showed (in a different context) that a Gaussian representation of the SIF emission spectrum around each maximum, resembles the emission spectral shape sufficiently well. Following this idea and adapting it to this approach, weighting functions for the central position, the width and the amplitude for both Gaussians have been defined and introduced to the model. Fig. 6.11 and 6.12 illustrate the summation over both fitted Gaussians as well as the fitting errors. One can see that the retrieved SIF signals for both measurements have reasonable magnitudes. However, the spectral shapes of the two retrievals are relatively different. For measurement A, the retrieved fluorescence signal demonstrates a significantly larger far-red peak than the relatively small red peak. This could be due to reabsorption of the SIF signal in red spectral region, since LAI for this area is typically larger than two. According to a study conducted by Sušila and Nauš [2007], the contribution of the chlorophyll fluorescence signal to the reflectance and transmittance of the leaves is different. The contribution of the fluorescence signal to reflectance and transmittance can be seen from Fig. 6.13. They argued that for stronger absorption (i.e. larger LAI and/or C_{ab}) the second fluorescence peak shows significantly larger values with respect to the first peak. On the other hand, stronger reflectance can be associated to a more balanced contribution from both emission peaks. The outcome of the retrievals for regions A and B confirmed this argument. As it can be seen from Fig. 6.10, the measured radiance for region A demonstrates smaller reflection in the red spectral range than for region B. In the same manner, as shown in Fig. 6.12, for an agricultural area with smaller LAI and stronger reflection (region B) the ratio between the red and far-red peaks is smaller than for region A.

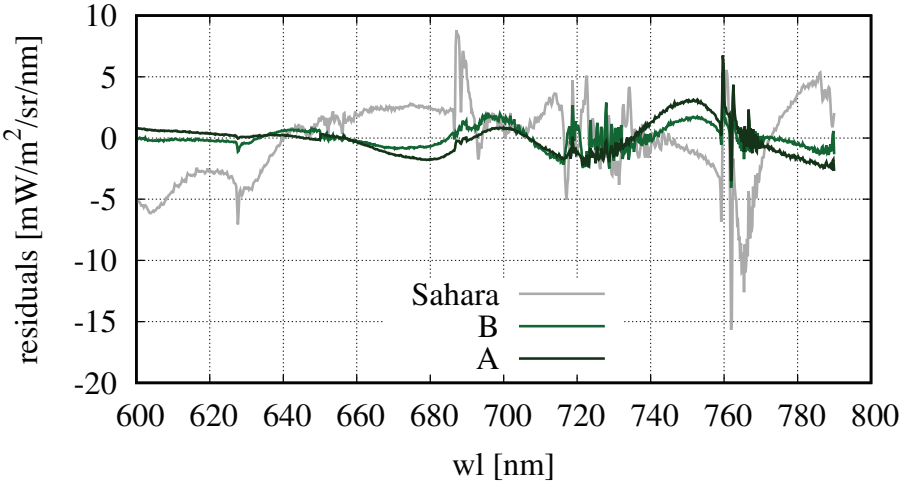

Figure 6.9: The fit residuals are plotted for three selected measurements over measured radiance over (A) a region mainly dominated by oak tree forests in West Virginia, (B) dominated by agricultural fields over Missouri state in the US and a measurement over Sahara which is ensured to be non-vegetated. The fit residuals from both vegetated regions show a clear difference to the residual spectra obtained from Sahara.

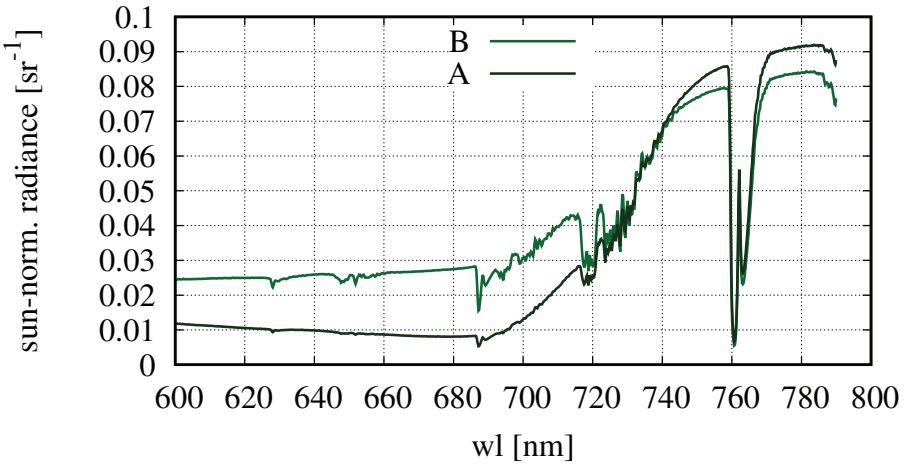

Figure 6.10: The sun-normalized radiances measured over regions (A) demonstrate stronger reflectance in the red spectral area than region (B). (A) represents an area of mainly oak tree forests and (B) is dominated by agricultural fields.

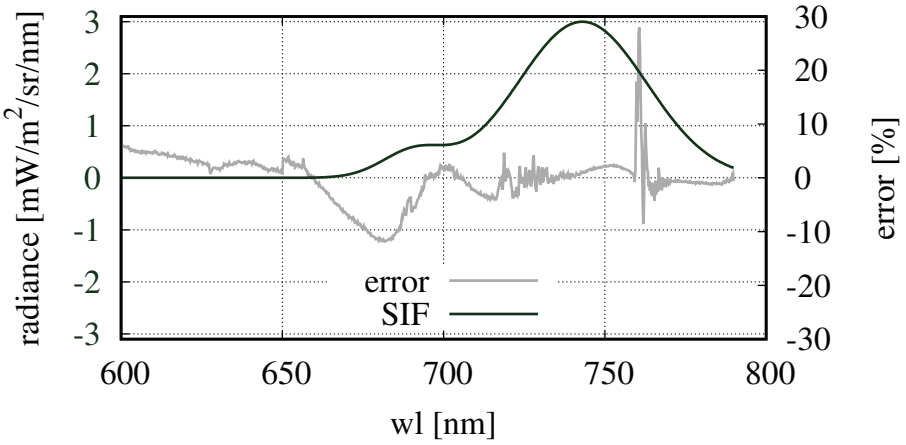

Figure 6.11: The fitted double Gaussian function for measurement A (green) together with the fit errors (gray).

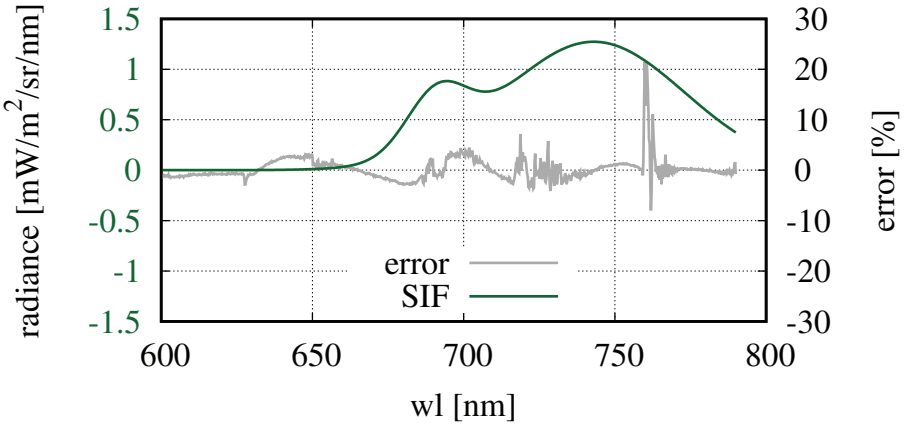

Figure 6.12: The fitted double Gaussian function for measurement B (green) together with the fit errors (gray).

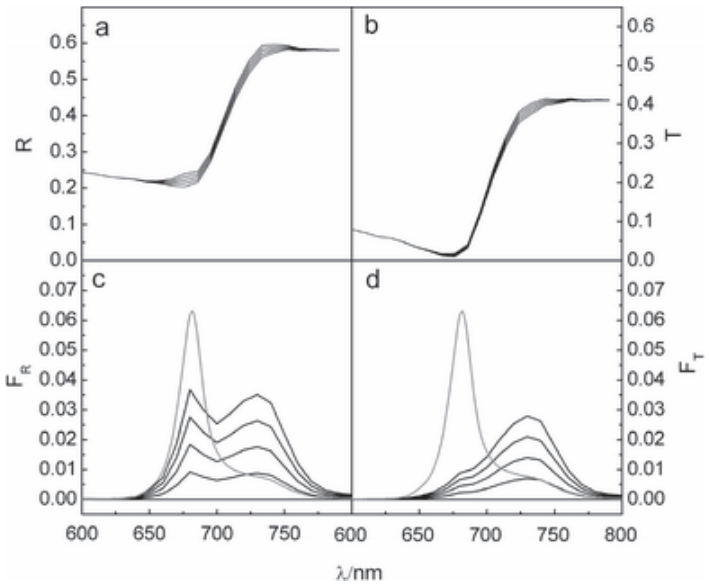

Figure 6.13: Spectra of leaf reflectance (a) and transmittance (b) modeled for diffused excitation light with the spectral resolution of 10 nm and for different fluorescence quantum yields (0, 0.02, 0.04, 0.08 from the bottom to the top curves). Fluorescence contributions to reflectance (c) and transmittance (d) are calculated and plotted together with assumed intrinsic fluorescence (gray curves). [Sušila and Nauš, 2007]

Chapter 7

Conclusions and Outlook

The relationship between photosynthesis and the Solar Induced Fluorescence (SIF) is of interest because SIF emission occurs simultaneously with photosynthesis and can potentially reveal information about the photosynthetic process and the physiological status of the photosynthetic organism (e.g. plants).

In this dissertation, novel methods have been developed and applied to retrieve SIF from space-borne measurements of radiance at the top of atmosphere (TOA). The results have been compared to the retrieved fluorescence obtained by recent studies in the field and to the photobiochemical properties of the canopy. Finally, the possibilities of fitting the reflected radiance and SIF over its full emission spectrum has been examined and assessed.

7.1 Conclusion

Provided that SIF is two orders of magnitude smaller than the upwelling radiance reflected from the vegetation at TOA, the main obstacles for its retrieval are the distortion of the signal due to atmospheric gaseous absorption [Frankenberg et al., 2012], as well as the spectral features with similar radiative behavior to SIF but different origins [Frankenberg et al., 2011b]. The first developed retrieval method uses a micro-wavelength-window in order to avoid telluric absorption bands and is accompanied by a correction scheme which has been developed as part of this study to account for additive signals not originating from SIF.

A thorough sensitivity analysis has been conducted on simulated data to assure the feasibility of the chosen approach and to define its limitations. Deriving from model studies, SCIAMACHY measurements in the far-red spectral region between 748.5 -753.0 nm have been chosen to be implemented in the retrieval method. Applying the

approach on a 10-year SCIAMACHY data showed that, the global SIF distribution is consistent with expected results and those already published. A direct comparison of the obtained SIF values with results from NASA's GSFC data (version 26) based on Joiner et al. [2013b] and Joiner et al. [2013a] from the GOME-2 instrument exhibited general agreement. However, there have been differences in details. The disagreements could be partially explained by differences in the spatial resolution and the overpass times of SCIAMACHY and GOME-2 instruments and the intrinsic differences in the retrieval methods. Generally speaking, the obtained SIF values exhibit a broader variation range of 0 - 4 mW m^{-2} $sr^{-1}nm^{-1}$, while Joiner et al.'s results were clearly confined within 0 - 2 mW m^{-2} sr^{-1} nm^{-1}. The retrieved SIF together with the comparison to the retrieved results by Joiner et al. [2013b] have been published in 2015 [Khosravi et al., 2015]. In parallel, Köhler et al. [2015b] presented SIF retrievals from SCIAMACHY and GOME-2 being more than 1.5 times larger than the SIF values provided by Joiner et al. [2013a] and Joiner et al. [2013b]. The final judgment of the results is not possible, since ground truth and validation sources are not available on comparable scales at SCIAMACHY and GOME-2 footprints [Khosravi et al., 2015, Köhler et al., 2015b]. Although the future instruments such as the Sentinel-5 Precursor (S5P) and the Fluorescence Explorer (FLEX) will provide more opportunities, assessing the reliability of results in this work is conducted based on temporal variation of vegetation and photosynthetic driven quantities such as GPP and APAR.

The global retrievals of SIF showed a clear correlation with seasonality of vegetation in both hemispheres. Additionally, since several studies suggested a strong dependence of SIF on photosynthesis and particularly on GPP (for instance see Frankenberg et al. [2011b], Guanter et al. [2014], Joiner et al. [2013b], Damm et al. [2015], Zhang et al. [2014, 2016b]), the GPP and APAR derived from flux-tower measurements have been averaged for each month and compared with the monthly mean SIF values obtained from SCIAMACHY, co-located with the towers. The agreement between corresponding monthly trends were clear despite the fact that the large footprint of SCIAMACHY is not already comparable with the area of GPP and APAR measurements. A recent study by Zhang et al. [2016b] showed that APAR regulates the linear relationship between the canopy-level GPP and SIF. This finding is in full agreement with the results obtained in this work.

Finally, the radiative transfer model SCIATRAN has been coupled with the leaf/canopy vegetation-model PROSAIL in order to investigate the possibility of resembling SIF over its full emission spectrum as well as canopy parameters such as LAI. Due to the close connection between SIF and the canopy reflection, an initial step is to model the canopy reflection with a sufficiently high accuracy. Several approaches have been assessed

based on numerical simulations, aiming to reproduce canopy reflectance using Jacobians of the radiance with respect to leaf/canopy parameters. In fact, considering the relative magnitude of SIF with respect to the reflected radiance from the canopy, minimizing the fitting residuals is extremely important. It has been proven that the developed algorithm can resemble measurements to a certain extent. However, simulations showed that O_2 absorption bands increase fitting errors by introducing additional inaccuracy to the fit. Moreover, although numerical simulations had proven the feasibility of the retrieval approach, cross-correlations between the fit parameters had to be taken into account. Therefore, an iterative fitting method has been developed that within its first step the AOD and gaseous absorption are approximated using segmented wavelengths. The outcomes of this step are utilized as a priori values to fit the leaf/canopy parameters (e.g. chlorophyll content of the leaves (C_{ab}) and LAI) as well as SIF over its full spectral emission window. Examples of the fit and the retrieved SIF have been presented in this work.

7.2 Outlook

The approach presented here is of generic nature and can thus be applied to other datasets as well. Adapting the retrieval method to GOME-2 instrument is beneficial due to the advantages it provides. The comparison of the results to the ground-based measurements from flux-towers could be also extended to other regions (e.g. Europe), permitting the possibility of comparisons between seasonal trends on different continents.

As discussed before, the numerical studies on reproducing the measured radiance from vegetated targets and retrieving LAI, C_{ab} and SIF showed promising results. Setting a priori values for LAI and C_{ab}, simulations showed that SIF over its full spectral emission window can be retrieved with high accuracy. Future effort shall address the refinement of the model with respect to the inter-correlations between the variables, providing potential boundary conditions to retrieve SIF over its full spectral emission range. Further investigations on the inter-correlations between the leaf-canopy variables and fluorescence are necessary to improve the retrieval. Moreover, the iterative retrieval algorithm shall be implemented in the radiative transfer model in order to have global retrievals. Additionally, the retrieved SIF has to be validated against ground truth data and satellite-based global retrievals. comparison of other retrieved parameters such as C_{ab} are also possible through available sources such as the MERIS terrestrial chlorophyll index [Dash and Curran, 2004].

The future of Solar-Induced Fluorescence is tied to the relationship between fluorescence emissions and photosynthetic activity. This will provide the opportunity to

assess the anthropogenic influence on global and regional vegetation and the vegetation stress detection.

Earth observation missions thus far have been limited with respect to spatial and spectral resolutions, they have successfully dealt with land-cover types and large-scale changes. Future missions will improve the quality of the fluorescence retrieval. The data provided by such missions combined with model-based studies opens a door to studying photosynthesis and photosynthetic efficiency.

Bibliography

Mark C Abrams, GC Toon, and RA Schindler. Practical example of the correction of fourier-transform spectra for detector nonlinearity. *Applied optics*, 33(27):6307–6314, 1994.

Giovanni Agati, Zoran G Cerovic, and Ismaël Moya. The effect of decreasing temperature up to chilling values on the in vivo f685/f735 chlorophyll fluorescence ratio in phaseolus vulgaris and pisum sativum: The role of the photosystem i contribution to the 735 nm fluorescence band. *Photochemistry and Photobiology*, 72(1):75–84, 2000.

Luis Alonso, Luis Gómez-Chova, Joan Vila-Francés, Julia Amorós-López, Luis Guanter, Javier Calpe, and José Moreno. Improved fraunhofer line discrimination method for vegetation fluorescence quantification. *Geoscience and Remote Sensing Letters, IEEE*, 5(4):620–624, 2008.

J Amorós-López, L Gomez-Chova, J Vila-Frances, L Alonso, J Calpe, J Moreno, and S del Valle-Tascon. Evaluation of remote sensing of vegetation fluorescence by the analysis of diurnal cycles. *International Journal of Remote Sensing*, 29(17-18): 5423–5436, 2008.

Cédric Bacour, Stéphane Jacquemoud, Marc Leroy, Olivier Hautecœur, Marie Weiss, Laurent Prévot, Nadine Bruguier, and Habiba Chauki. Reliability of the estimation of vegetation characteristics by inversion of three canopy reflectance models on airborne polder data. *Agronomie-Sciences des Productions Vegetales et de l'Environnement*, 22(6):555–566, 2002.

Neil R Baker and Eva Rosenqvist. Applications of chlorophyll fluorescence can improve crop production strategies: an examination of future possibilities. *Journal of experimental botany*, 55(403):1607–1621, 2004.

Dennis Baldocchi, Eva Falge, Lianhong Gu, Richard Olson, et al. Fluxnet: A new tool to study the temporal and spatial variability of ecosystem-scale carbon dioxide, water vapor, and energy flux densities. *Bulletin of the American Meteorological Society*, 82 (11):2415, 2001.

Frederic Baret and Samuel Buis. Estimating canopy characteristics from remote sensing observations: Review of methods and associated problems. In *Advances in land remote Sensing*, pages 173–201. Springer, 2008.

William L Bauerle, Ram Oren, Danielle A Way, Song S Qian, Paul C Stoy, Peter E Thornton, Joseph D Bowden, Forrest M Hoffman, and Robert F Reynolds. Photoperiodic regulation of the seasonal pattern of photosynthetic capacity and the implications for carbon cycling. *Proceedings of the National Academy of Sciences*, 109(22):8612–8617, 2012.

Alexander Berk, Patrick Conforti, Rosemary Kennett, Timothy Perkins, Frederick Hawes, and Jeannette van den Bosch. Modtran6: a major upgrade of the modtran radiative transfer code. In *SPIE Defense+ Security*, pages 90880H–90880H. International Society for Optics and Photonics, 2014.

Lenny Bernstein, Peter Bosch, Osvaldo Canziani, Zhenlin Chen, Renate Christ, Ogunlade Davidson, W Hare, S Huq, D Karoly, V Kattsov, et al. Climate change 2007: Synthesis report: An assessment of the intergovernmental panel on climate change. Technical report, IPCC, 2008.

Joseph A Berry, Christian Frankenberg, Paul Wennberg, Ian Baker, Kevin W Bowman, Saulo Castro-Contreas, Maria Pilar Cendrero-Mateo, Alexander Damm, Darren Drewry, Bethany Ehlmann, et al. New methods for measurement of photosynthesis from space. *Geophys. Res. Lett*, 38:L17706, 2012.

Sophie Bontemps, Pierre Defourny, Eric V Bogaert, Olivier Arino, Vasileios Kalogirou, and Jose R Perez. Globcover 2009-products description and validation report. 2011.

Christoph C Borel. Vegetative canopy parameter retrieval using 8-band data. *DigitalGlobe 8-Band Research Challenge 2010*, 2010.

H. Bovensmann, J. P. Burrows, M. Buchwitz, J. Frerick, S. Noël, V. V. Rozanov, K. V. Chance, and A. P. H. Goede. SCIAMACHY: Mission objectives and measurement modes. *J. Atm. Sci.*, 56(2):127–149, 1999.

J. P. Burrows, M. Weber, M. Buchwitz, V. Rozanov, A. Ladstätter-Weißenmayer, A. Richter, R. de Beek, R. Hoogen, K. Bramstedt, K-U. Eichmann, M. Eisinger, and

D. Perner. The global ozone monitoring experiment (GOME): Mission concept and first scientific results. *J. Atm. Sci.*, 56:151–175, 1999.

J.P. Burrows, E. Holzle, A.P.H. Goede, H. Visser, and W. Fricke. Sciamachy- scanning imaging absorption spectrometer for atmospheric chartography. *Acta Astronautica*, 35(7), 1995.

Claus Buschmann. Variability and application of the chlorophyll fluorescence emission ratio red/far-red of leaves. *Photosynthesis Research*, 92(2):261–271, 2007.

PKE Campbell, EM Middleton, JE McMurtrey, EW Chappelle, et al. Assessment of vegetation stress using reflectance or fluorescence measurements. *Journal of environmental quality*, 36(3):832–845, 2007.

K Chance and RL Kurucz. An improved high-resolution solar reference spectrum for earth's atmosphere measurements in the ultraviolet, visible, and near infrared. *Journal of quantitative spectroscopy and radiative transfer*, 111(9):1289–1295, 2010.

F Stuart Chapin III, Pamela A Matson, and Peter Vitousek. *Principles of terrestrial ecosystem ecology*. Springer Science & Business Media, 2011.

Emmett W Chappelle and Darrel L Williams. Laser-induced fluorescence (lif) from plant foliage. *IEEE transactions on geoscience and remote sensing*, (6):726–736, 1987.

Roderick K Clayton. *Photosynthesis: physical mechanisms and chemical patterns*, volume 4. Cambridge University Press, 1980.

Lawrence A. Corp, Elizabeth M. Middleton, Petya E. Campbell, K. Fred Huemmrich, Craig S. Daughtry, Andrew Russ, and Yen-Ben Cheng. Spectral indices to monitor nitrogen-driven carbon uptake in field corn. *Journal of Applied Remote Sensing*, 4 (1):043555–043555–10, 2010. doi: 10.1117/1.3518455.

Paul J Curran, Jennifer L Dungan, Bruce A Macler, Stephen E Plummer, and David L Peterson. Reflectance spectroscopy of fresh whole leaves for the estimation of chemical concentration. *Remote Sensing of Environment*, 39(2):153–166, 1992.

A Damm, L Guanter, E Paul-Limoges, C van der Tol, A Hueni, N Buchmann, W Eugster, C Ammann, and ME Schaepman. Far-red sun-induced chlorophyll fluorescence shows ecosystem-specific relationships to gross primary production: An assessment based on observational and modeling approaches. *Remote Sensing of Environment*, 166:91–105, 2015.

Alexander Damm, André Erler, Walter Hillen, Michele Meroni, Michael E Schaepman, Wout Verhoef, and Uwe Rascher. Modeling the impact of spectral sensor configurations on the fld retrieval accuracy of sun-induced chlorophyll fluorescence. *Remote Sensing of Environment*, 115(8):1882–1892, 2011.

Alexander Damm, Luis Guanter, Valérie C E Laurent, Michael E Schaepman, Anke Schickling, and Uwe Rascher. Fld-based retrieval of sun-induced chlorophyll fluorescence from medium spectral resolution airborne spectroscopy data. *Remote Sensing of Environment*, 147:256–266, 2014.

Jadunandan Dash and Paul J Curran. The meris terrestrial chlorophyll index. 2004.

F. Daumard, S. Champagne, A. Fournier, Y. Goulas, A. Ounis, J.-F. Hanocq, and I. Moya. A field platform for continuous measurement of canopy fluorescence. *Geoscience and Remote Sensing, IEEE Transactions on*, 48(9):3358–3368, 2010. ISSN 0196-2892. doi: 10.1109/TGRS.2010.2046420.

Fabrice Daumard, Yves Goulas, Abderrahmane Ounis, Roberto Pedros, and Ismael Moya. Measurement and correction of atmospheric effects at different altitudes for remote sensing of sun-induced fluorescence in oxygen absorption bands. *Geoscience and Remote Sensing, IEEE Transactions on*, 53(9):5180–5196, 2015.

Terence P Dawson, Paul J Curran, and Stephen E Plummer. Liberty—modeling the effects of leaf biochemical concentration on reflectance spectra. *Remote Sensing of Environment*, 65(1):50–60, 1998.

TP Dawson, PJ Curran, PRJ North, and SE Plummer. The propagation of foliar biochemical absorption features in forest canopy reflectance: A theoretical analysis. *Remote Sensing of Environment*, 67(2):147–159, 1999.

Gene Feldman and Norman Kuring. URL http://neo.sci.gsfc.nasa.gov/.

A. Fournier, F. Daumard, S. Champagne, A. Ounis, Y. Goulas, and I. Moya. Effect of canopy structure on sun-induced chlorophyll fluorescence. *{ISPRS} Journal of Photogrammetry and Remote Sensing*, 68:112 – 120, 2012. ISSN 0924-2716. doi: 10.1016/j.isprsjprs.2012.01.003.

C. Frankenberg, A. Butz, and G. C. Toon. Disentangling chlorophyll fluorescence from atmospheric scattering effects in o2 a-band spectra of reflected sun-light. *Geophysical Research Letters*, 38(3), 2011a. ISSN 1944-8007. doi: 10.1029/2010GL045896.

C. Frankenberg, C. O'Dell, L. Guanter, and J. McDuffie. Remote sensing of near-infrared chlorophyll fluorescence from space in scattering atmospheres: implications for its retrieval and interferences with atmospheric co_2 retrievals. *Atmospheric Measurement Techniques*, 5(8):2081–2094, 2012. doi: 10.5194/amt-5-2081-2012.

Christian Frankenberg, Joshua B. Fisher, John Worden, Grayson Badgley, Sassan S. Saatchi, Jung-Eun Lee, Geoffrey C. Toon, André Butz, Martin Jung, Akihiko Kuze, and Tatsuya Yokota. New global observations of the terrestrial carbon cycle from gosat: Patterns of plant fluorescence with gross primary productivity. *Geophysical Research Letters*, 38(17), 2011b. ISSN 1944-8007. doi: 10.1029/2011GL048738.

Christian Frankenberg, Chris O'Dell, Joseph Berry, Luis Guanter, Joanna Joiner, Philipp Köhler, Randy Pollock, and Thomas E Taylor. Prospects for chlorophyll fluorescence remote sensing from the orbiting carbon observatory-2. *Remote Sensing of Environment*, 147:1–12, 2014.

Mohammad Haji Gholizadeh, Assefa M Melesse, and Lakshmi Reddi. A comprehensive review on water quality parameters estimation using remote sensing techniques. *Sensors*, 16(8):1298, 2016.

Anatoly A. Gitelson, Yi Peng, Jeffery G. Masek, Donald C. Rundquist, Shashi Verma, Andrew Suyker, John M. Baker, Jerry L. Hatfield, and Tilden Meyers. Remote estimation of crop gross primary production with landsat data. *Remote Sensing of Environment*, 121:404 – 414, 2012. ISSN 0034-4257. doi: 10.1016/j.rse.2012.02.017.

H Charles J Godfray, John R Beddington, Ian R Crute, Lawrence Haddad, David Lawrence, James F Muir, Jules Pretty, Sherman Robinson, Sandy M Thomas, and Camilla Toulmin. Food security: the challenge of feeding 9 billion people. *science*, 327(5967):812–818, 2010.

M. Gottwald and H. Bovensmann, editors. *SCIAMACHY, Exploring the Changing Earth's Atmosphere*. Springer, 2011.

Yves Goulas, Antoine Fournier, Fabrice Daumard, Sébastien Champagne, Abderrahmane Ounis, Olivier Marloie, and Ismael Moya. Gross primary production of a wheat canopy relates stronger to far red than to red solar-induced chlorophyll fluorescence. *Remote Sensing*, 9(1):97, 2017.

JF Grainger and J Ring. Anomalous fraunhofer line profiles. *Nature*, 193:762, 1962.

L. Guanter, L. Alonso, L. Gomez-Chova, J. Amoros-Lopez, J. Vila, and J. Moreno. Estimation of solar-induced vegetation fluorescence from space measurements. *Geophysical Research Letters*, 34(8), 2007. ISSN 1944-8007. doi: 10.1029/2007GL029289.

L Guanter, L Alonso, L Gómez-Chova, M Meroni, R Preusker, J Fischer, and J Moreno. Developments for vegetation fluorescence retrieval from spaceborne high-resolution spectrometry in the o2-a and o2-b absorption bands. *Journal of Geophysical Research: Atmospheres*, 115(D19), 2010.

L Guanter, I Aben, P Tol, JM Krijger, A Hollstein, P Köhler, A Damm, J Joiner, C Frankenberg, and J Landgraf. Potential of the tropospheric monitoring instrument (tropomi) onboard the sentinel-5 precursor for the monitoring of terrestrial chlorophyll fluorescence. *Atmospheric Measurement Techniques*, 8(3):1337–1352, 2015.

Luis Guanter, Christian Frankenberg, Anu Dudhia, Philip E Lewis, José Gómez-Dans, Akihiko Kuze, Hiroshi Suto, and Roy G Grainger. Retrieval and global assessment of terrestrial chlorophyll fluorescence from gosat space measurements. *Remote Sensing of Environment*, 121:236–251, 2012.

Luis Guanter, Micol Rossini, Roberto Colombo, Michele Meroni, Christian Frankenberg, Jung-Eun Lee, and Joanna Joiner. Using field spectroscopy to assess the potential of statistical approaches for the retrieval of sun-induced chlorophyll fluorescence from ground and space. *Remote Sensing of Environment*, 133(0):52 – 61, 2013. ISSN 0034-4257. doi: 10.1016/j.rse.2013.01.017.

Luis Guanter, Yongguang Zhang, Martin Jung, Joanna Joiner, Maximilian Voigt, Joseph A. Berry, Christian Frankenberg, Alfredo R. Huete, Pablo Zarco-Tejada, Jung-Eun Lee, M. Susan Moran, Guillermo Ponce-Campos, Christian Beer, Gustavo Camps-Valls, Nina Buchmann, Damiano Gianelle, Katja Klumpp, Alessandro Cescatti, John M. Baker, and Timothy J. Griffis. Global and time-resolved monitoring of crop photosynthesis with chlorophyll fluorescence. *Proceedings of the National Academy of Sciences* , 2014. doi: 10.1073/pnas.1320008111.

Takashi Hamazaki, Yutaka Kaneko, Akihiko Kuze, and Kayoko Kondo. Fourier transform spectrometer for greenhouse gases observing satellite (gosat). In *Fourth International Asia-Pacific Environmental Remote Sensing Symposium 2004: Remote Sensing of the Atmosphere, Ocean, Environment, and Space*, pages 73–80. International Society for Optics and Photonics, 2005.

H.-W. Heldt. *Plant Biochemistry*. Elsevier Academic Press, 3. edition, 2005.

S Jacquemoud. Inversion of the prospect+ sail canopy reflectance model from aviris equivalent spectra: theoretical study. *Remote sensing of environment*, 44(2-3):281–292, 1993.

Stéphane Jacquemoud, Wout Verhoef, Frédéric Baret, Cédric Bacour, Pablo J Zarco-Tejada, Gregory P Asner, Christophe François, and Susan L Ustin. Prospect+ sail models: A review of use for vegetation characterization. *Remote Sensing of Environment*, 113:S56–S66, 2009.

Rosemary A Jago, Mark EJ Cutler, and Paul J Curran. Estimating canopy chlorophyll concentration from field and airborne spectra. *Remote Sensing of Environment*, 68 (3):217–224, 1999.

J. Joiner. Personal correspondence with respect to the **data download from http://avdc.gsfc.nasa.gov**, 07 2014.

J. Joiner, Y. Yoshida, A. P. Vasilkov, Y. Yoshida, L. A. Corp, and E. M. Middleton. First observations of global and seasonal terrestrial chlorophyll fluorescence from space. *Biogeosciences*, 8(3):637–651, 2011. doi: 10.5194/bg-8-637-2011.

J. Joiner, Y. Yoshida, A. P. Vasilkov, E. M. Middleton, P. K. E. Campbell, Y. Yoshida, A. Kuze, and L. A. Corp. Filling-in of near-infrared solar lines by terrestrial fluorescence and other geophysical effects: simulations and space-based observations from SCIAMACHY and GOSAT. *Atmospheric Measurement Techniques*, 5(4):809–829, 2012. doi: 10.5194/amt-5-809-2012.

J. Joiner, L. Guanter, R. Lindstrot, M. Voigt, A. P. Vasilkov, E. M. Middleton, K. F. Huemmrich, Y. Yoshida, and C. Frankenberg. Global monitoring of terrestrial chlorophyll fluorescence from moderate-spectral-resolution near-infrared satellite measurements: methodology, simulations, and application to gome-2. *Atmospheric Measurement Techniques*, 6(10):2803–2823, 2013a. doi: 10.5194/amt-6-2803-2013.

J. Joiner, L. Guanter, R. Lindstrot, M. Voigt, A. P. Vasilkov, E. M. Middleton, K. F. Huemmrich, Y. Yoshida, and C. Frankenberg. **Data download from http://avdc.gsfc.nasa.gov** for global monitoring of terrestrial chlorophyll fluorescence from moderate-spectral-resolution near-infrared satellite measurements: methodology, simulations, and application to gome-2. *Atmospheric Measurement Techniques*, 6(10):2803–2823, 2013b. doi: 10.5194/amt-6-2803-2013.

J Joiner, Y Yoshida, AP Vasilkov, K Schaefer, Martin Jung, L Guanter, Y Zhang, S Garrity, EM Middleton, KF Huemmrich, et al. The seasonal cycle of satellite

chlorophyll fluorescence observations and its relationship to vegetation phenology and ecosystem atmosphere carbon exchange. *Remote Sensing of Environment*, 152: 375–391, 2014.

J. Joiner, Y. Yoshida, L. Guanter, and E. M. Middleton. New methods for retrieval of chlorophyll red fluorescence from hyper-spectral satellite instruments: simulations and application to gome-2 and sciamachy. *Atmospheric Measurement Techniques Discussions*, 2016:1–41, 2016. doi: 10.5194/amt-2015-387.

Martin Jung, Markus Reichstein, Hank A Margolis, Alessandro Cescatti, Andrew D Richardson, M Altaf Arain, Almut Arneth, Christian Bernhofer, Damien Bonal, Jiquan Chen, et al. Global patterns of land-atmosphere fluxes of carbon dioxide, latent heat, and sensible heat derived from eddy covariance, satellite, and meteorological observations. *Journal of Geophysical Research: Biogeosciences*, 116(G3), 2011.

G.W. Kattawar, A.T. Young, and T.J. Humphreys. Inelastic scattering in planetary atmospheres, I, the Ring effect, without aerosols. *Astrophys. J.*, 243(3):1049–1057, 1981.

Jon E. Keeley and Philip W. Rundel. Evolution of cam and c4 carbon concentrating mechanisms. *International Journal of Plant Sciences*, 164(S3):S55–S77, 2003. ISSN 10585893, 15375315.

Narges Khosravi. Terrestrial Plant Fluorescence as seen from Satellite Data. Master's thesis, Institute of environmental physics, University of Bemen, 2012.

Narges Khosravi, Marco Vountas, Vladimir V Rozanov, Astrid Bracher, Alexandra Wolanin, and John P Burrows. Retrieval of terrestrial plant fluorescence based on the in-filling of far-red fraunhofer lines using sciamachy observations. *Frontiers in Environmental Science*, 3(78), 2015.

Jeffrey T Kiehl and Kevin E Trenberth. Earth's annual global mean energy budget. *Bulletin of the American Meteorological Society*, 78(2):197–208, 1997.

Stefan Kinne, Declan O'Donnel, Philip Stier, Silvia Kloster, Kai Zhang, Hauke Schmidt, Sebastian Rast, Marco Giorgetta, Tom F. Eck, and Bjorn Stevens. Mac-v1: A new global aerosol climatology for climate studies. *Journal of Advances in Modeling Earth Systems*, 5(4):704–740, 2013. ISSN 1942-2466. doi: 10.1002/jame.20035.

R. B. A. Koelemeijer, J. F. de Haan, and P. Stammes. A database of spectral surface reflectivity in the range 335-772 nm derived from 5.5 years of gome observations.

Journal of Geophysical Research: Atmospheres, 108(D2), 2003. ISSN 2156-2202. doi: 10.1029/2002JD002429.

Philipp Köhler, Luis Guanter, and Christian Frankenberg. Simplified physically based retrieval of sun-induced chlorophyll fluorescence from gosat data. *Geoscience and Remote Sensing Letters, IEEE*, 12(7):1446–1450, 2015a.

Philipp Köhler, Luis Guanter, and Joanna Joiner. A linear method for the retrieval of sun-induced chlorophyll fluorescence from gome-2 and sciamachy data. *Atmospheric Measurement Techniques*, 8(6):2589–2608, 2015b.

Zbigniew Kolber, Denis Klimov, Gennady Ananyev, Uwe Rascher, Joseph Berry, and Barry Osmond. Measuring photosynthetic parameters at a distance: laser induced fluorescence transient (lift) method for remote measurements of photosynthesis in terrestrial vegetation. *Photosynthesis Research*, 84(1):121–129, 2005. ISSN 1573-5079. doi: 10.1007/s11120-005-5092-1.

G. A. Korn and T. M. Korn. *Mathematical handbook for scientists and engineers*. McGraw-Hill Book Company, New York San Francisco Toronto London Sydney, 1968.

J. M. Krijger, M. van Weele, I. Aben, and R. Frey. Technical note: The effect of sensor resolution on the number of cloud-free observations from space. *Atmospheric Chemistry and Physics*, 7(11):2881–2891, 2007. doi: 10.5194/acp-7-2881-2007.

Andrew A Lacis, Gavin A Schmidt, David Rind, and Reto A Ruedy. Atmospheric co2: Principal control knob governing earth's temperature. *Science*, 330(6002):356–359, 2010.

J Lampel, U Frieß, and U Platt. The impact of vibrational raman scattering of air on doas measurements of atmospheric trace gases. *Atmospheric Measurement Techniques*, 8 (9):3767–3787, 2015.

Paul Latimer, T. T. Bannister, and E. Rabinowitch. Quantum yields of fluorescence of plant pigments. *Science*, 124(3222):585–586, 1956. ISSN 0036-8075. doi: 10.1126/science.124.3222.585.

Jeff W Lichtman and José-Angel Conchello. Fluorescence microscopy. *Nature methods*, 2(12):910–919, 2005.

Xinjie Liu, Liangyun Liu, Su Zhang, and Xianfeng Zhou. New spectral fitting method for full-spectrum solar-induced chlorophyll fluorescence retrieval based on principal components analysis. *Remote Sensing*, 7(8):10626–10645, 2015.

Juliette Louis, Abderrahmane Ounis, Jean-Marc Ducruet, Sébastien Evain, Tuomas Laurila, Tea Thum, Mika Aurela, Gunnar Wingsle, Luis Alonso, Roberto Pedros, et al. Remote sensing of sunlight-induced chlorophyll fluorescence and reflectance of scots pine in the boreal forest during spring recovery. *Remote sensing of environment*, 96(1):37–48, 2005.

Jason S Lupoi. Developments in enzyme immobilization and near-infrared raman spectroscopy with downstream renewable energy applications. 2012.

Christel M Marian. Spin–orbit coupling and intersystem crossing in molecules. *Wiley Interdisciplinary Reviews: Computational Molecular Science*, 2(2):187–203, 2012.

Alexander Marshak, Anthony Davis, Warren Wiscombe, and Georgii Titov. The verisimilitude of the independent pixel approximation used in cloud remote sensing. *Remote sensing of environment*, 52(1):71–78, 1995.

M Meroni and R Colombo. Leaf level detection of solar induced chlorophyll fluorescence by means of a subnanometer resolution spectroradiometer. *Remote sensing of environment*, 103(4):438–448, 2006.

M. Meroni, M. Rossini, L. Guanter, L. Alonso, U. Rascher, R. Colombo, and J. Moreno. Remote sensing of solar-induced chlorophyll fluorescence: Review of methods and applications. *Remote Sensing of Environment*, 113(10):2037 – 2051, 2009. ISSN 0034-4257. doi: 10.1016/j.rse.2009.05.003.

M Meroni, L Busetto, R Colombo, L Guanter, J Moreno, and W Verhoef. Performance of spectral fitting methods for vegetation fluorescence quantification. *Remote Sensing of Environment*, 114(2):363–374, 2010.

Elizabeth M Middleton, LA Corp, and PKE Campbell. Comparison of measurements and fluormod simulations for solar-induced chlorophyll fluorescence and reflectance of a corn crop under nitrogen treatments. *International Journal of Remote Sensing*, 29(17-18):5193–5213, 2008.

GF Midgley, L Hannah, D Millar, MC Rutherford, and LW Powrie. Assessing the vulnerability of species richness to anthropogenic climate change in a biodiversity hotspot. *Global Ecology and Biogeography*, 11(6):445–451, 2002.

S. Mieruch, S. Noël, H. Bovensmann, and J. P. Burrows. Analysis of global water vapour trends from satellite measurements in the visible spectral range. *Atmospheric Chemistry and Physics*, 8(3):491–504, February 2008.

John R Miller, Michael Berger, Luis Alonso, Zoran Cerovic, Yves Goulas, Stéphane Jacquemoud, Juliette Louis, Gina Mohammed, Ismael Moya, Roberto Pedros, et al. Progress on the development of an integrated canopy fluorescence model. In *Geoscience and Remote Sensing Symposium, 2003. IGARSS'03. Proceedings. 2003 IEEE International*, volume 1, pages 601–603. IEEE, 2003.

JR Miller, EW Hare, and Jiyou Wu. Quantitative characterization of the vegetation red edge reflectance 1. an inverted-gaussian reflectance model. *Remote Sensing*, 11(10): 1755–1773, 1990.

JR Miller, M Berger, Y Goulas, S Jacquemoud, J Louis, G Mohammed, N Moise, J Moreno, I Moya, R Pedrós, et al. Development of a vegetation fluorescence canopy model. *ESTEC Contract*, 16365(02), 2005.

I Moya, L Camenen, S Evain, Y Goulas, Z.G Cerovic, G Latouche, J Flexas, and A Ounis. A new instrument for passive remote sensing: 1. measurements of sunlight-induced chlorophyll fluorescence. *Remote Sensing of Environment*, 91(2):186 – 197, 2004. ISSN 0034-4257. doi: 10.1016/j.rse.2004.02.012.

Patricia Müller, Xiao-Ping Li, and Krishna K. Niyogi. Non-photochemical quenching. a response to excess light energy. *Plant Physiology*, 125:1558–1566, 2001. doi: 10.1104/pp.125.4.1558.

Zhuoya Ni, Zhigang Liu, Zhao-Liang Li, Françoise Nerry, Hongyuan Huo, Rui Sun, Peiqi Yang, and Weiwei Zhang. Investigation of atmospheric effects on retrieval of sun-induced fluorescence using hyperspectral imagery. *Sensors*, 16(4):480, 2016.

NOAA. U.s. agricultural belts, 2015.

Naomi Oreskes. The scientific consensus on climate change. *Science*, 306(5702): 1686–1686, 2004. ISSN 0036-8075. doi: 10.1126/science.1103618.

C. Papageorgiou and Govindjee. *Chlorophyll a Fluorescence: A Signature of Photosynthesis*. Springer, 2004.

Albert Porcar-Castell, Esa Tyystjärvi, Jon Atherton, Christiaan van der Tol, Jaume Flexas, Erhard E. Pfündel, Jose Moreno, Christian Frankenberg, and Joseph A. Berry. Linking chlorophyll a fluorescence to photosynthesis for remote sensing applications: mechanisms and challenges. *Journal of Experimental Botany*, 2014. doi: 10.1093/jxb/eru191.

U. Rascher, G. Agati, L. Alonso, G. Cecchi, S. Champagne, R. Colombo, A. Damm, F. Daumard, E. de Miguel, G. Fernandez, B. Franch, J. Franke, C. Gerbig, B. Gioli, J. A. Gómez, Y. Goulas, L. Guanter, Ó. Gutiérrez-de-la Cámara, K. Hamdi, P. Hostert, M. Jiménez, M. Kosvancova, D. Lognoli, M. Meroni, F. Miglietta, A. Moersch, J. Moreno, I. Moya, B. Neininger, A. Okujeni, A. Ounis, L. Palombi, V. Raimondi, A. Schickling, J. A. Sobrino, M. Stellmes, G. Toci, P. Toscano, T. Udelhoven, S. van der Linden, and A. Zaldei. Cefles2: the remote sensing component to quantify photosynthetic efficiency from the leaf to the region by measuring sun-induced fluorescence in the oxygen absorption bands. *Biogeosciences*, 6(7):1181–1198, 2009. doi: 10.5194/bg-6-1181-2009.

A Rosema, W Verhoef, J Schroote, and JFH Snel. Simulating fluorescence light-canopy interaction in support of laser-induced fluorescence measurements. *Remote Sensing of environment*, 37(2):117–130, 1991.

M Rossini, L Nedbal, L Guanter, A Ač, L Alonso, A Burkart, S Cogliati, R Colombo, A Damm, M Drusch, et al. Red and far red sun-induced chlorophyll fluorescence as a measure of plant photosynthesis. *Geophysical research letters*, 42(6):1632–1639, 2015.

Micol Rossini, Michele Meroni, Marco Celesti, Sergio Cogliati, Tommaso Julitta, Cinzia Panigada, Uwe Rascher, Christiaan van der Tol, and Roberto Colombo. Analysis of red and far-red sun-induced chlorophyll fluorescence and their ratio in different canopies based on observed and modeled data. *Remote Sensing*, 8(5):412, 2016.

V. V Rozanov. Personal correspondence, 2014.

V.V. Rozanov, A.V. Rozanov, A.A. Kokhanovsky, and J.P. Burrows. Radiative transfer through terrestrial atmosphere and ocean: Software package SCIATRAN. *Journal of Quantitative Spectroscopy and Radiative Transfer*, 133:13 – 71, 2014. ISSN 0022-4073. doi: 10.1016/j.jqsrt.2013.07.004.

N. Sabater, L. Alonso, S. Cogliati, J. Vicent, C. Tenjo, J. Verrelst, and J. Moreno. A sun-induced vegetation fluorescence retrieval method from top of atmosphere radiance for the flex/sentinel-3 tandem mission. In *2015 IEEE International Geoscience and Remote Sensing Symposium (IGARSS)*, pages 2669–2672, July 2015. doi: 10.1109/IGARSS.2015.7326362.

Rowan F Sage. The evolution of c. *New Phytologist*, 161:341–370, 2004.

A. F. J. Sanders and J. F. de Haan. Retrieval of aerosol parameters from the oxygen a band in the presence of chlorophyll fluorescence. *Atmospheric Measurement Techniques*, 6(10):2725–2740, 2013. doi: 10.5194/amt-6-2725-2013.

C. Schlundt, A. A. Kokhanovsky, W. von Hoyningen-Huene, T. Dinter, L. Istomina, and J. P. Burrows. Synergetic cloud fraction determination for SCIAMACHY using MERIS. *Atmospheric Measurement Techniques*, 4(2):319–337, 2011. doi: 10.5194/amt-4-319-2011.

Karan Deo Singh. Global forest resources assessments. In *Capacity building for the planning, assessment and systematic observations of forests*, pages 203–211. Springer, 2013.

Christopher E Sioris, Grégory Bazalgette Courrèges-Lacoste, and Marc-Philippe Stoll. Filling in of fraunhofer lines by plant fluorescence: Simulations for a nadir-viewing satellite-borne instrument. *Journal of Geophysical Research: Atmospheres*, 108(D4), 2003.

N Subhash and CN Mohanan. Curve-fit analysis of chlorophyll fluorescence spectra: Application to nutrient stress detection in sunflower. *Remote Sensing of environment*, 60(3):347–356, 1997.

Petr Sušila and Jan Nauš. A monte carlo study of the chlorophyll fluorescence emission and its effect on the leaf spectral reflectance and transmittance under various conditions. *Photochemical & Photobiological Sciences*, 6(8):894–902, 2007.

L. Taiz and E. Zeiger. *Plant physiology*, volume 79. Sinauer Associates Ltd., second edition, 1998.

Yu M Timofeyev and Aleksander Vladimirovich Vasil'ev. *Theoretical fundamentals of atmospheric optics*. Cambridge Int Science Publishing, 2008.

C Tol, JA Berry, PKE Campbell, and U Rascher. Models of fluorescence and photosynthesis for interpreting measurements of solar-induced chlorophyll fluorescence. *Journal of Geophysical Research: Biogeosciences*, 119(12):2312–2327, 2014.

C Van der Tol, W Verhoef, and A Rosema. A model for chlorophyll fluorescence and photosynthesis at leaf scale. *Agricultural and forest meteorology*, 149(1):96–105, 2009a.

C Van der Tol, W Verhoef, J Timmermans, A Verhoef, and Z Su. An integrated model of soil-canopy spectral radiance observations, photosynthesis, fluorescence, temperature and energy balance. *Biogeosciences Disc*, 6:6025–6075, 2009b.

Christiaan van der Tol, Micol Rossini, Sergio Cogliati, Wouter Verhoef, Roberto Colombo, Uwe Rascher, and Gina Mohammed. A model and measurement comparison of diurnal cycles of sun-induced chlorophyll fluorescence of crops. *Remote Sensing of Environment*, 186:663–677, 2016.

A. Vasilkov, J. Joiner, and R. Spurr. Note on rotational-raman scattering in the o_2 a- and b-bands. *Atmos. Meas. Tech.*, 6:981–990, 2013. doi: 10.5194/amt-6-981-2013.

W. Verhoef. Light scattering by leaf layers with application to canopy reflectance modeling: The sail model. *Remote Sensing of Environment*, 16(2):125 – 141, 1984. ISSN 0034-4257. doi: 10.1016/0034-4257(84)90057-9.

Jochem Verrelst, Juan Pablo Rivera, Christiaan van der Tol, Federico Magnani, Gina Mohammed, and Jose Moreno. Global sensitivity analysis of the scope model: What drives simulated canopy-leaving sun-induced fluorescence? *Remote Sensing of Environment*, 166:8–21, 2015.

M. Vountas, V. V. Rozanov, and J. P. Burrows. Ring effect: Impact of rotational Raman scattering on radiative transfer in Earth's atmosphere. *J. Quant. Spectrosc. Radiat. Transfer*, 60:943–961, 1998.

Sophia Walther, Maximilian Voigt, Tea Thum, Alemu Gonsamo, Yongguang Zhang, Philipp Koehler, Martin Jung, Andrej Varlagin, and Luis Guanter. Satellite chlorophyll fluorescence measurements reveal large-scale decoupling of photosynthesis and greenness dynamics in boreal evergreen forests. *Global change biology*, 2015.

Weatherspark. URL https://weatherspark.com/.

A. Wolanin, V.V. Rozanov, T. Dinter, S. Noël, M. Vountas, J.P. Burrows, and A. Bracher. Global retrieval of marine and terrestrial chlorophyll fluorescence at its red peak using hyperspectral top of atmosphere radiance measurements: Feasibility study and first results. *Remote Sensing of Environment*, 166:243 – 261, 2015. ISSN 0034-4257. doi: 10.1016/j.rse.2015.05.018.

Pablo J Zarco-Tejada, John R Miller, Gina H Mohammed, and Thomas L Noland. Chlorophyll fluorescence effects on vegetation apparent reflectance: I. leaf-level measurements and model simulation. *Remote Sensing of Environment*, 74(3):582–595, 2000.

Pablo J Zarco-Tejada, JC Pushnik, S Dobrowski, and SL Ustin. Steady-state chlorophyll a fluorescence detection from canopy derivative reflectance and double-peak red-edge effects. *Remote Sensing of Environment*, 84(2):283–294, 2003.

P.J. Zarco-Tejada, J.R. Miller, R. Pedrós, W. Verhoef, and M. Berger. Fluormodgui v3.0: A graphic user interface for the spectral simulation of leaf and canopy chlorophyll fluorescence. *Computers & Geosciences*, 32(5):577 – 591, 2006. ISSN 0098-3004. doi: 10.1016/j.cageo.2005.08.010.

Yao Zhang, Xiangming Xiao, Cui Jin, Jinwei Dong, Sha Zhou, Pradeep Wagle, Joanna Joiner, Luis Guanter, Yongguang Zhang, Geli Zhang, et al. Consistency between sun-induced chlorophyll fluorescence and gross primary production of vegetation in north america. *Remote Sensing of Environment*, 183:154–169, 2016a.

Yongguang Zhang, Luis Guanter, Joseph A Berry, Joanna Joiner, Christiaan Tol, Alfredo Huete, Anatoly Gitelson, Maximilian Voigt, and Philipp Köhler. Estimation of vegetation photosynthetic capacity from space-based measurements of chlorophyll fluorescence for terrestrial biosphere models. *Global change biology*, 20(12):3727–3742, 2014.

Yongguang Zhang, Luis Guanter, Joseph A Berry, Christiaan van der Tol, Xi Yang, Jianwu Tang, and Fangmin Zhang. Model-based analysis of the relationship between sun-induced chlorophyll fluorescence and gross primary production for remote sensing applications. *Remote Sensing of Environment*, 187:145–155, 2016b.